Fabrication and measurement of superconducting nanowires

by

Dominic Christoph Walliman

A thesis submitted to the
College of Engineering and Physical Sciences,
UNIVERSITY OF BIRMINGHAM
for the degree of
DOCTOR OF PHILOSOPHY

School of Physics and Astronomy
The University of Birmingham
April 2010

Abstract

An investigation was made into techniques that could be employed to produce sub-100nm wide superconducting nanowires. Nanowires of niobium and $YBa_2Cu_3O_{7-\delta}$ (YBCO) were fabricated in thin films using focused gallium ion beam milling (FIB) to a range of widths (100nm-300nm). A procedure was developed to controllably reduce the wire widths using argon ion beam milling. Milling niobium wires under rotation at 75° to the normal produced wires with width and thickness ∼70nm. The nanowires were cryogenically cooled to 4K and the resistance versus temperature characteristics measured. Nb and YBCO wires exhibited a broadening of the superconducting transition, which fitted reasonably with the theory of thermally activated phase slips. Further analysis of the voltage versus current characteristics of the wires showed behaviour not in agreement with the established theory. Various possible explanations were considered for this, with the conclusion that damage to the wires caused by implantation of gallium was the most likely cause.

Acknowledgements

There are loads of people who have helped me over the last four years. I'd like to thank you all very much.

First I'd like to thank all the fellow students and studious fellows, past and present, for making the group such an enjoyable environment to work in. The fluctuation of conversation from the sublime to the inane has always been quite stimulating. From those who have left, Charlotte, Christian, Rich, Silvia, Phil and Jonny, to those who are still here Jo, Georgina, Suz, Alex, Elizabeth, Josh, Rich and Al; thanks for all the cake.

A special mention to Suz, with whom I enjoyed many conversations about the fringes of science and tech (the future is going to be awesome). And to Jonny who was always fun for a chat (and a grumble). Alex and Elizabeth, it has been a pleasure working with you, I wish both all the very best in Birmingham. Georgina, it's been fun, I hope your experiments are kind to you. And Rich, don't loose hope, you'll get there.

Thanks also to my supervisor Chris Muirhead, who never made me feel scared to ask stupid questions (and many there were), and who's capacious knowledge of physics always came in handy. And to Mark, who's knowledge of electronics was truly colossal. A mention to Ted who's physics puzzles I always enjoyed (was I the only one?), and were certainly of better quality than the jokes. Also to Ed Tarte who always had some good advice for me when everything seemed to be going a bit wrong.

I'd also like to thank the people who have helped me in my project. James for all the AFM work, Spartaco for his immense work on the EBL, and Jason, who was always there to help when the FIB broke (again). Also to Gary and Michael for all their hard work and constant supply of helium.

I have to thank my family for always being interested in what I was doing and generally being a brilliant source of reassurance and nice food. I really am lucky to be related to such lovely people.

And thanks to all of my great friends, most of all to Lucy, without who's constant encouragement and hugs I don't think that this would ever have been possible.

Thank you.

Contents

List of Figures

List of Tables

Commonly used Symbols and Abbreviations

T_c - Transition temperature of a superconductor.

J_c - Critical current density of a superconductor.

H_c - Thermodynamic critical field.

H_{c1} - Lower critical field of type II superconductor.

H_{c2} - Upper critical field of type II superconductor.

ϕ_0 - The flux quantum.

Δ - Energy gap of a superconductor.

ψ - The superconducting order parameter.

S - The phase of the superconducting order parameter.

γ - Phase difference.

n_s - Density of superconducting electrons.

e - charge of electron.

λ_L - penetration depth.

ξ_{GL} - Ginzberg-Landau coherence length.

$\xi(0)$ - BCS coherence length.

ν_F - The Fermi velocity.

l - mean free path.

I_0 - Critical current.

U_J - Tilted washboard potential.

Ω - Attempt frequency.

τ_{GL} - Ginzberg-Landau coherence length.

ΔF_0 - Height of energy barrier in phase slip dynamics.

R_q - Quantum of resistance.

R_n - Normal resistance of superconductor, T just above T_c.

YBCO - The high temperature superconductor $YBa_2Cu_3O_{7-\delta}$.

BSCCO - The high temperature superconductor $Bi_2Sr_2CaCu_2O_{8+\delta}$.

HTS - High temperature superconductor.

TAPS - Thermally activated phase slip.

QPS - Quantum phase slip.

LAMH - Langer, Ambegaokar, McCumber and Halperin theory of thermally activated phase slips.[1][2]

FIB - Focused ion beam milling.

SEM - Scanning electron microscope.

AFM - Atomic force microscope.

EBL - Electron beam lithography.

Chapter 1

Introduction

In this thesis I present an investigation into the fabrication and electronic measurement of superconducting nanowires of niobium and $YBa_2Cu_3O_{7-\delta}$ (YBCO). The fabrication of nanowires is technically very difficult, requiring advanced nano fabrication techniques. Throughout this project many different techniques were investigated which led to the successful fabrication of 70nm wide niobium nanowires.

The electronic properties of nanowires is of fundamental interest in both superconductors and normal metals. In superconductors the superconducting state can be suppressed in very narrow samples. One of the causes of this suppression, a behaviour called phase slips, is interesting as it has possible applications to establish a novel current standard [3], or a new design of solid state qubit [4]. The breakdown of superconductivity at low dimensions is also interesting as it sets a limit to the miniaturisation of superconducting electronics.

Producing nanowires of normal metals is also of interest for a similar

reason. As the scale of cutting edge micro electronics and computing elements are constantly being decreased it is useful to investigate what the lower limits of this miniaturisation are. Fabricating computing elements in the nano scale presents new problems as to the reliability of the components. There has also been a significant body of work looking at the behaviour of electrons in one-dimensional metals [5](and references therein), where localization of the conduction electrons was shown to break down conductivity at small scales.

For these reasons, developing techniques that allow for the controllable production of nanowires is a worthwhile endeavour. There has been a large body of work published on many different techniques used to fabricate superconducting nanowires, and review of this work is presented in chapter 2 along with an analysis of the main results. At the end of this chapter I present initial work I performed to attempt to produce nanowires.

During the course of the project a broad range of techniques were employed to fabricate the nanowires. These process required a good deal of characterisation to successfully produce wires with diameters less than 100nm. The techniques used and characterisation results are presented in chapter 3. The most successful technique was to employ a combination of photolithography and focused ion beam milling to produce ∼200nm wide wires. Further reduction of wire size was enabled by milling using an argon ion beam. To successfully reduce the wire width and height evenly, the milling process was characterised to find the optimum angle of the wire to the beam. The process of characterisation that was developed enabled the reduction of niobium nanowires to 70nm. This process is material independent and is applicable to produce nanowires of any other material.

The superconducting properties of superconducting nanowires is significantly different to that of bulk superconductors. Chapter 4 is devoted to covering the laws of basic superconductivity and focusing on the phenomenon of phase slips that are exhibited by very narrow superconducting wires. To help explain the phenomenon of phase slips a treatment of the Josephson effects is made.

Phase slips only occur in one-dimensional superconducting wires. To be considered one-dimensional the wires have to be narrow enough to suppress superconductivity in every dimension apart from along the length of the wire. This criterion is reached when the wire has a diameter less than the coherence length (ξ), which varies for different superconductors but is generally in the range $\sim$100nm. In a narrow range of temperatures below T_c, the dominant mechanism of phase slippage is by thermal activation *over* an energy barrier. At lower temperatures the dominant mechanism is expected to be by quantum tunnelling of the phase *through* the energy barrier.

To determine whether the nanowires produced exhibited phase slip behaviour the resistance was measured at low temperatures. For this, cryogenic cooling systems and electrical measuring apparatus was employed. This measuring and cooling equipment is described in chapter 5.

Finally, chapter 6 presents the results from the electrical measurements. The results are analysed in terms of the theory of phase slips to determine if the characteristics observed can be explained by them. An analysis is made of the V(I) and R(T) characteristics of the wires.

Chapter 2

Fabrication Techniques

To investigate the quantum phase slip process one needs to fabricate wires with a diameter of a few tens of nm. This has been a challenge for many years. Research has been done into many different techniques to make wires that have such small dimensions. In this chapter I shall describe the different techniques that have been used so far in this field.

2.1 Typical Issues with Fabrication

There are several issues regarding the fabrication of good superconducting nanowires. This section covers the problems that can occur in the fabrication process, and what impact they can have on the quality of the samples produced.

2.1.1 Uneven Cross-section

When fabricating a narrow wire it is important that the cross-section is uniform along the length of the wire. This is because, at dimensions comparable to the coherence length, the T_c of most superconductors is dependent on the physical size of the sample. Deviation away from the bulk T_c values is seen in both thin films and narrow wires [6]. An increase of T_c is exhibited by indium, aluminium and zinc, while a decrease is seen in MoGe, niobium and lead ([6] and references therein). Interestingly tin shows no change of T_c with sample size. If a nano-wire has a large variation of cross section along its length, different sections turn superconducting at different temperatures. This behaviour can look very much like the R-T characteristics predicted by LAMH theory, so the experimentalist needs to be careful when interpreting data from wires with an uneven diameter.

In a paper by Zgirski and Arutyunov [6] it was shown that the broadening of a transition due to T_c variation along the length of a wire can mask that caused by thermally activated phase slips. They calculated the R(T) characteristics of an Aluminium wire whose cross section varied from 5000 to 6500 nm^2, and found the resistance to be greater then that predicted for TAPS (Fig. 2.1).

2.1.2 Granularity

In very narrow wires the granularity of the material can be a problem for two reasons: the grains each having a different T_c, and the grain boundaries behaving like weak links. The techniques commonly used to produce nano-

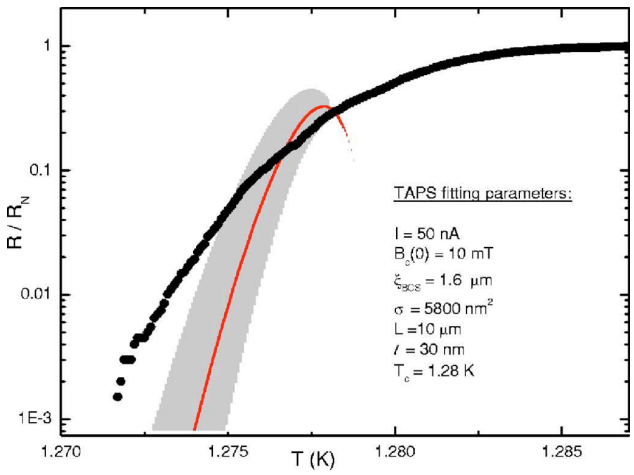

Figure 2.1: Results from [6] showing the predicted resistance of an aluminium wire due to varying T_c (solid black dots), compared to the resistance from TAPS (solid red line). The grey region is the TAPS resistance with a $\pm 10\%$ variation of the mean free path and critical field. The diameter of the wire has a variation of 20% along the length, which shows that even a relitively small amount of roughness can cause the TAPS resistance to be masked.

wires involve the deposition of the superconducting material via evaporation, sputtering or laser deposition, and all produce granular films.

If the grains have different T_c values then, just like the case of uneven cross section along the length, the transition can become broad as each of the grains become superconducting at different temperatures. There are two obvious mechanisms for this effect. Firstly, if the grains are similar in size to the coherence length of the superconductor then they will have a T_c variation dependant on their physical size, similar to the T_c variation caused by uneven an cross section of a wire. Secondly, different crystallographic growth directions can have different free energies, causing different orientations of grains to have different T_c's.

If the boundaries between grains are insulating they behave like Josephson

junctions. In this regime a sample can no longer be treated as a nanowire, as it is essentially a long series of coupled superconductors having a very different behaviour to that of a continuous wire. This is mainly a problem with high temperature superconductors when the grains have different growth directions, causing the interface to behave like weak link [7]

Therefore, care needs to be taken to use materials, or deposition techniques, that produce as little granularity as possible.

2.1.3 Contact

It is preferable to use the 4-terminal contact method to make electrical measurements of a nanowire. In the 4-terminal method current is passed via two of the leads and voltage measured across the other two. The advantage of this design is that only the resistance of the wire will be measured and not the resistance of the leads. Unfortunately it is not always possible to employ the 4-terminal method, indeed many experiments have had to resort to a two-terminal measurement [8] [9] [10]. Analysis of the results of these experiments is complicated by the fact that the measured resistance includes that of the leads. These leads are normally made of the same superconductor as the sample, although they may not have the same T_c. This is only a problem in the materials that have an increase in T_c with reduced dimension as the nanowire will turn superconducting before the leads. Therefore, the results from these experiments are only valid below the bulk T_c.

This same problem can occur even in the 4-terminal contact method (Fig. 2.2). In this case the contribution from the leads can cause a resistance at low

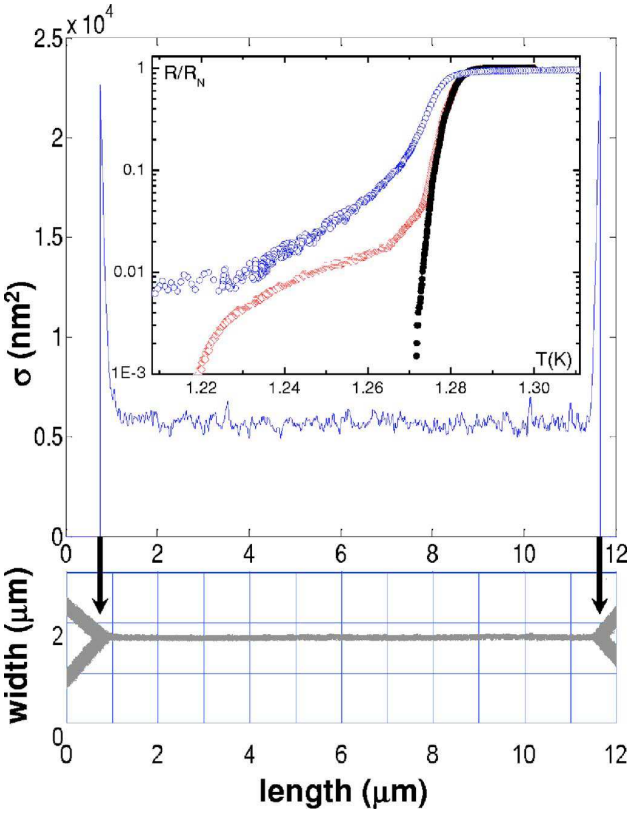

Figure 2.2: Results from [6], showing the contribution of leads to the measured resistance of a nanowire. The solid black dots show the contribution of the varying T_c along the wire. The red diamonds show the contribution due to the lower T_c of the leads. These are both theoretical. The blue circles are the measured resistance of the wire.

temperatures reminiscent to that of QPS. Therefore it is easier to interpret results from materials that have an increasing T_c with reduced dimensions. Both niobium and YBCO show this behaviour.

2.1.4 Measurement

Although this section is mainly concerned with the issues with fabricating very narrow superconducting wires, it is important to explain what is needed

to measure them properly. The details of the electrical measurement are covered in more detail in chapter 5. When measuring nanowires it is important that there is good electromagnetic shielding of the sample, and good filtering of the electronics used to measure the sample. This is because any interference of external noise, either from external electromagnetic radiation, or from noisy electronics, can cause fluctuations in the wire. These fluctuations will be temperature independent, and so observable at low temperatures where they could easily be misinterpreted as QPS. It is worth noting that, until recently [11], none of the papers reported what kind of shielding and filtering they used, making it difficult to assess the reliability of their results with regard to the measurement of QPS.

2.2 Techniques Used in Literature

To successfully produce a narrow superconducting wire that will exhibit phase slips several conditions need to be met. In the last 40 years, experimentalists have tried many different techniques to produce good samples. These different techniques have inherent advantages and disadvantages, and these are described in this section.

2.2.1 Whisker Growth

The first experiments into the superconductivity of narrow wires were performed in the early 70's by Lukens [12] and Newbower [13]. They produced very pure tin whiskers of diameter $\sim 1\mu$m and lengths up to 1mm. These whiskers were grown using standard techniques [14]. The whiskers were single

crystal and so were very uniform and did not contain any defects or impurities. Four point electrical contacts were made to the whiskers by soldering with Wood's metal, although this had a tendency to damage the crystal structure resulting in a rather low yield of usable samples. The samples that remained undamaged gave good results with very good fitting to the LAMH theory (Fig. 2.3).

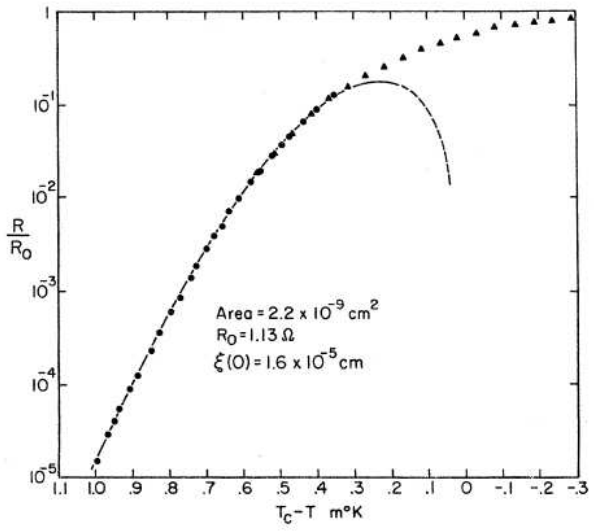

Figure 2.3: The resistance vs. temperature plot for a tin whisker [12]. The dashed line gives the theoretical LAMH fit to the data. The T_c of tin is 3.73K.

Unfortunately there are several limitations to using whiskers to investigate phase slips. The whiskers are difficult to manage because they have to be manipulated by hand and placed on the substrate to have contacts made. Also there is no control over the magnitude of the diameter of the whisker that grows. They grow naturally with diameter $\sim 1\mu$m, and at this size the broadening of the transition due to TAPS is small. Therefore very good temperature control is needed to obtain reliable results as the resistance drops

by 5 orders of magnitude in 0.7K. This also means that the whiskers have to be subsequently narrowed if one wants to investigate phase slips in smaller diameter wires.

Another way of producing single crystal wires was developed [15], which involved the growth of wires in a membrane. This allowed the production of single crystal whiskers as small as 20nm in diameter. Unfortunately, it was difficult to measure single wires because they quickly deformed when removed from the membrane, so measurements were done on whole arrays of them in parallel. The results showed good fitting to TAPS and QPS (Fig. 2.4), although it is difficult to draw conclusions about the slip process from these results because of the large range of samples being measured.

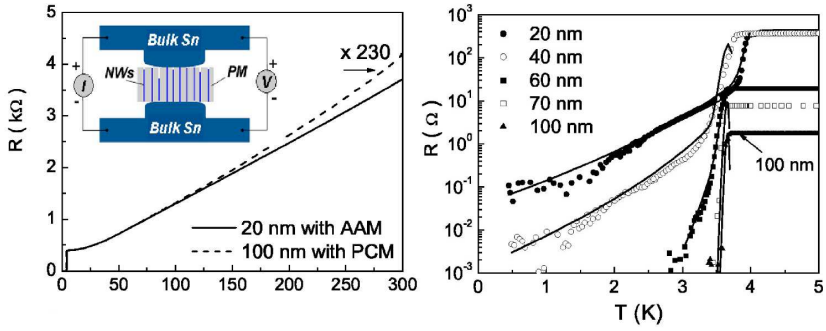

Figure 2.4: Diagram showing the R(T) characteristics of an array of tin nanowires [15]

2.2.2 Step Decoration

In the late 1980's early 90's a series of papers were published by Giordano and co-workers [16] [17] [18] [19] reporting on the investigation of Pb and Pb-In narrow wires fabricated using the step edge template decoration method

[20] (Fig. 2.5).

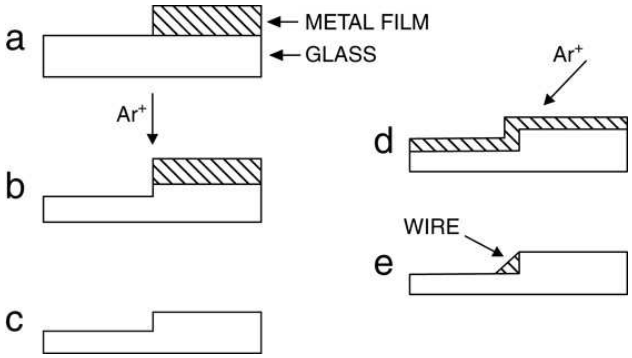

Figure 2.5: Diagram of the step decoration technique [20]. (Diagram from [21])

They managed to fabricate wires of diameters $\sim$ 20-100nm, and obtain a reasonable fit to LAHM theory. Some of the narrower tracks showed a deviation from LAMH theory at lower temperatures, which were attributed to QPS. However this has since been contested as the deviation may have been caused by the granularity of the deposited films [9].

2.2.3 Stencil

In the 90's Dynes and co-workers performed a series of experiments on a number of materials, looking at the transition from strong to weak localisation in 1D wires. They investigated the materials Sn, Pb, PbBi, Ag and Au, and fabricated granular wires with widths as small as 40nm [22]. They did this by evaporating metal through a suspended stencil (Fig. 2.6).

The advantage of their method was that the deposition and measurement apparatus were all in the same vacuum chamber, meaning that several depositions and measurements could be made without breaking vacuum. This was

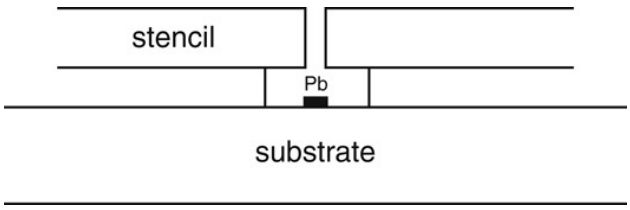

Figure 2.6: Diagram of the evaporation metal through a suspended stencil to produce a narrow wire [23].

a good design because the evolution of the resistance of a sample could be seen as the wire became thicker. At low temperatures they observed a larger resistance then that predicted by LAMH theory for the superconducting materials. They recognised that this could have been due to granularity of the wires, so a further test on amorphous Pb wires was performed [24]. Again the deviation away from LAHM theory was observed, although it was less dramatic. This behaviour could be interpreted as evidence for QPS, although in this case, there was no indication of resistance at very low temperatures (Fig. 2.7).

2.2.4 Evaporation on Carbon Nanotubes

Some of the smallest nanowires that have been fabricated to date were made by evaporating metal on top of carbon nanotubes, suspended between two electrodes. Several materials were studied using this method including MoGe and Nb [9][10]. The authors took care to ensure that the wires were not granular, by imaging with transmission electron microscopy, and comparing the normal state resistivity of the wires to that calculated from their geometry and bulk resistivity values. Typical lengths of wire were 100 - 300 nm and

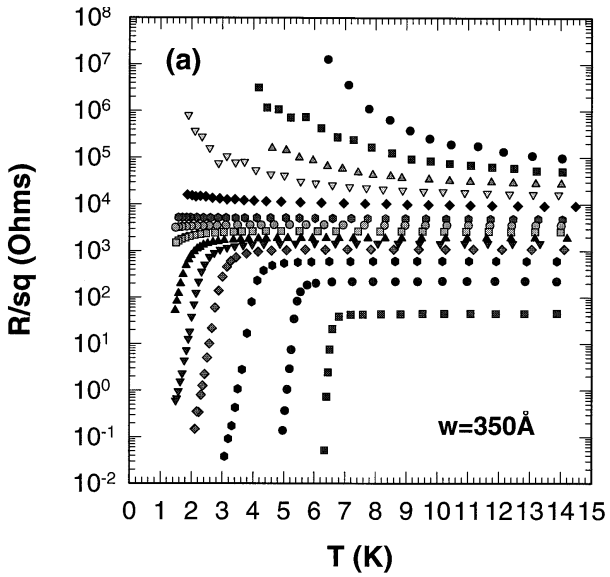

Figure 2.7: Resistance per square vs. temperature characteristics of a 35nm wide Pb film of different thickness' [24].

cross sections 10 - 30 nm. The Nb samples showed no deviation away from LAMH theory down to low temperatures. While the MoGe wires showed a significantly higher resistance at low temperatures than predicted by LAMH theory. This was attributed to QPS and fits were made to data (Fig. 2.8) using the QPS theory as described in section 2.3.3, although in order fit the data the authors used some additional pre-factors to the formulae as described in section 2.3.3. It was claimed that the results were good proof of QPS because the theory was able to fit all of the data with only one combination of pre-factors. However, there was no attempt to explain the physical significance of these pre-factors.

The large resistance at low temperatures may have had another source. As explained in section 3.1.3, an uneven cross section along the length of a nanowire can lead to an apparent resistance at low temperatures due to

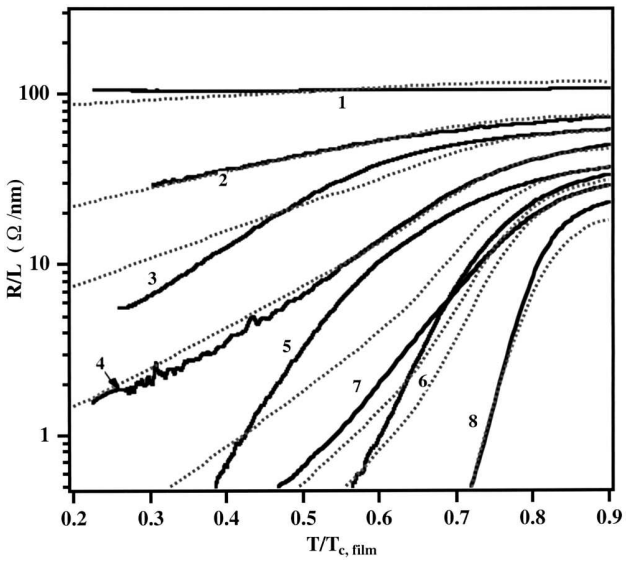

Figure 2.8: Resistance per unit length vs normalised temperatures for a series of evaporated MoGe nanowires. The diameter of samples ranged from 10 to 22 nm [9]

varying T_c. Unfortunately an analysis of the homogeneity of the cross section was not provided in this case. Another source of error can be a lack of correct filtering of electronics, and a lack of adequate shielding of the sample from outside sources of radiation. There was no mention steps taken to eliminate either of these problems in the paper.

2.2.5 E-beam and Ion beam milling

The most convincing evidence so far of QPS was from experiments on narrow wires of Al [11]. The wires were fabricated using E-beam lithography, and then subsequently narrowed using argon ion beam milling. The advantage of this method is that the same wire can be measured at several different thickness'. Also, the ion beam milling has an inherent polishing effect on the

wires, making their cross section very even along the length. The lengths of the wire measured were 10μm, with widths ranging from 50nm to 11nm. The very narrowest wires showed a large resistance at low temperatures, which were fitted with the QPS theory (Fig. 2.9). There was good shielding and filtering of electronics, and effects from granularity were small.

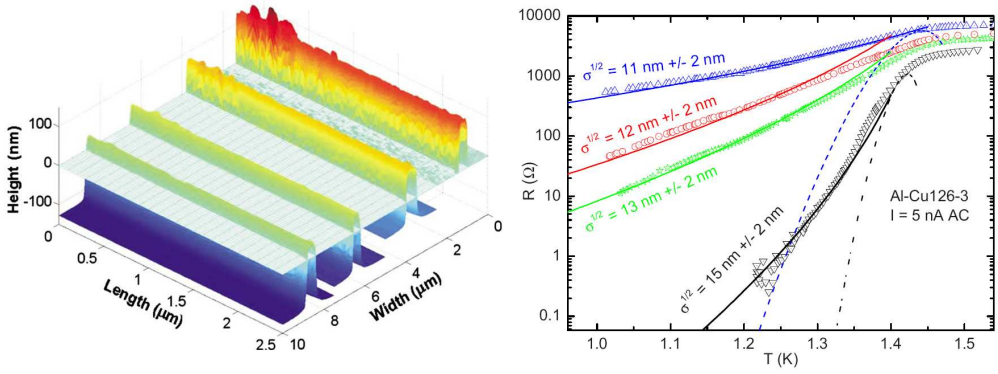

Figure 2.9: The progressive narrowing of an Al wire, and the results obtained from a set of these wires [11]. The dashed lines are plots predicted by LAMH theory while the solid lines are the plots predicted by QPS theory.

Most of this project has been involved with applying this method of fabrication to other superconducting materials.

2.2.6 High Tc

There has been very little work investigating phase slips in high temperature superconductors. This is due to the fact that the coherence length of HTS is very small, typically only a few nm. For YBCO this is only a few unit cells, so fabricating a wire this small is beyond the scope of technology today. Regardless of this, there has been an indication of phase slip behaviour occurring in HTS samples with a much larger cross section than the coherence length [25].

This experiment showed the results from the fabrication of several narrow wires of YBCO using focused gallium ion beam milling (FIB). The article showed a cross-over from superconducting to insulating behaviour when the normal state resistance increased above that of the quantum of resistance, reminiscent of earlier work on MoGe [9] (Fig. 2.10).

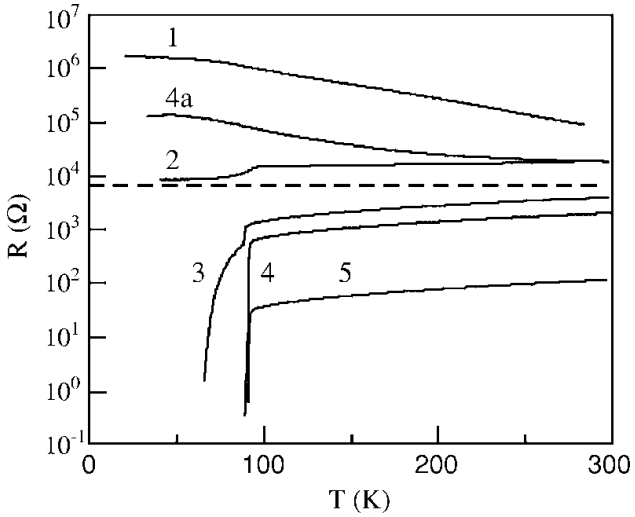

Figure 2.10: Graph showing the R(T) characteristics of a series of narrow wires of YBCO. Plot 3 shows a broadening reminiscent of TAPS. The wire width was 500nm, much larger than the coherence length of the superconductor.

One wire showed a broadened transition that could only be fitted to LAMH theory if the wire size was taken to be much smaller than the physical size observed. Two explanations of this were proposed. Firstly that the implantation of gallium ions into the superconductor during fabrication made the effective diameter of the wire much smaller, and alternatively that the current in a HTS may have a filamentary microstructure. The resistance could also have been caused by granularity, a significant problem in high

temperature superconductors because the grain boundaries are a similar size to the coherence length.

2.3 Early Work

This section covers the initial investigations of my PhD. The following experiments were informative in terms of finding new ways to fabricate nanowires, however they did not result in any samples that showed phase slip behaviour. I started my research by looking at the growth of single crystal whiskers of a high temperature superconductor BSCCO, and also investigated the feasibility of narrowing nanowires of YBCO using an acid etch.

2.3.1 BSCCO

$Bi_2Sr_2CaCu_2O_{8+\delta}$ (BSCCO) is a high temperature superconductor discovered in 1988 by Maeda et al [26]. It has a T_c of $\sim$105K. An interesting property of BSCCO is that it can be grown into very small, very pure, single-crystal whiskers. These are interesting with regards to this project because they do not have any grain boundaries, and the cross section is very uniform along the length. This makes them an ideal HTS to test for phase slips and to compare with the results from YBCO [25]. The whiskers grow to lengths up to 12mm, and have a diameter of $\sim 10\mu$m or more.

The whiskers were grown following a procedure [27] that involves grinding powders of the constituent chemicals and baking the mixture. This was done several times to ensure a good mixture of the chemicals. This mixture was then pressed into a pellet using a high pressure press. To grow the whiskers,

the pellet was placed in a furnace and baked at 885 °C to melt the surface, then baked further at 875 °C in flowing oxygen for 100 hours. The melting stage created a series of nucleation sites on the surface of the pellet out of which the whiskers grew during the 100 hour bake.

Early attempts at whisker growth by members of my group resulted in very short whiskers, too short to attach electrical contacts too. Through correspondence with M.Nagao, the author of [27], we were able to refine the procedure, and grew whiskers several mm long (Fig. 2.11).

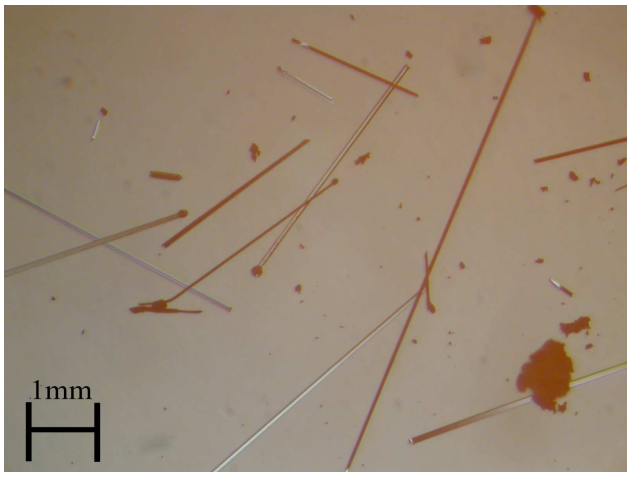

Figure 2.11: Picture of several BSCCO whiskers, with lengths up to 10mm.

Attaching electrical contacts to these whiskers was a challenge because the whiskers were so small. They had to be handled under a microscope with a single hair taken from a paintbrush. They were placed on an MgO substrate, and once there, had a small resistance to being moved. Contacts were attached by painting silver epoxy onto a whisker in 4 places along the length. The R(T) characteristics of several of these samples were measured in a continuous flow cryostat, however, none of the samples were superconducting

(Fig. 2.12).

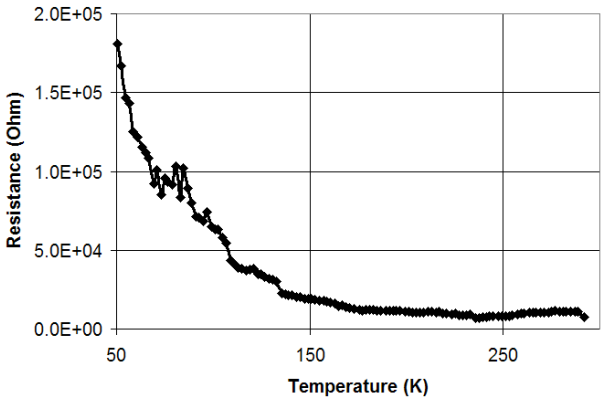

Figure 2.12: R(T) characteristic of a typical BSCCO whisker. The whisker shows an exponential increase of resistance with decrease of temperature suggesting it is semi-conducting. The general shape of this plot was reproducible, however the irregularities were not.

The production of non-superconducting whiskers could have been due to many factors. There are several phases of BSCCO in which whiskers can grow, each with different relative amounts of the constituent elements. This can be written $Bi_2Sr_2Ca_{n-1}Cu_nO_{2n+4+\sigma}$, where n can be 1, 2 or 3. Only the n=2 and n=3 states are superconducting, with n=1 being semi-conducting. This is likely to be the phase of the whiskers that were measured. Because of this, I attempted to address all of the factors that may have caused the growth of the wrong phase of BSCCO.

It has been shown that different annealing temperatures and different chemical compositions of the pellet produce whiskers of different morphologies [27]. Therefore several steps were taken to ensure that these variables were optimum for the whisker growth. Very high purity (99.9%-99.999% pure) chemicals were used. These were Bi_2O_3, $SrCO_3$, $CaCO_3$, CuO, and

TeO_2, used in the proportions 1:2:2:3:0.5. Tellurium is a catalyst that enhances the whisker growth, but does not appear in the final whiskers. The chemicals were weighed on a very accurate crystal balance weighing scale, and then ground in a new pestle and mortar.

The mixture was compressed into a pellet using a 10 tonne press. The die was made of stainless steel and was thoroughly cleaned with acetone before use. This produced a 1mm diameter pellet which was placed in a tube furnace for heat treatment. To minimise contamination, a new glass tube was bought for the furnace, and the pellet was placed in a new alumina boat. This followed the instructions received from our correspondence with the group that had produced the whiskers, which elaborated on that in [27].

The temperature when baking the pellet was critical for the growth of the right phase of whiskers. The temperature gauge of the tube furnace that was used was not very accurate, and there was also an inherent temperature gradient along the length of the tube. To ensure that the pellet was at the correct temperature during the bake, a thermocouple was placed beside it and the temperature was recorded. Because the internal thermometer of the tube furnace was not very accurate, the target temperature had be set to 30 °C higher than the temperature required. With these calibrations having been done, the temperature could be controlled to an accuracy of 1 °C.

The growth of good superconducting whiskers also requires a steady flow of oxygen. This ensures that the BSCCO has fully oxygenated CuO chains. At 875 °C the oxygen is able to quickly diffuse in and out of the structure, and only gets frozen in when the crystal is cooled to below 100 °C. Therefore, it is important to maintain a steady flow of oxygen while the crystals cool.

This was achieved by the release of 99.999% pure oxygen from a canister through medical grade nylon tubing.

To test the crystal structure of the resulting whiskers an X-ray diffraction pattern was taken of a batch of them. Single whiskers were too small to resolve using the x-ray that was used. The results of this diffraction showed peaks for both the n=1 and n=2 phases, suggesting that both superconducting and semi-conducting phases were present.

Despite all of these measures to ensure the correct phase of whiskers were grown, all electrical measurements on the whiskers still exhibited semiconducting behaviour. As a result of this we tried to obtain some superconducting whiskers from the group that had produced them. Unfortunately they could not provide us with any because the researcher that had grown the whiskers had subsequently left their group. At this point we decided to concentrate on other areas of research that were more productive.

2.3.2 Acid Etching

Previous work investigating phase slips in YBCO compared the results taken from many different samples [25]. A complication of this method is that sample specific effects can confuse the results, as each YBCO film will have slightly different superconducting characteristics. Therefore it is desirable to be able to measure and narrow the same samples in many stages to obtain a full evolution of R(T) characteristics with reducing cross section. To this end I investigated a method of reducing the width of YBCO narrow wires using acid etching.

This method was thought to be a good choice because the etch only effects the outer layer of the superconductor, leaving the rest undamaged. Previous work on YBCO [25] had used a focused gallium beam to fabricate the samples, which caused gallium implantation in the crystal structure. This destroys the superconductivity around the area milled, and so it is difficult to know the volume of a narrow wire that is still superconducting. Using an acid etch overcomes this problem as only the surface of the material is affected.

YBCO is etched by nitric acid, with the etch rate being dependant on the concentration of the acid. It was thought that a very dilute solution would etch a wire of YBCO in a slow and controllable way. Also, the resistance of the the wire could be measured while it is being etched, giving an indication of size of the wire. By leaving photo-resist on top of a wire after photolithography the width could be reduced while the thickness remained the same (Fig. 2.13).

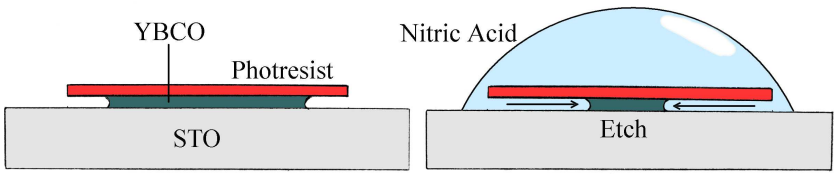

Figure 2.13: Diagram showing the acid etching process.

This etching successfully enabled the reduction of wire size, but unfortunately inherent problems prevented the production of very small wires. One problem was the photoresist being vulnerable to cracking after several thermal cycles. On subsequent etchings, these cracks allowed acid to etch vertically through the wire, and as the thickness of the wires were small in

comparison to the width, they were quickly etched through. To overcome this problem a mask that was unaffected by thermal cycling could have been used, however other problems became apparent before this was developed.

The acid etch was never uniform over the length of the wire, and so the cross section became increasingly uneven after several etchings. Because the T_c of YBCO goes down with the size of the sample it is important to maintain an even cross-sectional area along the length (Section 3.1.1). Critically this uneven etching was independent of the concentration of the acid, and so must be inherent to the etching process. A simple model can explain this effect. The etch rate is dependant on the surface area being etched. This means that any defects along the length of the wire will be preferentially etched with respect to smooth surfaces. Over time this leads to an increase of roughness (Fig. 2.14).

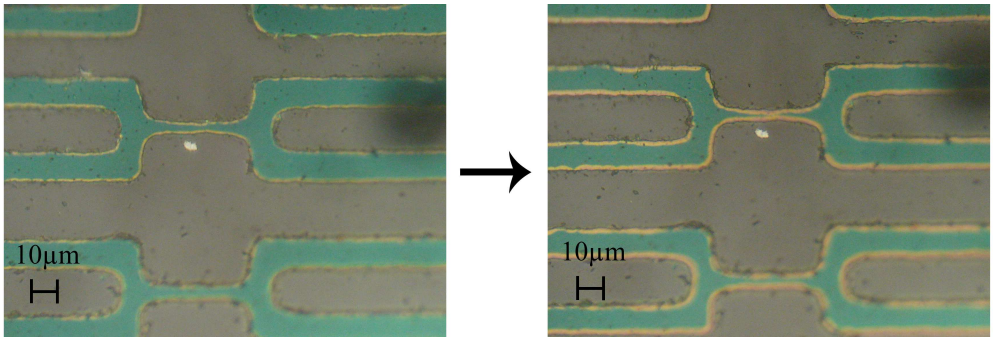

Figure 2.14: Diagram showing the increase of inhomogeneity of the width of a narrow YBCO wire after an acid etch.

This is exactly the opposite effect that argon ion beam milling has on a wire, where defects are reduced over time. This is because the defects shadow the surrounding area from the beam, causing them to receive a higher flux

of ions. This means that protuberances are milled at a higher rate than the surrounding area, which causes a general polishing affect. Therefore I decided to subsequently concentrate on argon ion beam milling for the successive reduction of wire width, rather than an acid etch.

Chapter 3

Fabrication

In this chapter I shall describe the techniques used to fabricate the superconducting nanowires. The same general methodology was used to produce all of the samples in this project. First a thin film (100nm - 200nm thick) of the material being studied was patterned into the desired shape using photolithography. This produced a minimum wire size of 4μm by 6μm. To reduce the sample size to the nm range two techniques were used, focused ion beam milling (FIB), and electron beam lithography (EBL). The wires produced by FIB had a length of 8μm and a width of 100nm-300nm, and those produced by EBL had a length of 1μm and width of 100nm. The final fabrication stage was to reduce the sample size further using an argon ion beam miller, employing a technique developed to allow for controllable reduction in wire dimensions at the sub 100nm level. An an atomic force microscope (AFM) and a scanning electron microscope (SEM) were used to measure samples and characterise the fabrication process.

3.1 Materials

3.1.1 Niobium

There are several reasons why niobium was chosen for investigation in this project. Having a T_c of 9.25K, several degrees above the boiling point of liquid helium, means that the transition of niobium can be measured relatively easily by use of a continuous flow cryostat. This means that the R(T) characteristics can be obtained relatively quickly compared to materials with a lower T_c, which would need more advanced cooling to see any effects. The drawback of having a large T_c is that niobium has a relatively short coherence length. This means that wires made from niobium have to be smaller than other materials to be considered one dimensional.

One very useful feature of niobium is that it has a strong contrast difference with respect to a silicon substrate when imaged with a normal SEM. This is very useful when characterising the fabrication process as the interface between the two materials can easily be seen, and hence the dimensions of a wire easily measured. This is an advantage over work done on aluminium wires [11], where the difference between the wire and substrate cannot be seen directly. In that case, measurements were done using an AFM and the height of the wire inferred from a separate measurement of the substrate height (Chapter 2 Fig. 2.9).

The superconducting properties of niobium are listed in 3.1.

Table 3.1: Superconducting properties of Niobium [21]

$T_c(K)$	$\lambda_L(nm)$	ξ_0 (nm)	$H_c(0)$ (A/m)	$\Delta(0)$ (meV)
9.25	85	30	2.59×10^{-7}	1.520

3.1.2 YBCO

$YBa_2Cu_3O_{7-\delta}$ (YBCO) is a high temperature superconductor (HTS) with a transition temperature of $\sim 90K$. This material was chosen for investigation to continue the previous work on phase slips in YBCO [25]. The aim was to ascertain whether phase slips can really occur in YBCO or if another effect causes the broadening of the transition.

Superconductivity in YBCO depends on the CuO layers in the crystal structure. The structure contains CuO planes and chains along which the supercurrent mainly flows. The superconductivity of YBCO is critically dependant on the oxygen content of the crystal, and if there is not enough oxygen to form the CuO chains, then superconductivity does not occur. The crystal structure of YBCO and the effect of oxygen content is shown in Fig.(3.1). Because the superconductivity of YBCO is sensitive to oxygen loss, care had to be taken to ensure that the samples were fully oxygenated.

The size of a unit cell of YBCO is $\sim$ 0.4nm in the a and b axis, and $\sim$ 1.2nm along the c axis. Because of the anisotropic crystal structure, the superconducting properties of YBCO are different in the ab plane compared to the c axis Fig.(3.2).

Table 3.2: Superconducting properties of YBCO [29][25]

T_c (K)	λ_{ab} (nm)	λ_{ab} (nm)	ξ_{ab} (nm)	ξ_c (nm)	$H_c(0)$ (A/m)
92	150	600	1.5	0.4	1.76×10^{-6}

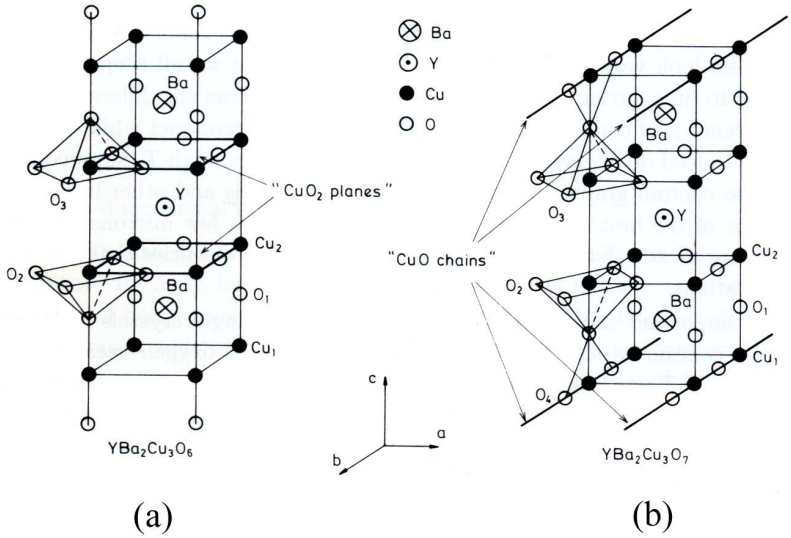

Figure 3.1: The crystal structure of (a) $YBa_2Cu_3O_6$ an insulator and (b) $YBa_2Cu_3O_7$ a superconductor [28].

Phase slips were reported in YBCO [25] in wires with a width of 500nm, much larger than the coherence length. Therefore, if phase slips do occur in YBCO, the current must be restricted inside the material is some way. The method proposed was that the supercurrent in YBCO is restricted into narrow filaments. This supported work on 2D films of YBCO where an increased resistivity was observed before the wires turned superconducting [30] [31]. This effect was attributed to phase-slip behaviour occurring in narrow 2nm wide filaments.

3.2 First Fabrication Steps

3.2.1 Films

The Nb thin films were bought from a company, Starcryo, who specialise in the deposition of high quality niobium thin films. A range of film thickness' were used, 600nm to calibrate the milling process and 100nm and 200nm to fabricate the narrow wires. They were deposited on an insulating doped silicon.

Initially, YBCO films were grown using pulsed laser deposition, however, the quality of the films produced was very variable. It was decided that buying films would save time, as it would have taken a large amount of work to refine the growing process to produce very high quality YBCO films. The films were bought from a company, THEVA, who specialise in high quality, smooth thin films. The films were deposited using an evaporation of the constituent elements, followed by a sintering in oxygen, and finally covered in a layer of gold in situ. The gold served two functions, it allowed for electrical contacts to be made to the samples using Al wire bonds, as the adhesion of Al wire bonds on YBCO is poor. The Au adheres well to both the YBCO and the Al wire bonds, so is the ideal interface material. Au does not readily absorb oxygen and so the layer also protected the oxygen content in the YBCO, preventing it from diffusing out during the storage of the films.

3.2.2 Photolithography

The thin films were patterned into the correct shape using standard photolithographic techniques. A versatile photo-mask was designed to allow for a range of different fabrication processes. This included masks for chemical etching, ion beam etching, lift-off, e-beam lithography, edge bead masks and contact pads masks.

The photoresist used for all of the experiments was AZ5214E, and the corresponding developer was MICROPOSIT MF-319. This was a positive photoresist, meaning that the area exposed by UV-light was the area that would be removed when developed. The thickness of the photoresist layer is an important parameter when fabricating samples. The smallest features that can be produced by photolithography are not only limited by the wavelength of the UV-light, but also but the thickness of the photoresist. With a very thin layer of photoresist ($\sim$200nm) the smallest feature that was produced was 2μm wide. However, it was difficult to consistently produce such thin photoresist layers.

A compromise was made in the design of the photo-mask to allow for thicker photoresist films. The smallest features were designed to be 4μm rather than 2μm to allow for some leeway in the fabrication process. It was found that features 4μm in size were relatively unaffected by the thickness of the photoresist. This meant that photoresist films up to a thickness of 1μm could be used. This was also important with the milling of thick Nb films as the mill rate of the photresist is round 4 times higher than Nb. This means the photoresist film had to be at least 400nm when milling a 100nm thick

Nb film.

The thickness of a photoresist film can be controlled by spinning the resist at different speeds. The most frequently used spin setting were: 500rpm for 10s, followed by 5500rpm for 40s, followed by a final 500rpm for a further 10s. This produced a film $\sim 1\mu$m thick.

The samples were then baked for 1min at a temperature of 100°C, before being exposed to UV-light, under the desired mask, for 11s using a KARL SUSS MJB3 mask aligner. Then the samples were developed and baked again at 100°C for up to 5mins before being ion beam milled. After milling the photoresist was washed off with acetone. This produced the pattern shown in Fig. 3.2.

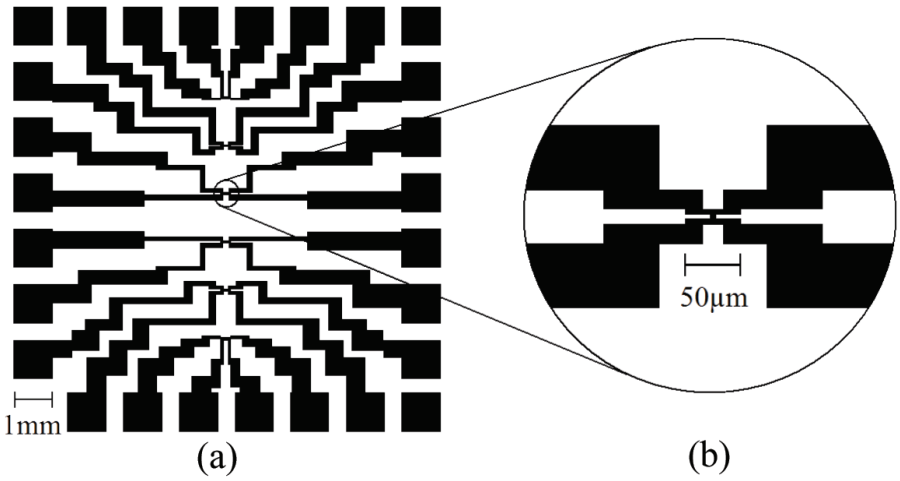

Figure 3.2: The pattern used for photolithography. Six samples can be produced per substrate. Each sample has four contacts, to allow for four terminal measurements.

The central region in Fig. 3.2(b) had a width of 6μm and length 4μm and was the region used to produce a very narrow, sub-micron wire. To produce

these narrow wires, two methods were used, focused ion beam milling and e-beam lithography.

3.3 Techniques Used

Several fabrication techniques were used to produce the nanowires in this project. Each of these techniques is described in this section.

3.3.1 FIB

Focused ion beam milling is a process by which one can very accurately mill a material using a beam of accelerated gallium ions. The ions are produced by applying a large electric field to a sample of liquid gallium. The ions are then accelerated and focused into a beam with spot size 30nm using electronic lenses. This beam can then be used to etch materials in a very controlled way.

The system used in this project was a dual beam Strata DB235 xP FIB/SEM workstation based in the department of Mechanical Engineering at the University of Birmingham. The advantage of a dual beam system is the ability to view the sample with the SEM without damaging it, as imaging with the FIB also etches the sample. The beam current used was 30pA, and an ion energy of 30keV.

FIB is a good method to use to produce narrow wires as it can mill away material very accurately to produce wires as narrow as 100nm, with length up to 10μm. It is a reasonably new technique that has not been widely used to produce ultra-narrow wires. The main advantage over other

nano-fabrication techniques, such as e-beam lithography is that the entire fabrication of a nanowire can be done in a single machine. To obtain the same results with e-beam lithography, several fabrication steps need to be made as described in the next section.

There are, however, several ancillary effects of the milling process that need to be considered when fabricating samples. The most important of these are surface charging and gallium implantation.

Surface Charging

Sample charging occurs when the electrical conductance of the material being milled is low. The result of charging is a deflection of the ion beam away form the charged region, resulting in less focused milling. Niobium and YBCO have a high enough conductivity to prevent significant charging, however, by necessity they are grown on resistive substrates. This was an issue when fabricating long thin wires as the trapped charge would affect the accuracy of subsequent mills. This problem was largely overcome by shorting the films to the sample stage by using silver paint, however some residual charging effects were still evident which limited the reproducibility of 100nm wires.

Gallium Implantation

Because the gallium ions have a large kinetic energy they can become implanted in the target surface and change the chemical composition [32]. This is an important effect as it can destroy the superconductivity in the surface of a wire. The implanted gallium can also cause a heating effect as the kinetic energy of ions is transferred into phonon vibrations of the lattice. This can

be an important effect in YBCO as heating above ∼200°C [33] allows the oxygen to become mobile and diffuse out. Temperature increases in a $SrTiO_3$ from a 100pA, 25kV Ga ion beam have been estimated to be of order 1K [34]. This level of heating would be negligible for oxygen loss in YBCO, however as FIB milling is a highly localised effect it is difficult to use macroscopic models to describe it. Both chemical implantation and oxygen loss result in a superconducting region that is less than the physical size of the wire.

The depth of penetration of gallium ions were be estimated using a computer modelling program, SRIM (Stopping Range of Ions in Matter). For 30keV gallium ions, the depth of penetration into an YBCO and Nb films are roughly the same: ∼30nm, with a lateral spread of 20nm either side of the central beam (Fig. 3.3).

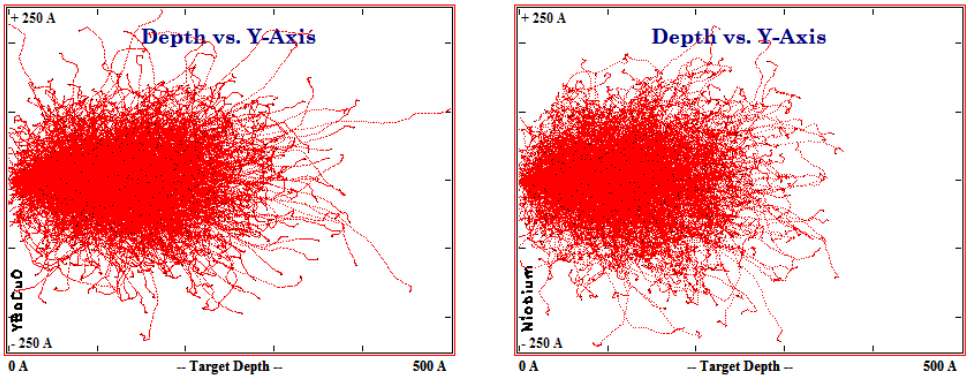

(a) (b)

Figure 3.3: The scattering paths of 2000, 30keV gallium ions in (a) YBCO and (b) niobium using SRIM analysis. Note: the sale is measured in angstroms.

3.3.2 E-Beam Lithography

E-beam lithography is a powerful technique that can be used to fabricate very small devices using a method very similar to photolithography. A photosensitive polymer is exposed by a very narrow beam of electrons and then developed. This can be used to produce a pattern in the photoresist, with a minimum feature size as small as ∼10nm. The e-beam system used in this project was a converted Hitachi S-4300 SEM based at the University of Bath.

A procedure was developed to fabricate very narrow wires in Nb using e-beam lithography. To do this an aluminium etch mask was patterned on the surface. This then protected the Nb in a reactive ion etcher. So the pattern that was desired in the Nb first had to be fabricated on top in Al.

First, Al was deposited onto a thin Nb film, and then patterned into the desired shape using photolithography. This produced a pattern identical to that produced for the FIB (Fig. 3.2), except that the central connection between the 4 contacts was not made (Fig. 3.4(a)). This left room for a very narrow wire to be fabricated in the middle of the 4 contacts (Fig. 3.4(b)), and this was done using EBL and a lift off technique .

To fabricate the very narrow wire, the sample was covered in PMMA (Poly methyl methacrylate), a polymer that is sensitive to exposure to electrons. This layer was then exposed in the desired shape using the EBL according to the pattern shown in Fig. 3.4(b). This was then developed, which produced a gap in the PMMA which defined the shape of the final wire. Al was evaporated over the entire sample, and through this gap in the PMMA, producing a narrow wire. Finally, the PMMA with Al on top was

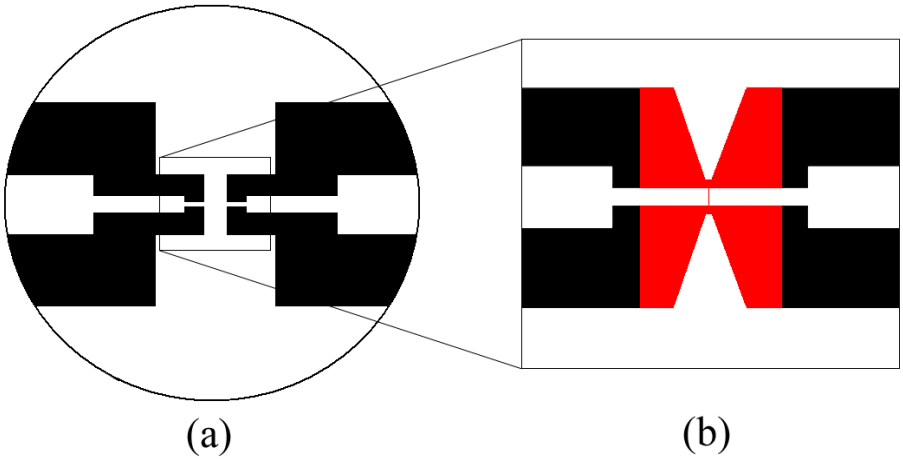

Figure 3.4: The shape of the Al layer after patterning. A gap is left between the four contact wires to allow for the EBL phase. The red section denotes the area that is covered in Al after the EBL process is complete.

removed by washing in acetone, the so called 'lift-off' technique.

This left a film of Nb with a patterned Al layer on top. To transfer the pattern into the Nb, the sample was etched using Reactive Ion Etching (RIE). This involves exposing the sample to a chemical ion plasma which selectively etches Nb but not Al, in this case SF_6 (Sulfur Hexafluoride). This transferred the Al pattern into the Nb film. The Al was then subsequently removed with the photoresist developer (MICROPOSIT MF-319), which was found to etch Al.

Because of the intricacies of this procedure, a lot of characterisation was required. The most critical step was to be able to expose the PMMA correctly. There were several parameters that limited the minimum size for the exposure including, the thickness of the PMMA layer, the focus of the e-beam and the amount of dose given to each section exposed. Details of this process are explained later in this chapter.

3.3.3 Argon Ion Beam Milling

Argon ion beam milling is a technique used to homogeneously mill thin films using an ionised argon beam. This differers to focused ion beam milling in that the beam is large (50mm wide) and uniform across most of the diameter, only tailing off at the edges. Also, the energy of the incoming ions is relatively small, typically less than 1keV compared to 30KeV for FIB. The Ar ions can become implanted in the target material, just like Ga ions in FIB milling. However as the beam energies are a lot smaller the implantation depth is a lot less. SRIM simulations predict the implantation depth to be in the range of ∼2nm for Nb and YBCO Fig.(3.5).

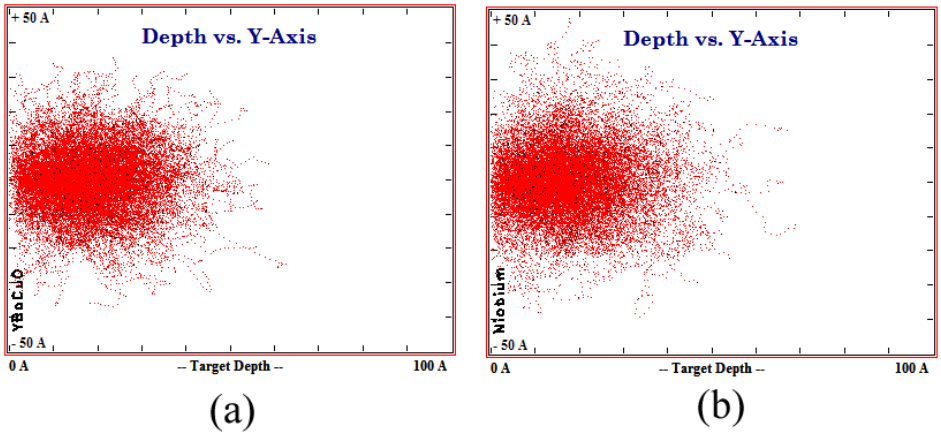

Figure 3.5: The scattering paths of 2000, 1keV argon ions in (a) YBCO and (b) niobium. Note: the sale is measured in angstroms.

For this project, an Oxford Applied Research IM150 ion milling system, with a 13.56 MHz RF ion source was used. In this system a sample could be mounted at any angle with respect to the beam, and also rotated during milling. The system had an attached mass spectrometer which detected the

materials that were being sputtered from the sample, and was used to see when a thin film had been milled through (end point detector).

To keep the results consistent, the settings used to control the beam were kept the same throughout the project. These settings produced a homogeneous beam, with argon ions hitting the sample stage with ∼500eV of energy. The only variables that were changed were the angle of the sample with respect to the beam, and the time the sample was exposed to the beam. As with FIB, the Ar ions cause heating of the sample being milled which can lead to oxygen loss in YBCO [35] (and references therein). YBCO samples that are heated in a vacuum are particularly susceptible to oxygen loss due to the combined effect of heating and vacuum pumping. In the system used, the sample stage was cooled to minimise this effect as far as possible. To reduce the chance of oxygen loss further a lower beam energy could have been employed.

Rotating the sample during milling produced a polishing effect on the films being milled. This polishing effect is allowed for the production of very narrow wires as any inhomogeneity in the width of a wire was reduced during milling. The mechanism of this polishing effect is caused by protuberances from the surface being preferentially milled with respect to the surrounding material because of shadowing. This is schematically shown in figure (3.6).

Ion beam milling is generally used to mill thin films as the final step of lithographic patterning, and this is one of the ways it was used in this project. However, another very useful application of ion beam milling is to controllably reduce the width and height of narrow wires as developed by [11]. The characterisation and results of this process are described in section

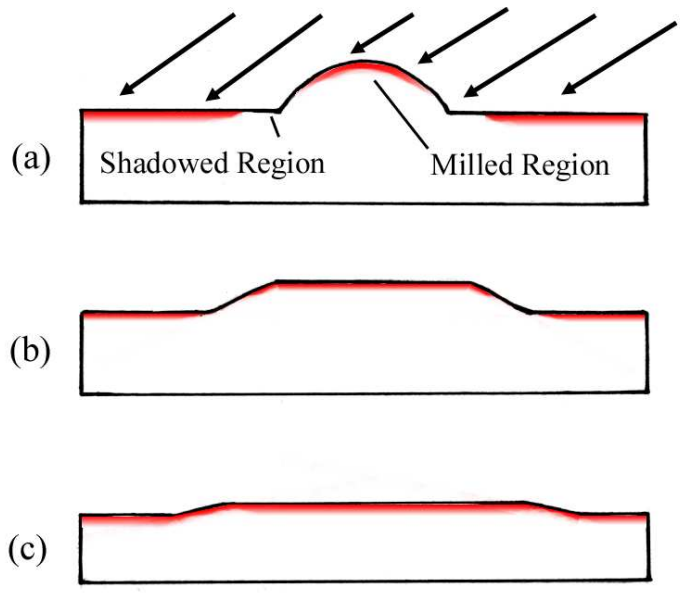

Figure 3.6: As the sample is rotated in the ion beam a shadowing effect causes protuberances to be milled more than the shadowed region (a). This produces a flattening on any inhomogeneity during milling (b)(c), resulting in a general polishing effect.

3.6.3.

3.3.4 AFM

An atomic force microscope was used in the fabrication process to measure the wires produced and to characterise both the FIB and Ar^+ milling process'. The AFM used was a a Dimension 3100 Nanoscope AFM (Veeco, UK) operated with the help of Dr. J. Bowen, a research fellow at the department of Chemical Engineering. The software used to control the AFM and analyse the results was Nanoscope v5.12 software (Veeco, UK).

To measure the wires the AFM was used in contact mode with a high

resolution tip. Because the tip was not perfectly sharp it added to the lateral dimensions of the objects being measured. Calibration showed that a new tip added 30nm to lateral dimensions which increased as the tip degraded. The vertical resolution was much better $\sim$ 1nm, and was not affected by tip degradation. An example of the measurement produced by the AFM is show in figure(3.7).

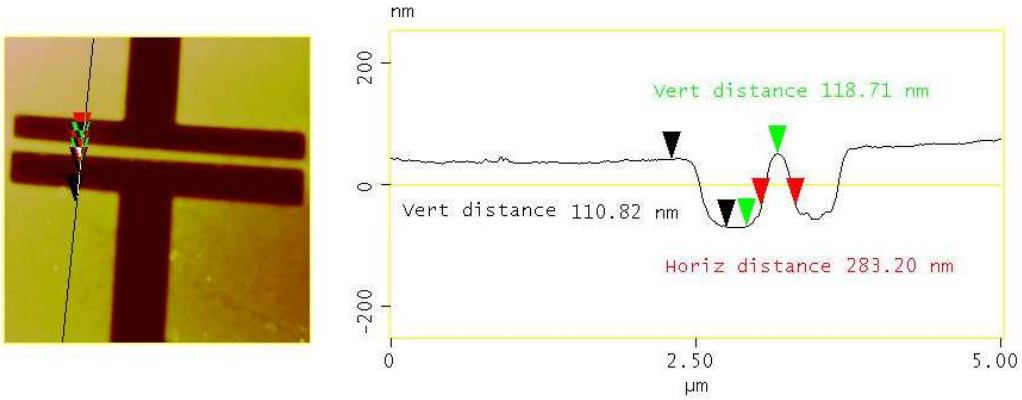

Figure 3.7: Example of the data collected from the AFM. The vertical resolution was $\sim$ 1nm. Because of the tip size the AFM added 30nm to lateral dimensions.

3.3.5 SEM

The wires produced were also measured with the SEM based in the FIB system. When measuring niobium wires, the SEM could resolve the contrast between the Nb and Si substrate. This allowed for the measurement of the wire height after milling, a measurement not possible using the AFM. The resolution of the SEM was $\sim$ 10nm, where focusing was the main limitation. The measurements were made using the SEM software (Fig. 3.8).

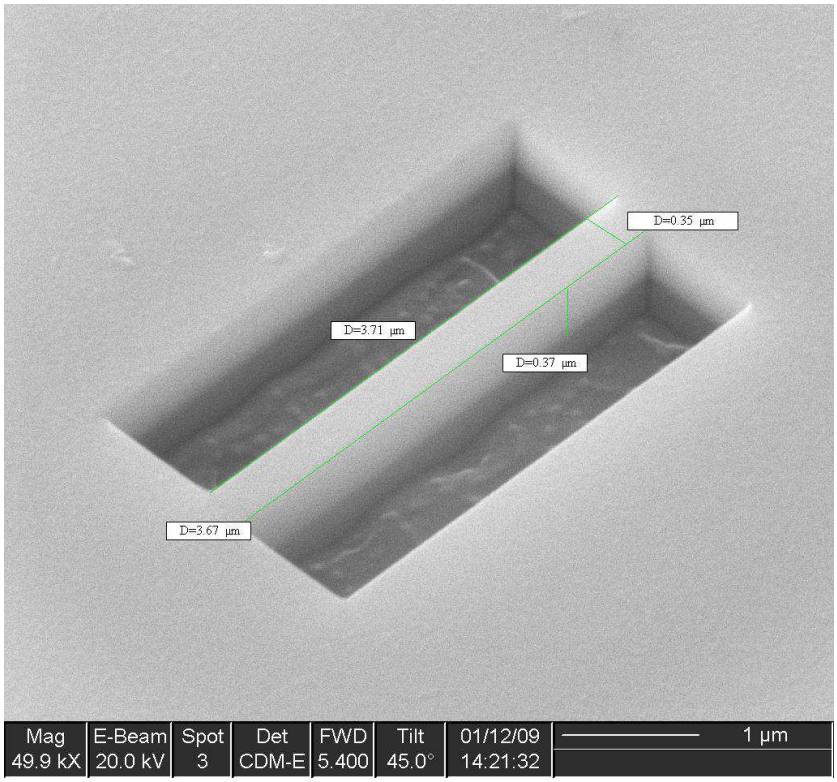

Figure 3.8: Example of an SEM scan and measurements. Because some images were scanned at an angle to the features being measured, the measured size was corrected accordingly.

Measuring sample sizes below 100nm was difficult as the samples were not as square shaped as Fig.(3.8). Taking measurements of the wire with was easy as the sample could be measured from above (Fig. 3.9(a)), however to determine the wire height measurements were made at 60° to the normal (Fig.3.9(b)). When it was very difficult to resolve the height of the wire, several measurements were made at increasing angles, and the wire shape extrapolated from this data.

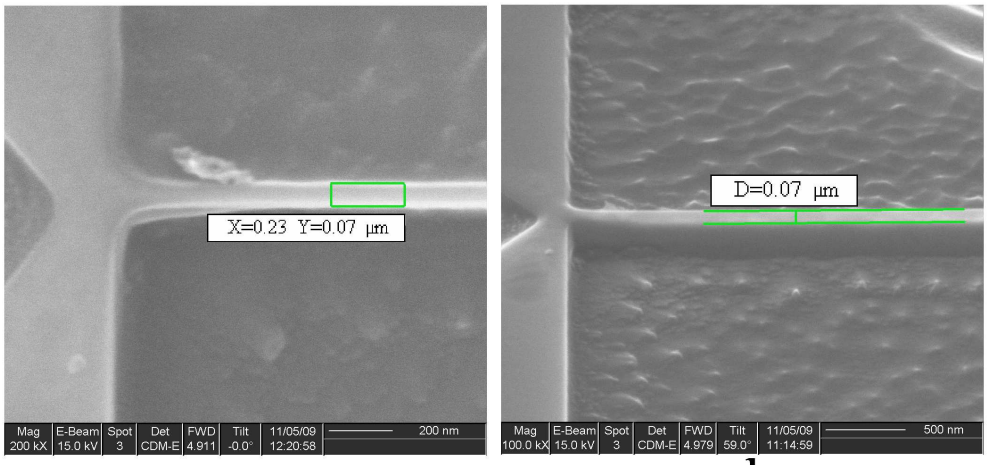

Figure 3.9: The same wire measured at an angle of 0° (a), and 60° (b). The wire width and height is extrapolated from these measurements.

3.4 Fabrication Results

3.4.1 FIB Results

To produce narrow wires in Nb and YBCO using the FIB the mill rate of each material needed to be characterised. The mill rate depends on the current of the beam, and the energy of the ions, both of which could be controlled. The advantage of having large current/energy of the beam is a reduction of pattering times. However this also increases distance over which the gallium ion become implanted in the superconductor. Because implantation is a significant issue, a low beam current of 30pA and an accelerator voltage of 30kV was used.

The mill rate of Nb using these settings was found by producing a series of test squares with increasing mill times. The depth of these could then be

measured en situ with an SEM to ascertain the mill rate. Because Nb has a strong contrast difference to the Si, it was clear when the sample had been milled through.

This technique could not be applied to YBCO because there was no contrast difference between the film and the substrate. In this case a calibration was made by milling a series of test squares in an YBCO film for different times, and then measuring the depth of each square with an AFM. This gave an estimate of the mill rate of YBCO. Also, the by-products of the FIB milling could be monitored in real time on an oscilloscope, and here a contrast between the material ejected from YBCO and the substrate could be seen. This offered good indication as to when the film had been milled through.

Several different designs of pattern were used throughout the course of the project. The main problem of design was producing a 4-terminal contact to the wire to allow for good electrical measurements. The design pattern needed to be simple as any complicated patterns would be harder to reproduce, and would increase the process time significantly. Also, the pattern had to allow for the sample to be subsequently reduced in size using an ion beam miller, so made in such a way that the wire would be the narrowest feature. The final design is shown in Fig. 3.10.

The pattern produced in figure (3.10) is a pseudo 4-terminal measurement as the current and voltage leads meet before the wire. This means that the voltage leads will measure the voltage of the small portion of superconductor either side of the wire as well as the wire itself. However because the T_c of both niobium and YBCO goes down with sample size, this portion

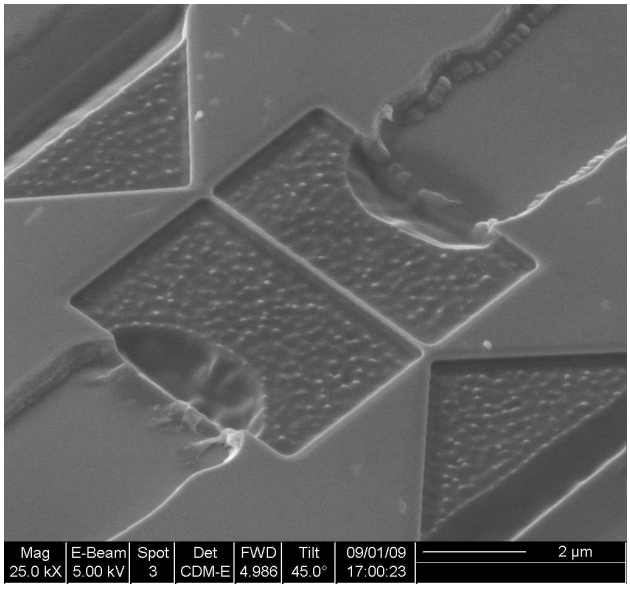

Figure 3.10: A niobium film milled using the FIB. The central wire is 8μm long and 100nm wide. This pattern was made using 4 milling shapes from the original features left from the photolithograpy stage.

will become superconducting before the nanowire, and so will not effect the measurement of the resistance.

3.4.2 EBL Results

The production of nanowires using electron beam lithography required several processing stages. The most critical of these steps was the application and exposure of the PMMA layer. There are many variables that affect the minimum size of wire that can be fabricated. These include, the thickness of the PMMA layer, the alignment of the e-beam pattern, the dose given to each part of the e-beam pattern, and the length of time the exposed PMMA is developed. The process was set up in collaboration with Prof. S. Bending and Dr. S. Landi during a number of visits to The University of Bath. The

process was further characterised and refined by Dr. S. Landi, and it was he who produced the smallest wires.

The PMMA layer needs to be thin to produce very narrow wires, in this case a 200nm layer was used. This was controlled by the speed of a spinner. There were initially some problems with the PMMA becoming grainy, but these were solved by using a new batch.

The alignment of the e-beam pattern (Fig. 3.4(b)) is critical as it is made up of several shapes that are individually exposed in sequence. The effect of poor alignment is shown in Fig.(3.11). In this case the problem was due to an inaccuracy of the hardware. This was solved for later experiments as, over the course of the project, the hardware and software of the EBL machine was upgraded.

Each shape in the e-beam pattern is assigned a dosage. The dosage is the amount of time the shape in the pattern is exposed for by the electron beam. The dosage values are critical because the pattern becomes overexposed if it receives a larger dose then is needed. This means that too much of the PMMA is exposed creating larger features. To find the correct dose for the pattern a test array was created that systematically covered the various dose combinations.

The development time of the PMMA was important for the same reasons as the dose. If the PMMA was developed for too long the small features in the pattern became too large. To find the correct development time, several samples were developed for different times, the optimum time was found to be 15s.

The results of this process was to successfully produce some sub 100nm

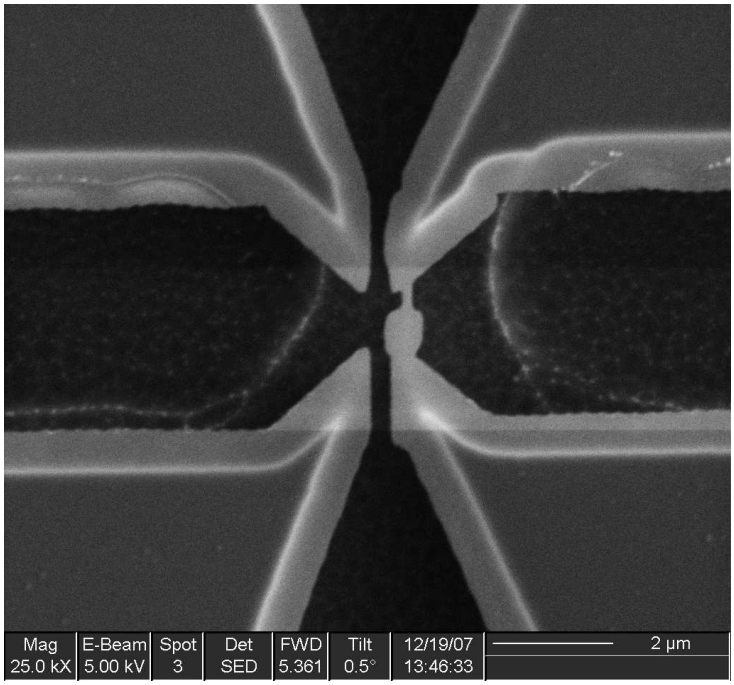

Figure 3.11: The effect of misalignment of the electron beam pattern. The central narrow wire is slightly off centre causing it to not be fully connected to the contacts.

wires in Al. Although the process was designed to produce Nb wires, the samples were over-etched in the final reactive ion etching stage. This produced the wire shown in fig. 3.12.

Although no Nb nanowires were produced using the e-beam lithography fabrication, the over etching produced 4 aluminium nanowires. Unfortunately the contacts leading to the nanowires had not been fabricated correctly, which meant that the wires could not be measured.

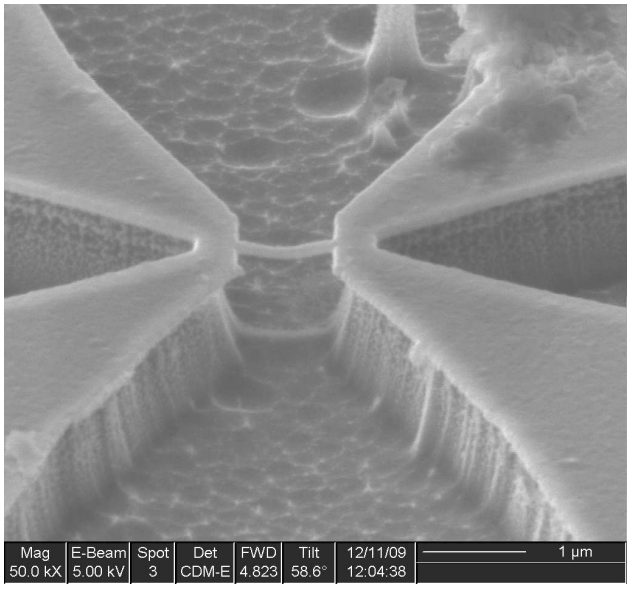

Figure 3.12: A sample produced by the e-beam lithography fabrication process. The sample has been over etched in the RIE leaving a haging nanowire of Al. The wire is 1μm long and 100nm wide and thick.

3.4.3 Argon Ion Beam Milling Results

Argon ion beam milling was used to produce a reduction of Nb wire size after the wires had been fabricated using FIB. This was done by milling the wire at an angle to the Ar^+ beam, and under rotation. The samples were rotated while milling to ensure that they were milled evenly.

This work on ion beam milling follows an experiment [11], where Ar^+ beam milling of aluminium nanowires produced an even reduction of height and width. The milling angle they used was 60° to the normal. This enabled the group to reduce the dimensions of their wires by a factor of ten from 100nm by 100nm to as small as 11nm by 11nm. This was only possible by milling the wires at such an angle that maintained a relatively even cross section.

My initial attempts to reproduce these results in wires of Nb were unsuccessful. When milling at 60° and under rotation a Nb wire with a square cross section would become rectangular after milling, rather than maintaining a square cross section as in Ref.[11]. The top of the Nb wire reduced faster than the sides, leading to a squat rectangular wire and limiting the minimum size.

For a wire to be considered one dimensional it is important that is has a relatively even cross section. This is because the superconducting wavefunction needs to be suppressed in all dimensions apart from along the length of the wire. If the wire is rectangular in cross section, for example its width greater than its height, the wavefunction may be suppressed along the height, but not the width, causing it to behave like a 2D film. In this situation the wire would be completely milled away before it was narrow enough to to behave one dimensionally.

Therefore, it was critical to find the correct angle with which to mill Nb and obtain an even reduction in width and height. For this I needed to characterise the angular dependency of the mill rate of Nb. The angular dependency of the mill rate of several materials, unfortunately not including niobium, is shown in Fig.(3.13) [36].

I began the investigation by characterising the mill rates of several materials used in the project at a single milling angle of 60°. These included Nb and the substrate Si, and YBCO and the substrate YSZ, and for comparison Al. This characterisation was done by covering a film of the material in photoresist, and then patterning a series (6 or 12) of square holes in the photoresist using photolithography. The samples were then milled several times,

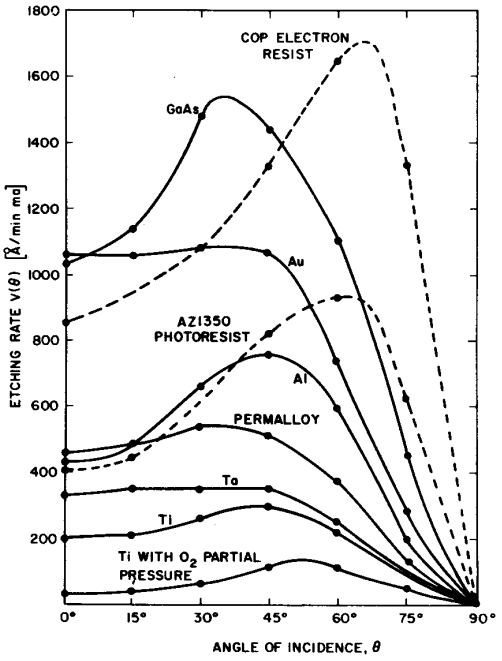

Figure 3.13: The mill rate of several different materials at different milling angles to the normal. The acceleration voltage was 500V, argon gas pressure 1×10^{-4} Torr, and current 0.6 mA/cm^2 [36] (Note: mill rates are in Å/min.)

each time covering one of the squares with photoresist sequentially. Finally the photoresist was washed off leaving a series of squares each milled for a different amount of time. The depth of each of these squares was measured using an AFM, and the data produced the mill rate of the various materials. These are shown in figure 3.14.

This gave an idea as to the relative mill rates of the different materials. Notably Al has twice the mill rate of Nb. The next step of the investigation was to characterise the mill rate as a function of angle milled. This was done for Nb, Si, and YBCO, and deduced for Al using Fig.(3.13).

To find the angular dependency of the mill rate of Nb, Si and YBCO six

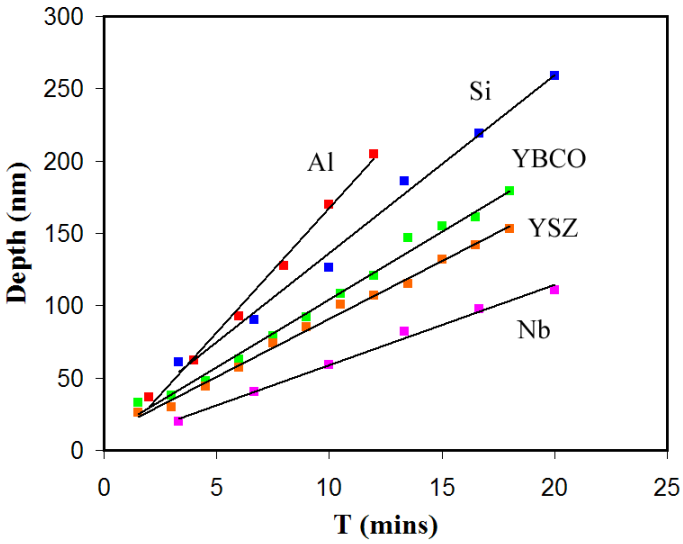

Figure 3.14: The mill rates of several materials used in the project. The Al was milled at 45°, whereas the the others were milled at 60°. This gave a rough comparison of the relative mill rates of the materials. The mill rates according to the linear fits are: Al = 17nm/min, Si = 12nm/min, YBCO = 9.4nm/min, YSZ = 7.8nm/min, Nb = 5.5nm/min.

samples of each were milled at different angles to the normal. 600nm thick films were used, and half of each film was covered in photoresist to protect it from the ion beam. They were each milled at an angle between 0° and 75°, at increments of 15°. After milling, the photoresist was removed resulting in a step in each film, the height of which depended on the angle milled. As the mill rate of niobium had been found to be $\sim$ 5.5nm/min, and YBCO $\sim$ 9.4nm/min, the samples were each milled for 30mins, giving an expected depth of 165nm and 282nm respectively. This was well within the 600nm thickness' of the films.

Also, before ion beam milling, wires were milled into each of the Nb films using an FIB, producing a large wire of cross section $\sim$ 500nm $\times$ 500nm,

and length 4μm in each of the films. This was done to see how milling at different angles would effect square wires.

After ion beam milling for 30 mins, the photoresist was washed off with acetone, and the step edges were measured with an AFM. The results are shown in Fig. 3.15.

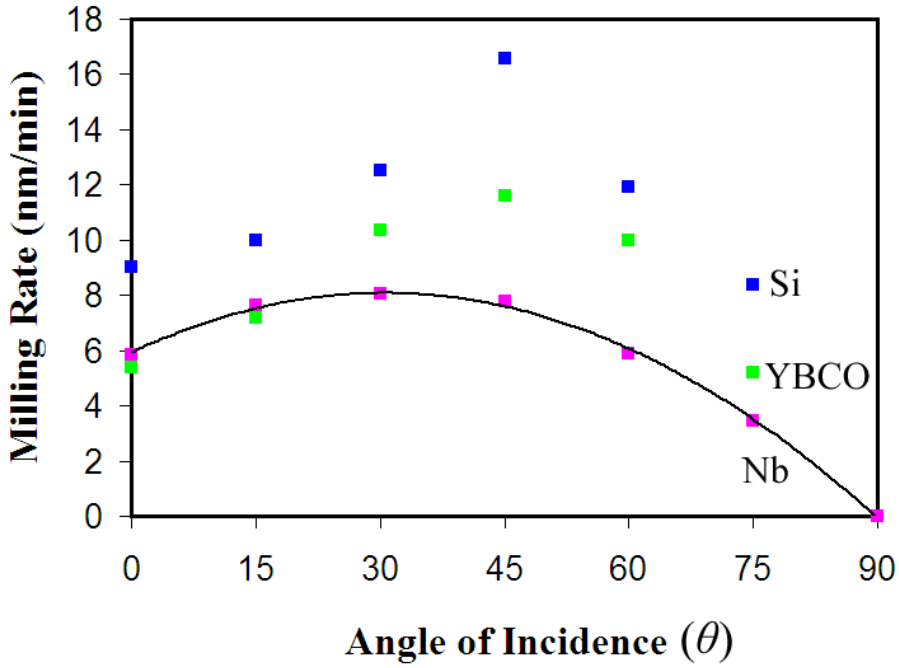

Figure 3.15: The mill rate of Si, YBCO and Nb as a function of milling angle from the normal to the film. The Nb has been fitted by a second order polynomial, -0.0023 θ^2 + 0.14 θ + 5.9.

Comparing Fig.(3.15) with the Al plot from Fig.(3.13), we see the maximum mill rate is at 45° for Al and 30° for Nb. The different dependencies of mill rate on angle is likely to have been the reason why milling Nb at 60° did not produce an even reduction of the height and width of the wire, as it did with Al [11].

The different milling angles had a large effect on the shape of the wires that had been fabricated in the Nb films. When milled at 0°, the wire went from being square in cross section to triangular. This was also true for 15°. At 30° the square wire became trapezoidal, and at larger angles the wires maintained a rectangular shape. These effects are summarised in Table.(3.3) where SEM images of the wires are shown before and after the ion beam mill, along with schematic diagrams of the wire cross sections. The measurements shown on the schematics are taken from measurements of the SEM images of the wires before and after milling. These were made using the SEM software, and have an error of roughly ±10nm. This error was due to the difficulty of interpreting the shape of the wire accurately from the images. However, the major advantage of this technique was the ability to clearly resolve the boundary between the Nb film and the Si substrate, as can be seen in the images.

The reason why the wires exhibited a range of cross sectional shapes after milling follows from a simple explanation. Because the maximum mill rate is at 30° to the beam, any surface at this angle will be milled faster than any other, and so will become more prominent. The triangular wires were produced by the corners of the rectangle being milled at the fastest rate until they dominated the shape of the wire. At larger angles, 45° and above, the corners were perpendicular to the beam and so got milled at a slower rate than the sides, causing the rectangular shape to be maintained. Milling at 30° showed the crossover between these two regimes.

It is important to note that the rotation of the samples also has an important effect. Because of rotation, the sides of the wires periodically come in

Table 3.3: Effect of different milling angles on square wires with schematic diagrams of the initial and final cross-sections.

Angle	Before	After	Before (nm)	After (nm)
0°	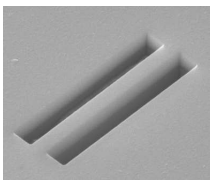	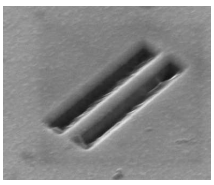	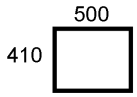	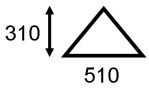
15°	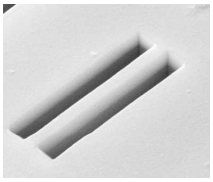	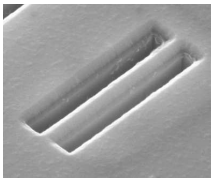	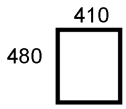	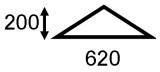
30°	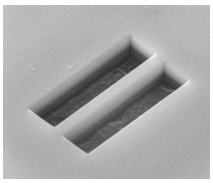	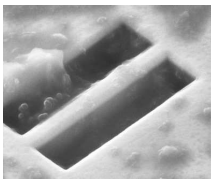	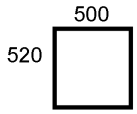	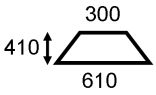
45°	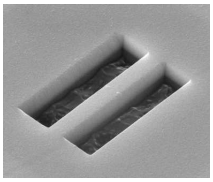	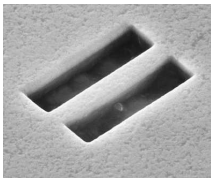	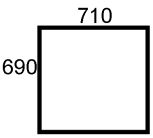	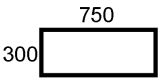
60°	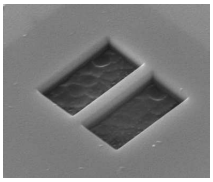	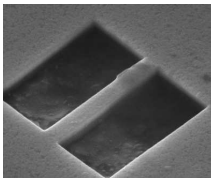	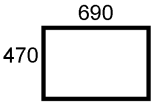	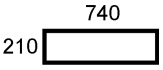
75°	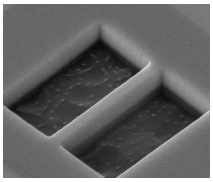	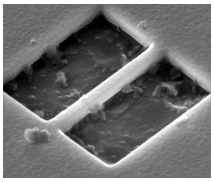	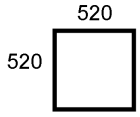	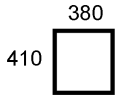
90°	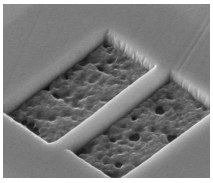	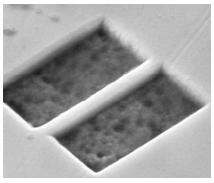	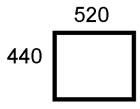	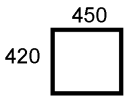

and out of view of the beam. This means that they see the beam for a much shorter time than the top of the wire, and are milled at a varying angles and hence at a varying rate. Without rotation, milling at 45° should produce an even mill of the top and a side of the wire, and this was indeed seen in one sample. However, milling without rotation had the drawback of increasing surface roughness, whilst milling under rotation creates a polishing effect [11]. Therefore, the angle that produces an even mill of the top and sides of a wire under rotation is larger than 60°, the results in Table 3.3 suggesting it is in the region of 75°. The ideal angle can be formally calculated by using the angular dependency of the mill rate. This is covered in the next section.

3.4.4 Theoretical Calculation of Ideal Mill Angle

To find the best angle for milling under rotation, one needs to calculate which beam angle will mill the top and sides of a wire at the same rate. Because the wire rotates in the beam, the milling rate of the side walls of the wire is time dependent. Therefore, one needs to calculate an average value for the mill rate of the sides, and compare this to the constant mill rate for the top of the wire. This can be done by integrating the mill rate of the sides of the wire over a full rotation, and then dividing by 360°.

A diagram showing the direction of the ion beam with respect to a wire is shown in Fig.(3.16).

Figure(3.15) shows the mill rate of niobium depending on the angle to the *normal* of the substrate. This can be written as $R = a\theta^2 + b\theta + c$, where a, b and c are the constants -0.0023, 0.14 and 5.9 respectively, obtained from

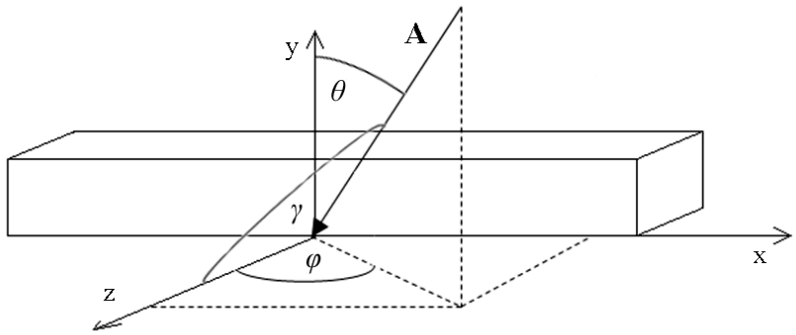

Figure 3.16: The vector $\boldsymbol{A}$ shows the angle of the ion beam with respect to the wire. The wire is rotated about the y-axis, causing a variable mill rate on the sides of the wire over time.

a least squares fit to figure(3.15). According to figure(3.16), the angle of the beam from the normal to the *side* of the wire is given by γ. As the wire is rotated around the y-axis in the beam this angle will change over time. From simple vector algebra, the angle γ can be written in terms of θ and ϕ as,

$$cos\gamma = sin\theta cos\phi. \tag{3.1}$$

The mill rate of the side of the wire is therefore given by,

$$R = a\gamma^2 + b\gamma + c = a\left[cos^{-1}(sin\theta cos\phi)\right]^2 + b\left[cos^{-1}(sin\theta cos\phi)\right] + c. \tag{3.2}$$

The average mill rate of the side of the wire is then given by,

$$R = \frac{2}{\pi}\int_0^{\frac{\pi}{2}} a\left[cos^{-1}(sin\theta cos\phi)\right]^2 + b\left[cos^{-1}(sin\theta cos\phi)\right] + cd\phi. \tag{3.3}$$

Solving this integral numerically, one obtains a range of different average mill rates depending on the angle milled. Homogeneous milling of a wire is expected to be produced when the average mill rate of the sides of the wire equals the mill rate of the top. Comparing the mill rates of the top and sides of the wire (Fig.3.17) this is shown to be $\sim 61°$.

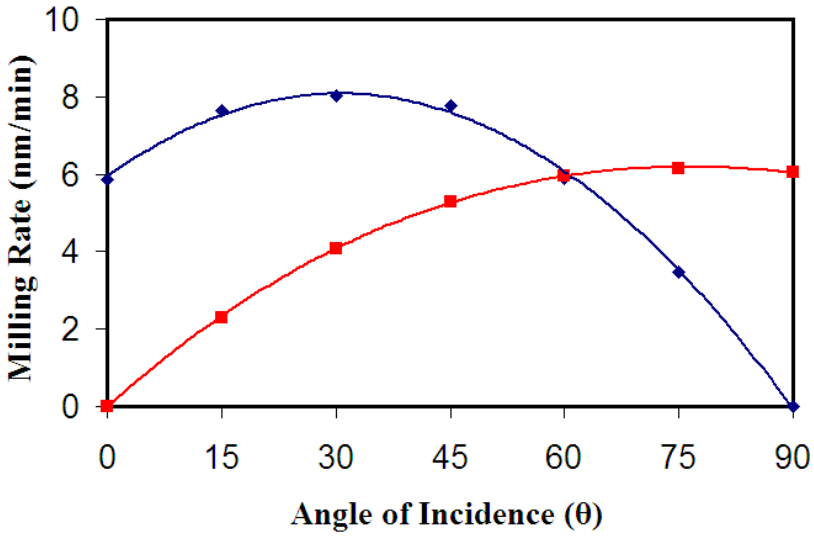

Figure 3.17: The mill rates of the top (diamonds), and side (squares) of a Nb wire being milled at an angle θ, defined in Fig.3.16. The crossover at 61° corresponds to the angle at which the ion beam is expected to produce an equal milling of the top and sides of the wire.

The results of this simple model do not match the results of the experiments, as milling at 60° reduced the height of a wire faster than the width and 75° seemed to produce an even reduction (Table.3.3). From milling done on wires after this calibration it was found that milling 75° in fact reduced the width faster then the height. This suggests that the optimum angle for the even milling lies approximately halfway between 60° and 75°. The discrepancy between the model and the results is likely due to the fact that the

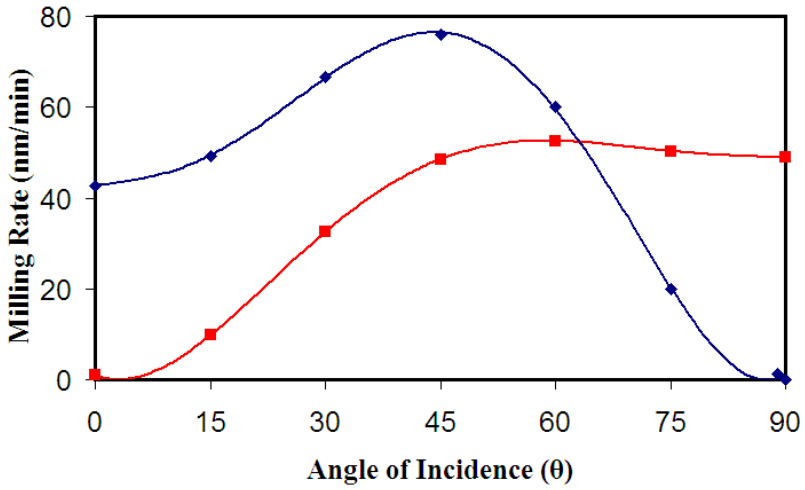

Figure 3.18: The mill rates of the top (diamonds), and side (squares) of an Al wire being milled at an angle θ from the normal to the top of the wire (Original Al data from [36]). The crossover at 63° corresponds to the angle at which the ion beam is expected to produce an equal milling of the top and sides of the wire.

model is too simplistic. To test the reliability of the model I applied it to the work done on Al.

The ideal milling angle for Al was reported to be 60° [11]. The result can be checked using the mill rate vs. angle of Al as shown in Fig.(3.13). To do this I fitted a 6th order polynomial to the angular dependency of mill rate of Al, and then applied the same integral to find the optimum mill angle. The results are shown in Fig.(3.18).

The ideal angle for homogeneous milling of Al, calculated by this model is 63°. This is similar to the 60° angle reported in [11], suggesting that the model is reliable for Al.

The model seems to predict a larger milling angle for Al (63°) than for Nb (61°), whereas the experimental results show Nb requires a larger milling

angle than Al. This discrepancy may be due to the fact the the model does not take into account other effects that occur in the milling process. One process that may have an effect on mill rates is the re-deposition of the substrate on the sides of the wire. It is clear that this will reduce the mill rate of the sides of the wire, for both Nb and Al. However, it is not clear whether it will have a bigger effect on one or the other.

In both cases the substrate used was Si which, at 60° to the normal, has a mill rate of 11.9 nm/min. Comparatively, using the same milling parameters, Al has a mill rate of 13.5 nm/min and Nb has a mill rate of 5.9 nm/min. As Nb has a low milling rate in comparison to Al, one may think that the deposition of Si onto the surface would have a greater effect on Nb. This would cause the mill rate of Nb to be reduced more than that of Al when Si is deposited.

To explore this idea one needs to consider the re-deposition process. As Si is milled from the substrate at 60°, a certain fraction of the material removed is re-deposited onto the wall of the wire. This deposited material is then milled again, but this time at an angle of 30°. This process has two solutions. If the deposition rate of Si onto the walls of the wire is *greater* than the milling rate, the walls will increase in size as more and more of the material is deposited. On the other hand, if the deposition rate of the Si on to the sides of the wire is *less* than the milling rate, an equilibrium state will be reached where are certain percentage of the side of the wire will be covered in Si at one time. The proportion of this coverage will depend on the relative rates of deposition and milling.

In this second case it is not clear that the mill rate of Nb will be affected

more than Al. If the same percentage of the face of each wire is covered in Si, the mill rates of each will be reduced by the same percentage. Therefore, this effect cannot explain the discrepancy between the model for Nb and Al.

It is worth noting however that in Table.(3.3), the Nb wires milled at 60° and 45° both appear to get wider after milling. In comparison, the wire milled at 75°, gets narrower. This suggests that material is being deposited on the sides of the wires quicker than it is being milled for the 60° and 45° mills, while the reverse is true for the 75° mill. This is consistent with the above model. If the Si substrate in the published data had a lower relative milling rate than the Si used in this project, it could account for the discrepancy Without knowledge of this it is difficult to draw further conclusions, apart from the fact that re-deposition appears to be an important effect, and should be taken into consideration when attempting to narrow nanowires.

Another limitation of the model is to assume that the wires are perfectly rectangular in cross section. In reality this is not the case, the wires have a certain amount of curvature between the walls and the top. This curvature will effect the mill rate of the wires as there will be continuum of mill rates over this surface.

In practice most of the wires fabricated with the FIB were wider than than tall before being milled in the argon ion beam miller. In this situation milling at 75° was found to be the best angle as it reduced the width of the wire faster than the height. In this way it was possible to produce sub-100nm wires that became relatively even in cross section after milling.

3.5 Fabricated Samples

3.5.1 Niobium wires

On the basis of the characterisation presented in this chapter, a series of Nb nanowires were fabricated with the FIB in 100nm thick Nb films. These were then narrowed to sub 100nm dimensions using Ar^+ beam milling at the angle 75°. This produced a series of Nb nanowires whose dimensions were reduced from a size of $\sim$ 200nm by 100nm, to $\sim$ 70nm by 70nm. These wires were measured electronically in between milling, and showed a broadening of the transition as a function of wire dimension. The results from these wires are presented in chapter 6.

3.5.2 YBCO wires

The superconducting properties of YBCO wires was found to degrade quickly after being ion beam milled. Because the YBCO wires were no longer covered in a protective layer of gold, and the dimensions small, oxygen loss is likely to have been the cause of this problem. It is well documented that oxygen diffusion increases under a high vacuum [37]. Therefore I concentrated on fabricating the wires directly with the FIB and then measuring them as soon as possible afterwards.

I was able to produce a range of sample sizes from several μm down to 100nm using the FIB. The most compelling results came form a series of different sample sizes that were fabricated from the same 150nm thick film. This allowed the comparison of the transitions of different sample sizes which

had the same film properties, at least eliminating film dependant effects.

A known solution to remedy the oxygen loss in YBCO is to heat the samples above 100° in an oxygen atmosphere. Use of this technique could have replaced the oxygen lost from the wires in a high vacuum. The problem with this solution in these films is that the implanted gallium would also become more mobile at higher temperatures. A possible solution to this might be to mill away the damaged layer with argon milling, and heat in oxygen once the gallium is removed. However, due to time constraints, this technique was not developed.

3.6 Sample Damage

Because the nanowires are so small, they are incredibly fragile, and so a series of methods had to be used to ensure that they would not be damaged. During the course of the project I found that samples were vulnerable to many things including, ultrasonic baths, static electricity, depletion of oxygen (YBCO), and human error.

Many of the samples produced ceased to be conducting in between measurements. One of the main reasons was thought to be damage form static discharge. To overcome this problem a series of measures were put in place including using conductive tweezers, anti-static sample storage, grounding of the wire bonding tip before use, and ensuring that measurement electronics had been grounded before being attached to the sample. I also made sure that I had been grounded before handling samples. The most successful change that helped to avoid the Nb samples from being destroyed was to use

semiconducting silicon substrates. At room temperature these had a resistance of 600Ω, less than the nanowires of 7kΩ, which meant that any static discharge would travel through the substrate instead of the nanowires. The resistance of the substrate rose sharply as the temperature was decreased (Fig. 3.19), to several MΩ, and so, importantly, did not effect the resistance measurements of the sample at low temperatures.

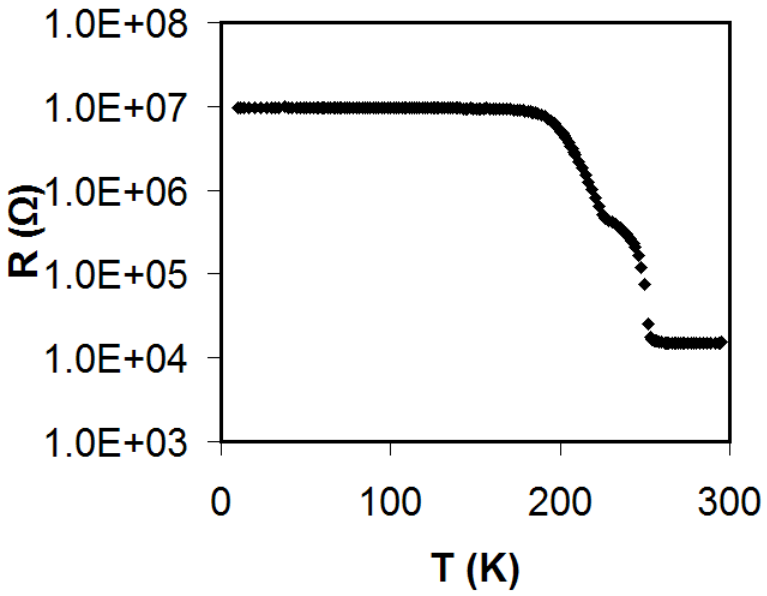

Figure 3.19: A two terminal measurement of the resistance of the Si substrate from independent contact pads showing the resistance of the Si substrate is 14kΩ at room temperature, but rises to several MΩ below 200K (10MΩ is the maximum resistance that could be measured with the equipment.) It should be noted that this measurement of resistance will include the contribution from the Schottky barrier between the Nb and Si layers. Over the length of a nanowire the resistance of the substrate was calculated to be 600Ω.

As well at these effects, the samples were also very fragile to mechanical stress. Nb nanowires were observed to break even after washing with acetone. Therefore care had to be taken not to shock the samples when transporting

them, and avoid getting the samples dirty (vacuum grease), because they could not be subsequently cleaned.

3.7 Conclusions

The aim of the project was to produce nanowires that could be controllably reduced in size. This would allow for several measurements of the R(T) characteristics of the *same sample* as the dimensions were reduced. All of the experiments in this field apart from [11] have compared the data from several different samples. Measuring the same sample at different dimensions has the advantage of eliminating any sample dependent effects from the analysis.

The optimum mill angle for Nb was found to be 75° to reduce the wires with initial width ∼200nm and height 100nm, to wires with width and height ∼70nm. This shows that milling at 75° reduced the width faster than the height of Nb nanowires. Through knowledge of the angular dependency of the mill rate of Nb it would be possible to tune the milling angle used to successfully narrow wires with different initial aspect ratios. A simple model predicted that an angle of 61° would reduce the width and height of a square wire evenly, although re-deposition effects of the substrate may make the required angle larger.

Through the characterisation process presented in this chapter 4 Nb samples were produced that were successfully milled from large dimensions (200nm) to sub 100nm scales and measured several times. The characterisation allowed for the mill angle to be tuned to the dimensions of the original wire to produce wires with an even cross section after milling.

The same characterisation process could be applied other materials. The optimum mill angle is material specific as the angular dependency of the mill rate is different for each. Therefore, applying this characterisation process would allow for the discovery of the optimum mill angle and hence an even reduction in dimensions of any other material.

Many nanowires were also fabricated in YBCO. In this case wires would not survive several milling steps before becoming insulating. So instead I concentrated on fabricating a range of sample sizes on the same film, ensuring that at least the superconducting properties would be largely the same. This was also done successfully.

The results from the electrical measurements of these samples is presented in Chapter 6.

Chapter 4

Phase Slips

This project investigates phenomena exhibited by very narrow (∼100nm) superconducting wires. To understand the physics involved in these experiments, a knowledge of the general properties of superconductors is required. Superconductivity is a large and diverse subject covering many topics that, although very important, are not required to understand the phenomenon of phase slips. Therefore I shall only cover those parts of superconductivity that are useful for this project. These include a description of basic superconductivity (section 2.1), the Josephson effects (section 2.2), and finally the physics of phase slips (section 2.3).

4.1 Basic Superconductivity

Superconductivity is a phenomenon exhibited by certain materials, whereby the resistance of the material drops to zero below a certain temperature. The temperature at which superconductivity occurs is different for each material,

and is called the transition temperature, written T_c. There are two defining properties of superconductors when below T_c, zero resistance and flux expulsion.

Above T_c superconductors exhibit normal metallic conduction, while below T_c the resistance drops sharply to an immeasurably small value (Fig. 4.1). Measurements of persistent currents in a superconducting ring have

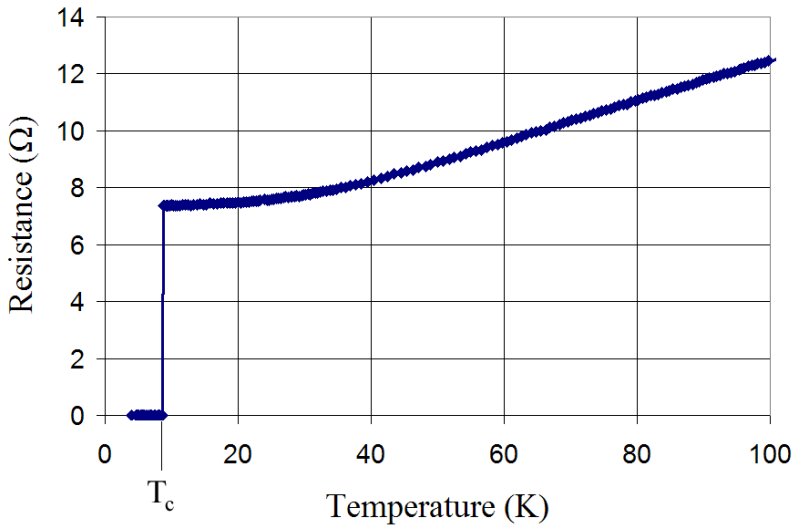

Figure 4.1: An example of the resistance vs. temperature characteristics of a niobium sample, showing a resistive transition at 8.8K

shown that, at the transition, the resistance drops by at least 14 orders of magnitude [38]. It is well established theoretically that the resistance is zero [39].

The second notable property of superconductors is flux expulsion. When a small magnetic field is applied to a superconductor below T_c, the magnetic flux is excluded from the material. In addition, if a superconductor above T_c is cooled in a magnetic field, the flux is expelled from the material as

it undergoes the transition. This happens because the applied magnetic field induces persistent eddy currents in the surface of the superconductor. These eddy currents produce their own magnetic field acting in the opposite direction, which cancels the applied field. This is called the Meissner effect [40]. It is worth noting that zero resistance alone cannot explain this effect. If a magnetic field were applied to a normal, and ideal conductor, which would have zero resistance at zero Kelvin, we would expect flux to be trapped in the material when the magnetic field was taken away. This is not what happens in a superconductor, meaning that the superconducting state is a different thermodynamic phase, which has a lower free energy than the normal state.

Superconductors fall into one of two categories, type I or type II. These different types respond differently to an applied field. In type I superconductors, the Meissner state can be destroyed by a sufficiently large magnetic field, which will cause the superconductor to go back into the normal conduction state. The field that will do this is called the thermodynamic critical field; written H_c. This can be written in terms of the Gibbs free energy;

$$G_N - G_S = \frac{1}{2}\mu_0 {H_c}^2, \tag{4.1}$$

where G_N and G_S are the Gibbs free energy of the normal and superconducting sates respectively. When the applied field is less than H_c the superconducting state has a lower Gibbs free energy, and hence the material will be superconducting. Conversely, when the applied field is above H_c the normal state has a lower energy, so it will exhibit normal conduction.

Type II superconductors have a more complicated interaction with an

applied field, as shown in Figure 4.2. They have two critical fields, the lower critical field H_{c1}, and the upper critical field H_{c2}. At fields below H_{c1} type II superconductors exhibit complete flux expulsion, just like type I. But when the field is increased above H_{c1} magnetic flux penetrates through the superconductor in small strands called flux lines. Each flux line carries a small amount of flux $\Phi_0 = h/2e$, the flux quantum. The flux line density increases with applied field, until the flux lines overlap and superconductivity is destroyed at H_{c2}.

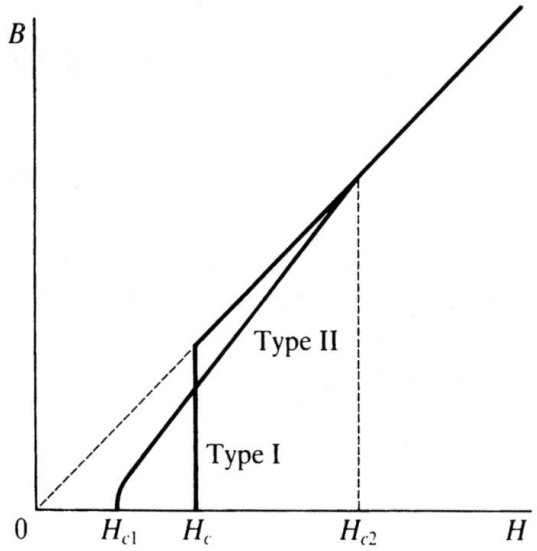

Figure 4.2: Schematic plot [41] of magnetic field B inside a type I and type II superconductor with regard to applied field H. The type I superconductor has a critical field, H_c, where the applied field is large enough to turn the superconductor normal. The type II superconductor has two critical fields, H_{c1} and H_{c2}. Below H_{c1} the superconductor is in the Meissner state, just like type I. Between H_{c1} and H_{c2} it is in the mixed state, with flux penetrating in the form of flux lines. And above H_{c2} superconductivity is completely suppressed.

A current flowing through a superconductor can also destroy supercon-

ductivity if the magnetic field it induces exceeds H_c. This is called the critical current, J_c. T_c, H_c and J_c can be shown in a phase diagram (Fig. 4.3).

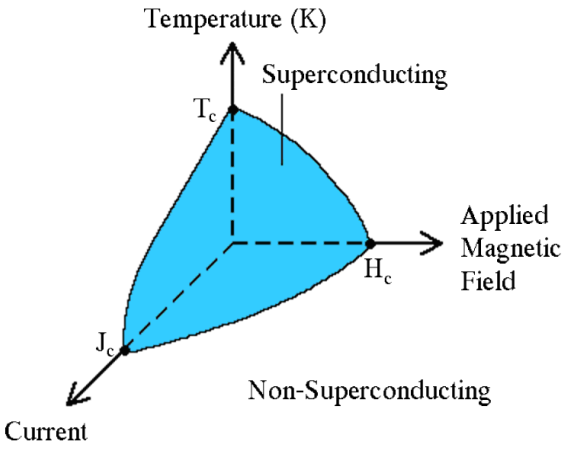

Figure 4.3: Schematic phase diagram showing the superconducting and non-superconducting phases of a material. The characteristic values T_c, H_c, and J_c, are called the critical temperature, the thermodynamic critical field and the critical current respectively. These are the values at which the superconductivity is destroyed when the other variables are zero.

This project has been mainly spent investigating the properties of two superconducting materials, the compound $YBa_2Cu_3O_{7-\delta}$ (YBCO) and the element Niobium (Nb). These both exhibit type II superconductivity, and have transition temperatures of 93K and 9.2K respectively. In addition to this, YBCO is a high temperature superconductor. High temperature superconductors (HTS) were discovered in the 1980's and created a lot of excitement because they were the first materials to have a transition temperature above that of liquid nitrogen, opening up the possibility of many interesting applications.

4.1.1 Theories of Superconductivity

So far I have described the characteristics of superconductivity, with no attempt at explaining the processes that cause it. In this section I shall describe the mechanisms by which superconductivity occurs.

There have been three main theoretical breakthroughs in superconductivity since its discovery. London theory in 1935 [42] and Ginzberg-Landau theory in 1950 [43], provided a phenomenological description of superconductors. Then in 1957 BCS theory provided a complete microscopic description [39]. Details of these theories are available in many texts [44] [45] [46]. Rather than describing each of these theories in detail, I shall just pick out the results that are important for this project.

An important result of BCS theory is that the charge carriers in the superconducting state are not single electrons, but pairs of electrons in a bound state, called Cooper pairs. These pairs are resistant to being broken into single electrons by an energy gap Δ. This means that the Cooper pairs are not affected by collisions with the lattice unless they are given an energy greater than Δ. Below T_c this condition is met and they no longer scatter off the lattice, hence they flow without resistance.

For electrons to form pairs there needs to be an attractive force between them. It was proposed by Frölich in 1950 [47] that an effective interaction could be created between electrons via phonons in the lattice. If one electron emits a phonon and another absorbs it, the energies of the electrons are changed, creating an effective force between them. Importantly, this interaction is attractive, and superconductivity arises when the force of this

attraction overcomes the Coulomb repulsion between electrons. The magnitude of the attractive force is dependant on how strongly the electrons are coupled to the lattice. Therefore superconducting materials tend to have a large normal state resistance. This also explains why the noble metals are not superconductors, their resistance is comparatively low because the electrons are weakly coupled to the lattice.

This idea was further developed by Cooper [48] who showed that this attractive potential meant that the entire Fermi sea was unstable to the formation of pairs, with the most favourable paired state to be that of electrons with opposite spin and momentum. The full many-body theory of BCS [39] solved the dynamics for all electrons, and showed that they all condense into the same quantum state. This is because the Cooper pairs, having integer spin, behave like Bosons, and so are free to occupy the same superconducting quantum state.

The superconducting state can be described by a wavefunction,

$$\psi(\mathbf{r}) = |\psi(\mathbf{r})|\mathrm{e}^{iS(\mathbf{r})}. \tag{4.2}$$

Here, $|\psi(\mathbf{r})|^2$ is equal to the density of superconducting electrons (n_s), and S is the phase of the wavefunction. This wavefunction had already been used by the earlier theories to describe the superconducting state, and is generally called the order parameter, from Ginzberg-Landau theory.

The phase of the order parameter is related to the current in a supercon-

ductor by the London equation,

$$\boldsymbol{J} = \frac{n_s e\hbar}{m}(\nabla S - \frac{2e}{\hbar}\boldsymbol{A}). \tag{4.3}$$

Where $\boldsymbol{J}$ is the supercurrent density, n_s, e, and m are the density of, charge of and mass of an electron and $\boldsymbol{A}$ is the magnetic vector potential. This equation shows that the current flowing through a superconductor increases with the gradient of the phase, a fact that is important when considering phase slips, discussed later in section 2.3.

The London equation can be used to derive an important property of a superconductor, the penetration depth. This is the characteristic length by which a magnetic field can penetrate into a superconductor. A superconductor is a near perfect diamagnet, however, there is a certain depth within which an applied field dies off exponentially. Combining 4.3 with the Maxwell equation curl $\mathbf{B} = \mu_0\mathbf{J}$ to get,

$$\lambda_L = \sqrt{m/(\mu_0 n_s e^2)}. \tag{4.4}$$

Another important characteristic of a superconductor is the coherence length. Both BCS and Ginzberg-Landau theory contain a coherence length that, although related, mean different things. The BCS coherence length $\xi(0)$ is temperature independent, and can be thought of as the size of a cooper pair. The Ginzberg-Landau coherence length ξ_{GL} is temperature dependant and is the minimum distance within which the magnitude of the order parameter can drop to zero (Fig. 4.4).

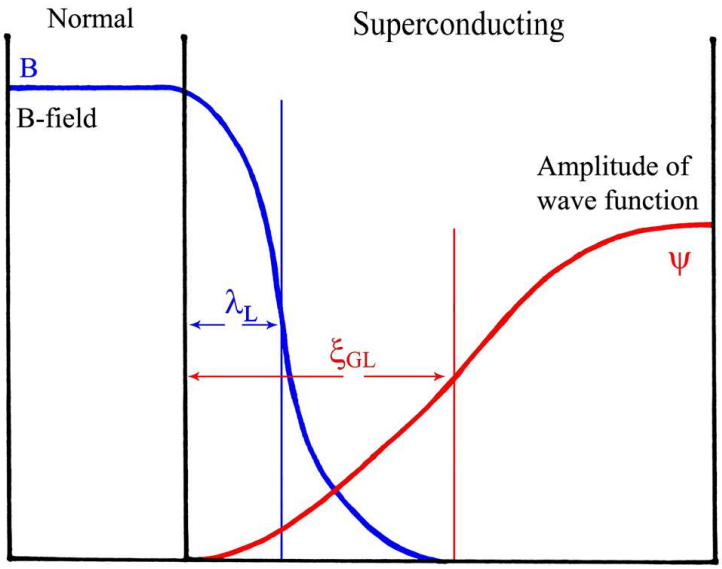

Figure 4.4: Diagram showing the decay of field and order parameter at a normal-superconducting interface. The penetration depth λ_L is the characteristic length scale of the decay of and applied field in a superconductor. The coherence length ξ_{GL} is the characteristic length over which the superconducting order parameter can drop to zero.

The BCS coherence length is given by,

$$\xi(0) = 0.18\frac{\hbar\nu_F}{k_B T_c} \tag{4.5}$$

where ν_F is the Fermi velocity. The GL coherence length is dependant on the BCS coherence length, and also the mean free path of the electrons, l. This is important because it means that the coherence length is dependent on the purity of the material. In the clean limit, where a pure material has a normal state mean free path much greater than $\xi(0)$, the GL coherence

length is given by,

$$\xi_{GL}(T) = 0.74\xi(0)\left(\frac{T_c}{T_c - T}\right)^{\frac{1}{2}}, l \gg \xi(0). \tag{4.6}$$

The opposite condition is called the dirty limit and is where the mean free path is much less than $\xi(0)$, which gives,

$$\xi_{GL}(T) = 0.85\sqrt{\xi(0)l}\left(\frac{T_c}{T_c - T}\right)^{\frac{1}{2}}, l \ll \xi(0). \tag{4.7}$$

The GL coherence length is an important parameter in this project as it determines how narrow a superconducting wire needs to be for the phase slip phenomenon to occur.

This completes a basic treatment of the theory of superconductivity. There has been a huge amount of research done on the various properties I have described, but for the rest of the chapter I will concentrate on one area; the physics of superconducting devices.

4.2 Josephson Effects

Although this project was concerned with fabricating 1-dimensional superconducting wires rather than Josephson devices, it is useful to cover the Josephson effects because the underlying physics has a number of similarities, and the energetics are useful in visualising the phase-slip process.

4.2.1 The Josephson Equations

The Josephson effects we first predicted by Brian Josephson in 1962 [49] when he looked at what would happen when two superconducting regions were separated by a narrow gap. In normal metals, electrons can quantum mechanically tunnel through narrow insulating barriers due to the fact that their wavefunction leaks across the barrier. A similar effect happens in superconductors, but as well as normal electrons tunnelling across the barrier, it is also possible for Cooper pairs to do so. This leads to some interesting effects because when two superconductors are separated by a thin insulating layer the wavefunctions describing each of the superconducting states overlap and can become weakly coupled (Fig. 4.5).

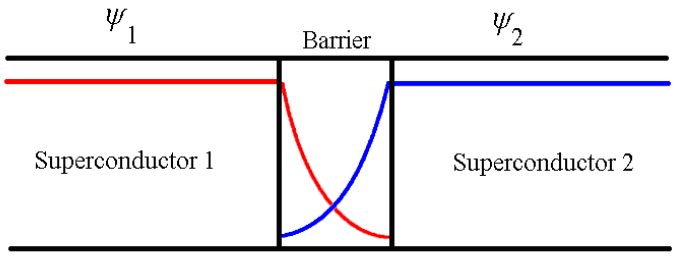

Figure 4.5: Diagram showing the decay of the amplitude of two superconducting wavefunctions in an insulating barrier.

These wavefunctions can be written:

$$\psi_1(\mathbf{r}) = |\psi_1(\mathbf{r})|\mathrm{e}^{iS_1(\mathbf{r})} \tag{4.8}$$

$$\psi_2(\mathbf{r}) = |\psi_2(\mathbf{r})|\mathrm{e}^{iS_2(\mathbf{r})}. \tag{4.9}$$

If the two regions are at the same temperature then one can interpret $|\psi_1|^2 = |\psi_2|^2 = n_s$, and so the amplitudes are the same. However the phase of each wavefunction is independent, and so there will be a phase difference between them $\gamma = S_2 - S_1$. Josephson found that there was a relationship between the phase difference and the current flowing across the barrier, given by,

$$I = I_0 sin\gamma. \tag{4.10}$$

Where,

$$I_0 = \frac{2K \cdot 2eW}{\hbar} n_s = \frac{4\pi KW}{\phi_0} n_s. \tag{4.11}$$

Here K is the coupling strength, W is the volume of the junction and ϕ_0 is the flux quantum. This means that any current up to I_0 can be passed through the junction and no voltage will appear across the junction because the phase difference will adjust to a constant value. This is known as the DC Josephson effect and Eqn.(4.10) is the first Josephson equation.

The second effect Josephson found is that when a voltage is applied to the junction the phase difference increases with time,

$$\frac{d}{dt}\gamma = \frac{2eV}{\hbar} = \frac{2\pi V}{\phi_0}. \tag{4.12}$$

Putting this result into the first Josephson equation (4.10), one sees that an increasing phase difference produces an alternating current. This is called the AC Josephson effect. The current will oscillate at a frequency $\omega = 2eV/\hbar$ and emit radiation which is typically in the MHz to GHz range. This effect produces a very accurate way of measuring the applied voltage and is the

basis of the voltage standard. There is a full derivation of the Josephson equations in the Feynman lectures [50].

In idealised I(V) characteristic of a Josephson junction is shown in figure 4.6.

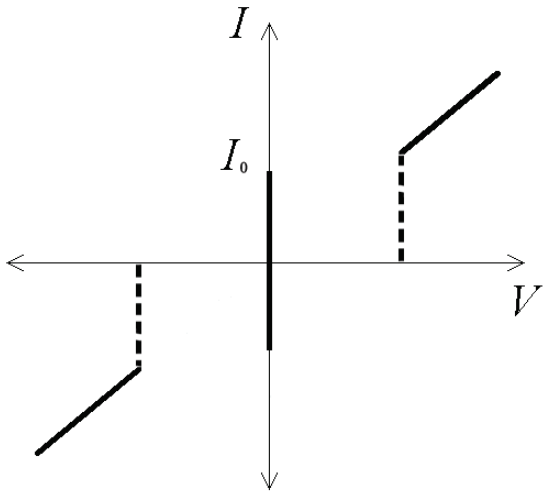

Figure 4.6: Schematic diagram of the I(V) characteristics of a Josephson Junction. This shows that a current up to I_0 can flow across the junction without a voltage drop across the junction.

4.2.2 Dynamics of a Josephson Junction

The dynamics of a real Josephson junction can be electronically modelled by a conventional circuit involving the Junction in parallel with a capacitor and a resistor. This model is called the RCSJ (resistively- and capacitively-shunted junction) model and is useful to make the properties of the Junction easier to understand (Fig.4.7).

The Junction in the RCSJ model is assumed to be ideal and point like,

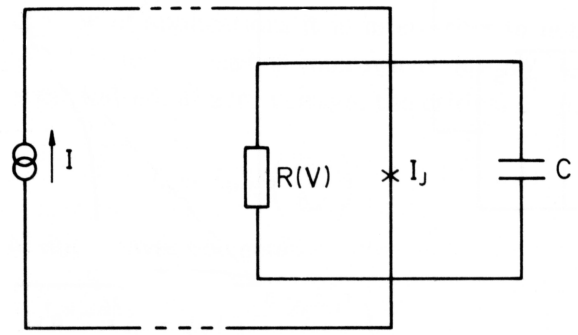

Figure 4.7: Circuit diagram showing the components in the RCSJ model. The cross is an ideal Josephson junction.[51]

and the capacitance and resistance are the self-capacitance and resistance of the real junction. Using Kirchhoff's law on the circuit one gets,

$$I = I_0 sin\gamma + \frac{V}{R} + C\frac{dV}{dt}. \tag{4.13}$$

Re-arranging the second Josephson equation (4.12) one gets,

$$V = \frac{\phi_0}{2\pi}\frac{d\gamma}{dt}. \tag{4.14}$$

Then substituting (4.13) into (4.14) yields,

$$I - I_0 sin\gamma = \frac{\phi_0}{2\pi R}\frac{d\gamma}{dt} + \frac{\phi_0 C}{2\pi}\frac{d^2\gamma}{dt^2}. \tag{4.15}$$

This is the equation of motion of the phase difference, and can be written in terms of a potential,

$$I - I_0 sin\gamma = -\frac{2\pi}{\phi_0}\frac{\partial U_J}{\partial \gamma}. \tag{4.16}$$

Where,

$$U_J = \frac{\phi_0}{2\pi} \{I_0(1 - cos\gamma) - I\gamma\} . \tag{4.17}$$

U_J is called the tilted washboard potential as shown in fig 4.8.

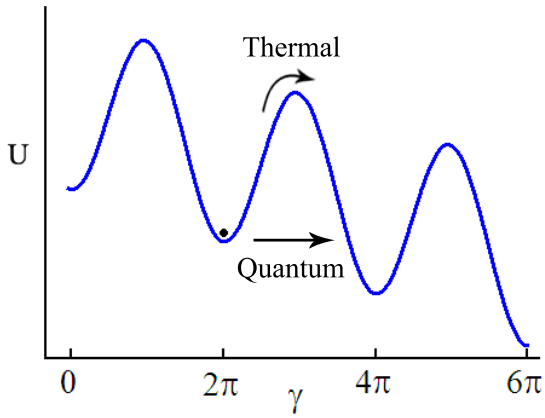

Figure 4.8: A schematic diagram of the tilted washboard potential. The phase difference of the Josephson junction behaves like a classical ball rolling in the potential. It can be thermally excited over the barrier, or quantum tunnel through it.

The tilted washboard potential is a useful model to picture the dynamics of the Junction. Here the phase difference behaves like a classical ball oscillating in the potential. An increase in current causes the potential to become more and more tilted, increasing the probability of the ball rolling down the slope. Figure 4.8 shows the tilted washboard potential for a current $I < I_c$. When the current is larger than I_c the potential is tilted so much that the 'ball' rolls down the potential unhindered, apart from damping. This means that the phase difference evolves with time and the voltage state in figure 4.6 is reached.

When $I < I_c$ the ball oscillates in its local potential well. It can be

excited into the neighbouring potential wells either by thermal excitation over the barriers, or by quantum tunnelling through the barriers. In this case, the phase difference is more likely to move down the potential than up it, although there is a finite probability of both occurring. These changes in the phase difference can be observed, as they will correspond to a voltage across the Junction. These effects have been confirmed by several experiments [52][53][54][55]. These phase dynamics are analogous to the properties of phase slips in superconducting nanowires.

4.3 Phase Slips

In this section I shall describe the process of phase slips in 1D superconductors. I shall describe what they are, the conditions under which they occur, and finally how they can be measured.

4.3.1 Phase Slips

Phase slips occur in superconductors that have been fabricated into very narrow '1D' wires. To be considered one dimensional, the superconductor has to have a width and thickness less than the Ginzberg-Landau coherence length ξ_{GL}. This causes the order parameter to be suppressed in all dimensions apart from along the length of the wire. Under these conditions superconductivity can be suppressed by thermal fluctuations and cause thermally activated phase slips (TAPS). A phase slip is a change of the phase of the order parameter by 2π between the ends of the wire. According to the second Josephson equation (4.12), a rate of change of phase gives a volt-

age. This means that a '1D' wire will have a finite resistance below the T_c of the material. This resistance, being dependent on temperature, quickly dies away as the wire is cooled. This is an interesting phenomenon because it gives a limit to how small superconducting electronics can be fabricated before there is dissipation.

To appreciate in more detail what happens in a thermally activated phase slip it is useful to consider the nature of the order parameter in a 1D wire. Because it is suppressed in all directions apart from along the length of the wire the order parameter can be changed from the general form (4.2), to a 1D form,

$$\psi(x) = |\psi(x)|e^{iS(x)}. \tag{4.18}$$

If this wavefunction is plotted in real and imaginary space it forms a helix as shown in figure(4.9).

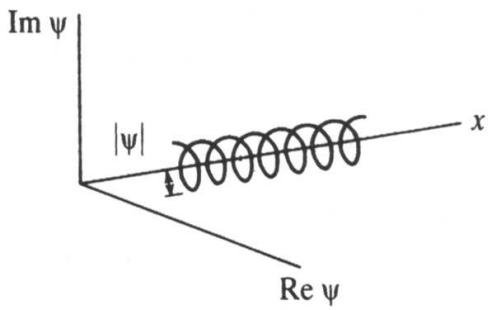

Figure 4.9: Schematic diagram showing the order parameter in a one dimensional superconductor. [56]

In this situation a constant current, proportional to the gradient of the phase, flows along the wire and there is no voltage drop across it. A thermal fluctuation can cause the amplitude of the order parameter to go to zero

at some point effectively creating a small quasi-normal region of length $\sim \xi_{GL}$. In the centre of this region the phase of the order parameter is no longer defined, and so the phase difference across the region can change by an integral number of 2π before coherence is regained. This is a phase slip. Such a phase slip process is schematically drawn in figure(4.10)

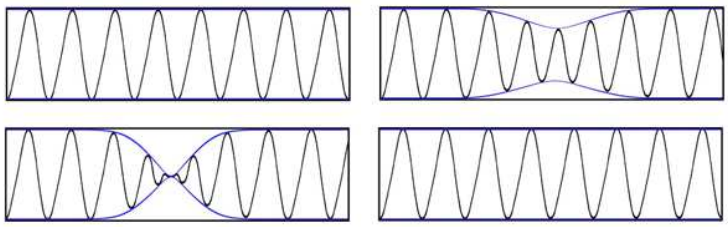

Figure 4.10: Schematic diagram showing the suppression of the order parameter in a phase slip process.

According to the second Josephson relation (4.12), a change in phase causes a non-zero voltage drop to occur across the phase slip region. These discrete voltage drops cause a time averaged voltage across the wire. This causes a resistance to be observed below T_c. Therefore, in similar way to a Josephson junction, the phase dynamics of the 1D wire can be described using a washboard potential. In this case a thermal activation over the barrier corresponds to a thermally activated phase slip. Given the washboard potential model, it is also possible for the phase to quantum mechanically tunnel through the energy barrier. This is called a quantum phase slip.

In a paper by Mooij and Nazarov [3], it was shown that the dynamics of Quantum Phase Slips are the exact dual of Josephson tunnelling with respect to the exchange of phase and charge. In a Josephson junction, quantum tunnelling of cooper pairs leads to a change of charge of $2e$ across the junction.

In a quantum phase slip event it is the *phase* that tunnels, resulting in a change of phase of 2π across the nanowire. Following this logic Mooij showed that any Josephson junction could, in theory, be replaced by a phase slip junction as shown in figure (4.11).

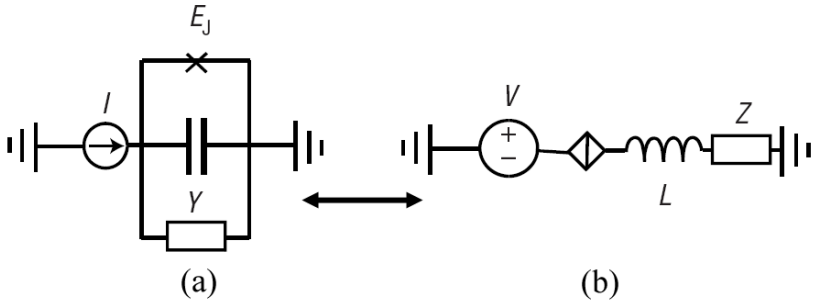

Figure 4.11: The equivalence of Josephson and phase slip junctions from [3]. By exchanging the Josephson junction with a quantum phase slip junction, the current source with a voltage source, the capacitance with an inductance, and putting the components in parallel (b), one obtains the exact equivalent circuit as (a).

From these arguments it can be shown that the equations used to derive the washboard potential for a Josephson junction can be reproduced for a phase slip junction by making the relevant substitutions. For example equation 4.15:

$$I - I_0 sin\gamma = \frac{\phi_0}{2\pi R}\frac{d\gamma}{dt} + \frac{\phi_0 C}{2\pi}\frac{d^2\gamma}{dt^2}, \tag{4.15}$$

becomes,

$$V - V_0 sin(2\pi q) = 2eR\frac{dq}{dt} + 2eL\frac{d^2q}{dt^2}, \tag{4.19}$$

where V is voltage, L is inductance and q is charge. This leads to an exact equivalent washboard potential, where neighbouring energy minima are separated by a charge $2e$, and the slope of the washboard is increased by

increasing the applied voltage.

This equivalence between Josephson junctions and phase slips has interesting technological implications as devices based on Josephson junctions could be reproduced using phase slips junctions. This could produce a phase slip based current standard as an equivalent to the Josephson voltage standard, or could produce a phase slip qubit.

The dynamics of phase slips was investigated long before the relationship to Josephson junctions was established. The theory of thermal and quantum phase slips is shown in the following section.

4.3.2 Thermally Activated Phase Slips

The theory of thermally activated phase slips (TAPS) was first derived in 1967 by Langer and Ambegaokar [1], and then finished by McCumber and Halperin in 1970 [2]. This LAMH theory described the amount of resistance below the transition one would expect to get for a given wire. The full derivation is beyond the scope of this thesis so only the important results are presented here.

As described in the last section, there is an energy barrier between neighbouring states of phase 2π. The height of this barrier is the amount of energy needed to to suppress the order parameter and allow the phase to slip. It is important to note that the LAMH theory calculated the energy landscape of the phase slip process with respect to *phase*, unlike the derivation by Mooij which showed the landscape relative to charge. The result of this is that the potential derived by LAMH is not exactly the same as the washboard poten-

tial, although many of the features are similar; neighbouring energy states separated by phase 2π by an energy barrier, and a tilt between these states that increases with an applied current.

The size of this energy barrier predicted by LAMH theory is,

$$\Delta F_0 = \frac{8\sqrt{2}}{3}\frac{\mu_0 H_c^2}{2} A\xi_{GL} \tag{4.20}$$

where A is the cross sectional area of the wire.

An applied current tilts the potential making phase slips of $+2\pi$ more likely than those of -2π. The difference between the height of the energy barriers in each direction is,

$$\delta F = \Delta F_+ - \Delta F_- = \frac{h}{2e} I. \tag{4.21}$$

Because the energy to get over the barrier is provided by thermal fluctuations, the phase slip probability is proportional to the Boltzmann factor. Hence, the phase slip rate given by LAMH is,

$$\begin{aligned} \frac{d\gamma}{dt} = \Omega \left[exp\left(-\frac{\Delta F_0 - \delta F/2}{k_B T}\right) - exp\left(-\frac{\Delta F_0 + \delta F/2}{k_B T}\right)\right] \\ = 2\Omega e^{-\Delta F_0/k_B T} sinh \frac{\delta F}{2k_B T} \end{aligned} \tag{4.22}$$

where Ω is the frequency at which the phase attempts to go over the barrier. This is given by

$$\Omega = \frac{L}{\xi}\left(\frac{\Delta F_0}{kT}\right)^{1/2} \frac{1}{\tau_{GL}} \tag{4.23}$$

where τ_{GL} is the Ginzberg-Landau relaxation time,

$$\tau_{GL} = \frac{\hbar\pi}{8k_B(T_c - T)}. \tag{4.24}$$

According to the second Josephson relation (4.12), a rate of change of phase gives a voltage. So applying this to Eqn.(4.22), and substituting in Eqn.(4.21) we get,

$$V = \frac{\hbar\Omega}{e} e^{-\Delta F_0/k_B T} sinh \frac{hI}{4ek_B T}. \tag{4.25}$$

From this we can obtain a resistance because at small currents the *sinh* term can be replaced by its argument, giving,

$$R = \frac{V}{I} = \frac{\pi\hbar^2\Omega}{2e^2 k_B T} e^{-\Delta F_0/k_B T}. \tag{4.26}$$

This is the resistance that is measured below the transition temperature. The theory has fitted well with the many experiments that have been performed on 1D superconducting wires [12][13][57][16][8][9]. As experiments went on, another behaviour became evident at low temperatures, where the resistance at low temperatures was larger than that predicted by LAMH theory. This led people to suspect that quantum phase slips could be dominating at these temperatures and led to the theory of QPS.

4.3.3 Quantum Phase Slips

Quantum Phase Slips (QPS) are similar to TAPS, however, rather than the phase changing by 2π due to thermal fluctuations, a QPS corresponds to a quantum fluctuation. This means that the phase tunnels through the potential barrier, rather than getting excited over it. The QPS rate has a much weaker temperature dependence than TAPS, and can lead to a resistance even at 0K. This is in contrast to that of Josephson junctions that have a constant rate of phase change at sufficiently low temperatures. Many papers claim to have observed QPS, however, due to the difficulty of producing wires that are small enough ($\sim 10nm$), and measuring them in a noiseless environment, there has been some controversy over the interpretation of the results.

The first theory for QPS was given by Giordano [17] to fit the data he obtained from narrow indium wires. He proposed a qualitative adjustment to the LAMH theory by replacing k_BT with $\hbar/\tau_{GL}$, where τ_{GL} (Eqn.4.24) varies with temperature and is the cause of the temperature dependence of QPS. The resistance due to QPS is,

$$R = \frac{B\pi\hbar^2\Omega_{MQT}}{2e^2(\hbar/\tau_{GL})} exp\left(-\frac{a\Delta F_0}{(\hbar/\tau_{GL})}\right). \tag{4.27}$$

where a, and B are arbitrary pre-factors close to unity, and Ω_{QPS} is given by,

$$\Omega_{QPS} = \frac{L}{\xi}\left(\frac{\Delta F_0}{(\hbar/\tau_{GL})}\right)^{1/2}\frac{1}{\tau_{GL}}. \tag{4.28}$$

This theory was later supported by Saito and Murayama [58][59], who ob-

tained the same result from a quantitative treatment. However, being based on Ginzberg-Landau theory, there is some controversy over whether this theory for QPS is valid to low temperatures. Strictly Ginzberg-Landau theory is only true close to T_c, although it works well for many systems down to temperatures $\sim T_c/2$.

4.4 Other Mechanisms of Dissipation

As well as phase slips there are other mechanisms that can cause dissipation in superconducting wires. These include flux flow, hot spots and pair breaking. It is necessary to consider these processes when analysing the data from superconductinng nanowires.

4.4.1 Pair Breaking

The superconducting and normal states are separated by an energy gap 2Δ. If a cooper pair at the Fermi energy has a kinetic energy greater than 2Δ, then this energy can break the cooper pair into normal electrons. This occurs at certain critical velocity, v_s, called the pair breaking velocity. There is therefore a critical current at which the cooper pairs can flow, above which dissipation due to pair breaking destroys superconductivity.

In narrow wire this critical current has been derived from Ginzberg-Landau theory to be [60],

$$J_c = \frac{4}{3\sqrt{6}} \frac{\mu_0 H_c(T)}{\lambda(T)}. \tag{4.29}$$

Which shows how the critical current changes with temperature,

$$I_c \propto \left(1 - \frac{T}{T_c}\right)^{\frac{3}{2}}. \tag{4.30}$$

By measuring the variation of I_c with temperature, and fitting to this function one can ascertain if the breakdown of superconductivity is caused by pair breaking.

4.4.2 Flux Flow

As already mentioned, magnetic fields permeate type II superconductors in small strands of magnetic flux, called flux lines, each containing a single flux quantum ϕ_0. When an electric field is applied to a type II superconductor, the flux lines feel a Lorenz force at right angles to the flow of supercurrent. The flux lines tend to pin to sites with low energy, for example, crystalline defects or chemical impurities. However, if the Lorenz force is large enough the flux lines can move, causing dissipation. This is known as flux flow.

The V(I) relationship of flux flow is given by the relation [61],

$$V = R_F(I - I_c), \tag{4.31}$$

where R_F is the flux flow resistance and I_c is the critical current above which the flux lines become depinned and and start to flow.

The flow of flux lines can also be thermally activated [62] out of the pinning sites. The effect of this is to reduce the critical current I_c, needed to liberate the flux lines, as the current and heat energy both contribute to the

depinning. Experimentally this can be observed as a decrease of I_c as the temperature increases close to T_c.

4.4.3 Hot Spots

Superconductivity breaks down when the applied current exceeds the critical current I_0 of the superconductor. In nanowires the critical current may not be homogeneous along the sample as impurities in the material, and variations of the cross section can cause the material to have local variations of I_0. The effect of this is that, when the current applied is increased, the region of the wire with the lowest I_0 will turn normal first, and start to dissipate heat (hot spot) [63]. This dissipation of heat can quickly increase the temperature of the surrounding wire above T_c, until superconductivity is completely destroyed in the wire.

This effect is experimentally manifested in hysteresis of the V(I) curves of the wires. As the applied current is increased the wire jumps into the voltage state at a certain I_0. When the applied current is then reduced, the wire will turn superconducting again, but at a current lower than I_0. This is because the wire will still be dissipating heat, and so the temperature will only reduce below T_c after a certain relaxation time. This effect can be seen at all temperatures, however I_0 reduces as the temperature is increased towards T_c.

The temperature dependency of the critical current I_0 close to T_c is dif-

ferent to that of the pair breaking case, and is given in [63] to be,

$$I_0 \propto \left[1 - \left(\frac{T}{T_c}\right)^2\right]^{\frac{3}{2}} \left[1 + \left(\frac{T}{T_c}\right)^2\right]^{\frac{1}{2}}. \tag{4.32}$$

This concludes the theoretical look at the physics in this project. The following chapter details the experimental set-up for cooling the nanowires to low temperatures, and measuring their electrical properties. Then finally, chapter 6 presents an analysis of the results in terms of the theory presented in this chapter.

Chapter 5

Low Temperature Measurements

5.1 Measuring Equipment

To obtain the R(T) characteristics of the nanowires they were cooled in a continuous flow cryostat, and measured electronically as they cooled. Custom built electronics was used to measure the V(I) characteristics of the wires, which were then fitted to produce the resistance vs. temperature graph. Analysis of the R(T) and V(I) plots reveals whether phase slips occur in these samples. The base temperature of the cryostat was $\sim$ 4K.

Another system was built to measure the nanowires at lower temperatures, and in a lower noise environment. This was based on an Oxford Instruments Heliox system and had a base temperature of 0.3K.

The two cooling systems had specific roles in the measurement of samples. The continuous flow system had a fast turnaround time and enabled the

measurement of many samples at a time. The Heliox system took a lot longer to run but had many advantages over the continuous flow system including a lower base temperature, better shielding and filtering, and much better temperature control. Because so many samples were produced, the idea was to measure them in the continuous flow system first, and those that showed interesting characteristics would be measured in the Heliox system. Unfortunately, due to sample damage, none of the sample measured in the Heliox system exhibited phase slip like behaviour.

5.2 Continuous Flow Cryostat

A standard continuous flow system was used to cool samples down to $\sim$ 4K. The temperature was measured using a silicon diode thermometer at the base of the cryostat. The sample was mounted on a multi-pin sample holder at the bottom of the cryostat probe. Electrical connection to the sample was made by aluminium wire bonds between contact pads on the sample and gold tracks on the sample holder (Fig.5.1). The sample holder and measuring electronics were designed to allow for up to 4 samples to be connected at a time. This meant that many samples could be measured without the need to remove the probe.

In normal operation the samples were cooled to a base temperature of 4.2K. Lower temperatures of $\sim$ 3.4K could be obtained by filling the lower portion of the cryostat with helium liquid, and then pumping on this. The sample was shielded from magnetic field by surrounding the cryostat in a mu-metal shield with a shielding factor of $\sim$20. Measurements were made

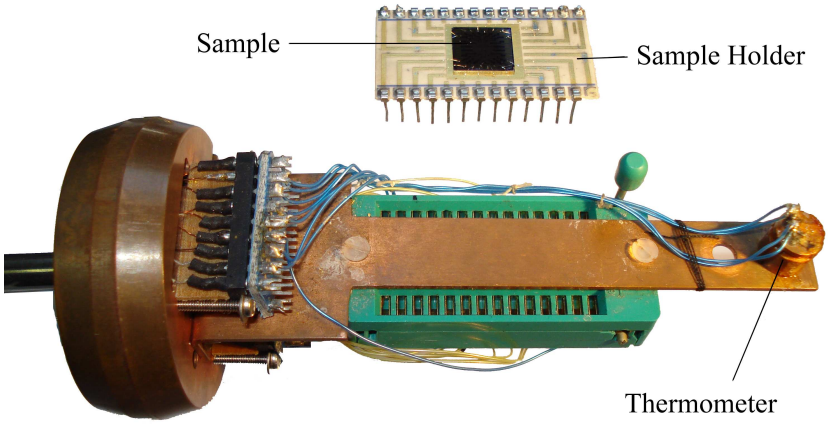

Figure 5.1: The sample is glued to the sample holder with varnish, and electrical connection made with aluminium wire bonds attached to the gold tracks. The holder is then clamped in place onto the cryostat probe. There are enough connections to allow for four samples to be measured in four terminal mode. Another thermometer was added to the sample holder at a later date (Fig.5.3.)

with and without the the mu-metal shield but no difference was observed in the R(T) characteristics.

A limitation of this system when taking sensitive measurements was the lack of electronic filtering of the wires leading to the sample. This means that electromagnetic interference with the wires above the sample could have effected the measurements that were taken as the samples are susceptible to frequencies in the GHz range.

Ideally one wants to take electrical measurements at a stable temperature, but unfortunately the temperature control on this system was poor. Fortunately the warming of the probe from base temperature was slow with respect to the time taken to make a measurement. The warming was $\sim$0.01K/s, and the time taken to make an V(I) plot was 1 second. Therefore the V(I) plots

were unaffected by the temperature change. This was confirmed by the V(I) plots being linear, showing that the resistance of the sample was not changing over the time taken to make a measurement.

An issue discovered with this system was a temperature lag between the thermometer and the sample at the lowest temperatures. This was first noticed when the R(T) characteristics of the nanowires showed a hysteresis between measurements taken when the sample was cooled and those taken when it was warmed up (Fig.5.2).

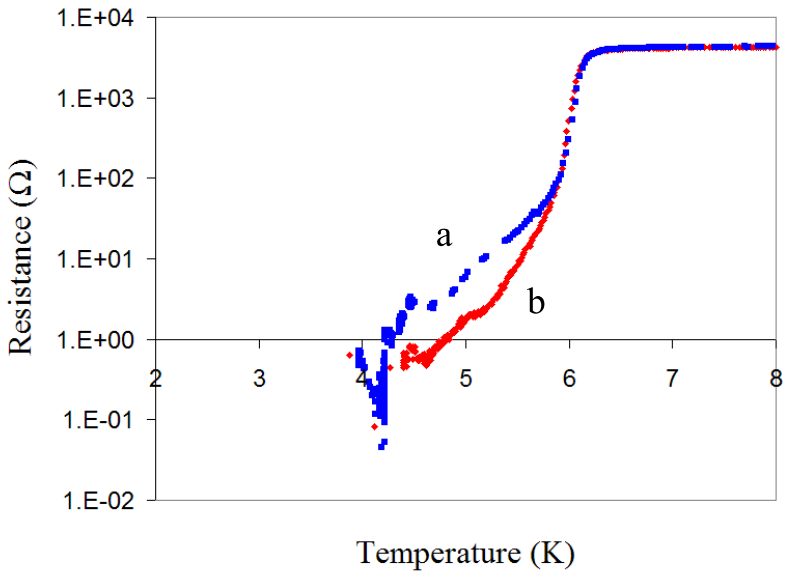

Figure 5.2: Plot (a) shows the R(T) characteristics of a sample being cooled. Plot (b) shows the R(T) characteristics of the same sample as it warms up. The hysteresis between the two plots is attributed to a thermal lag between the thermometer and sample.

This hysteresis was only observed at temperatures below 6K. Above this temperature both the sample and thermometer were cooled by the helium exchange gas that was cycled through the cryostat can, and so were in rela-

tively good thermal equilibrium. However, at the lowest temperatures liquid helium would start to condense in the bottom of the cryostat. When this reached the copper plate at the bottom of the probe it cooled the thermometer faster than the sample. This was because the thermometer was directly attached to the copper plate whereas the sample was separated from it by the ceramic plate of the sample holder (Fig.5.1).

To remedy this problem a new silicon diode thermometer was placed directly onto the sample holder, next to the sample (Fig.5.3). Prior to the attachment to the sample holder this new thermometer was calibrated by attaching it to the same cooper bar as the pre-existing thermometer, at the same height above the bottom of the probe. This eliminated the effect of any thermal gradient along the length of the bar. The voltage across the new thermometer was measured at a series of temperatures to produce a graph of voltage vs. temperature. This was then fitted with a Chebychev polynomial to produce a function that would give an accurate temperature for a given voltage.

The placement of the new thermometer on the same piece of gold as the sample ensured that they were in thermal equilibrium. When using the new thermometer the low temperature hysteresis was no longer observed (Fig.5.4), thereby giving confidence that the temperature measurements were reliable.

Because many data sets had already been taken with the old thermometer, it was useful to compare the R(T) characteristics of the same sample using the two thermometers. The comparison is shown in figure (5.5).

Figure (5.5) shows that the temperature lag between the thermometer on the cryostat probe and the sample is $\sim$ 0.5K at the low temperatures, and

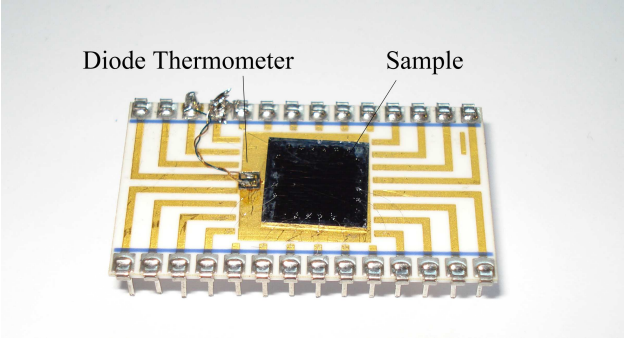

Figure 5.3: The sample holder with an attached silicon diode thermometer. Two of the wires leading to the sample were used to measure the voltage across the thermometer.

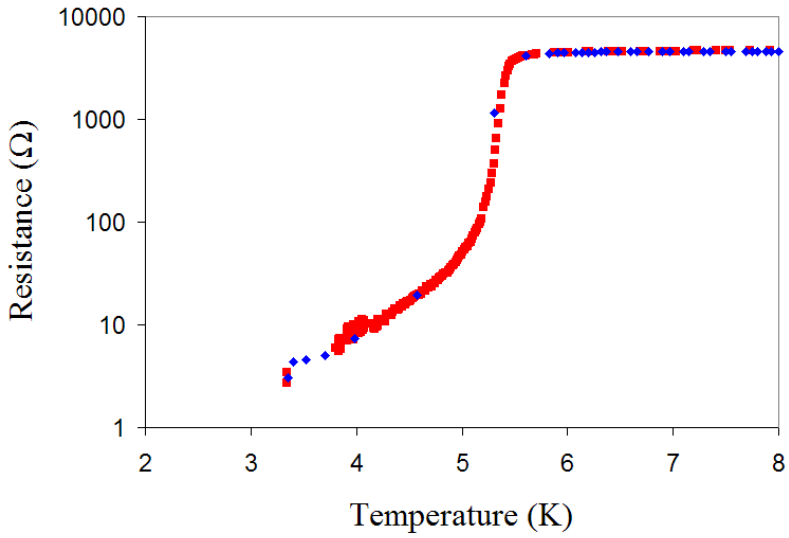

Figure 5.4: The blue data points show the R(T) characteristics of a sample being cooled. The red data points show the R(T) characteristics of the same sample as it warms up. The sample was cooled very quickly to enhance any effect caused by a temperature lag between the sample and thermometer. Even under these conditions there is no significant hysteresis.

reduces at higher temperatures. This calibration was used in the analysis of the R(T) data to correct three R(T) characteristics that were effected by the temperature lag. These samples had been milled after the data taken and so

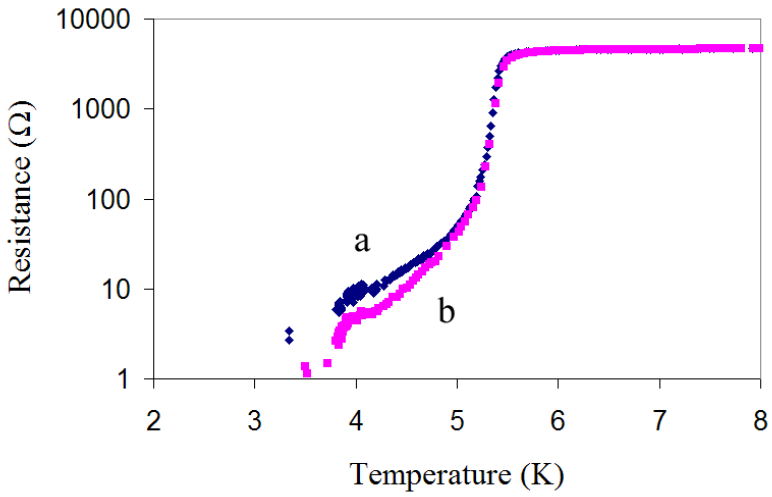

Figure 5.5: R(T) characteristics of the same sample measured with the on chip thermometer (a) and the thermometer at the bottom of the cryostat (b).

could not be re-measured with the new thermometer.

5.3 Measuring Electronics

The electrical measurements of the sample were controlled using a PC via a custom electronics box. The software and electronics were designed and built by Dr.M.S.Colclough. This system allowed for control over the measurements that were made.

The custom electronics, so called 'VI Box' controlled the current passed through the sample and allowed for the measurement of the voltage. A multiplexer at the top of the box allowed the user to choose which of the wires leading down to the sample would carry the current and which would measure the voltage. In this way it was possible to measure several samples

without the need to remove the cryostat probe. The box also measured the temperature of the thermometer by passing a 10μA current and measuring the corresponding voltage across the silicon diode. This voltage was then converted to a temperature by the computer.

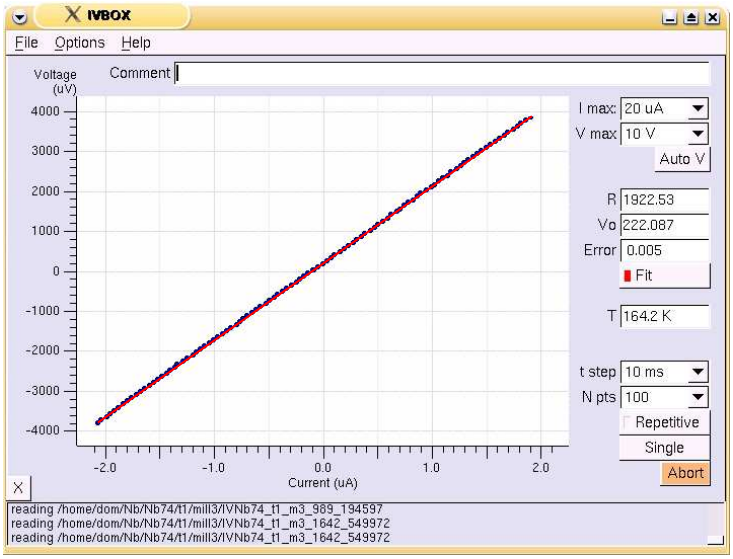

Figure 5.6: The program controlling the IV box control electronics.

Figure (5.6) shows the computer program that controls the VI Box. The measurement consists of several small steps in current plotted with the corresponding voltage measurement. This has then been fitted with a straight line and the resistance calculated. The program also saves the temperature of the thermometer at the time of the measurement.

There are several measurement settings that can be changed including the size of the maximum current measured, the number of data points and the speed at which the data points are taken. Most of the V(I) characteristics in this project were taken with 100 points per graph, and 10ms between each point which was found to be a good compromise between measurement time

and accuracy of measurement. The applied current was varied in the range 1μA - 10μA depending on the sample that was being measured. Larger currents were avoided due to the fragile nature of the wires where high currents could lead to overheating.

To ensure that the IV Box was reliable, a series of tests were made. A number of dummy resistors were measured that simulated the resistance range of my samples. These measurements were compared to those made by a multimeter and found to correspond well. The electronics could measure resistances down to $\sim 0.1\Omega$. The highest resistance the box could measure was around $\sim$10MΩ, well above the maximum that was required for the samples in this project.

To produce the R(T) characteristics, another program takes the resistance and temperature measurements from the V(I) program. An entire R(T) plot is then built up over time (Fig.5.7). When a full R(T) graph was completed it was saved to a folder along with the V(I) characteristics of every single data point. The data were then transferred to another computer for analysis.

5.4 Heliox System

Measurements were also made using an Oxford Instruments Heliox system. Although none of the samples measured in the Heliox system exhibited phase slip behaviour, the design of the system has been included for completeness.

The Heliox system consisted of a cryostat that was submerged in liquid helium in a dewar. Further cooling below 4.2K was achieved by continuous flow of ^{4}He, which reduced the temperature to 1.5K. The final stage of cooling

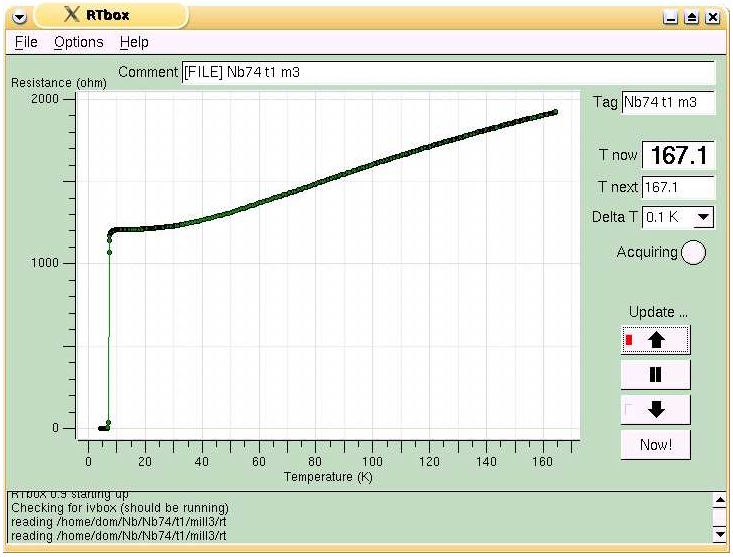

Figure 5.7: The program recording the R(T) characteristics of a sample.

was performed by a ^{3}He pot, within which ^{3}He liquid would be condensed and then pumped on by cooling a carbon sorb. The system had a base temperature of ~ 0.3K.

A custom low noise environment was built to house the samples in this system. This included a sealed copper box to house the sample, electronic filtering of the wires leading to the sample, and a superconducting lead shield surrounding the base of the cryostat. This is an important inclusion to measuring the phase slip process as interference has the potential to cause a flattening in the R(T) characteristics at low temperatures. This could cause interference to be mistakenly interpreted as quantum phase slips, one criticism of some of the previous work done in this area.

The design of the sample box is shown in figure (5.8). It was machined from a single piece of copper and had a lid that screwed down in several places. This was important to make sure that the sample was shielded form

any external electromagnetic radiation.

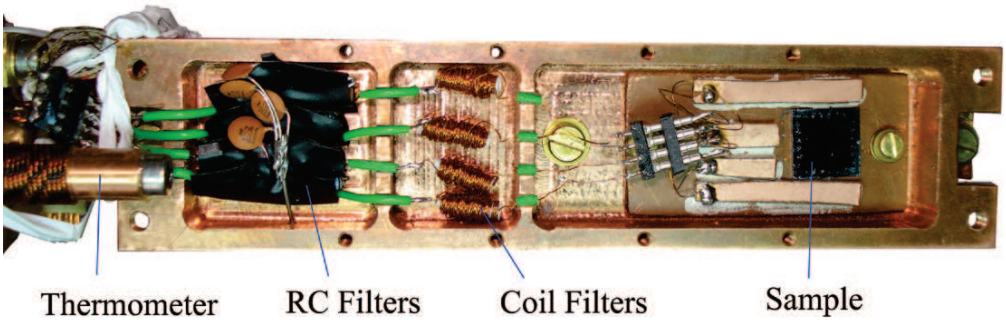

Figure 5.8: The copper box designed and built for the phase slip experiments.

During the design of the box, an estimate of the thermal load on the system was made, as there was a limited amount of ^3He (0.22 mol) available for cooling. The total volume of the box was calculated to be $\sim 5.4\times10^{-5}m^2$, which is 7mol of copper. The temperature dependent heat capacity of copper is given by [64],

$$C_p = 8 \times 10^{-4}(T + 7 \times 10^{-}2T^3). \tag{5.1}$$

This gives $C_p(1.5K) = 2.8\times10^{-3}\ Jmol^{-1}K^{-1}$, and $C_p(0.3K) = 2.4\times10^{-4}$ $Jmol^{-1}K^{-1}$. To find the total heat capacity of the copper, the function (5.1) was integrated over the temperature range of 0.3K-1.5K, giving a total heat capacity of $9.3\times10^{-4}\ Jmol^{-1}$. For 7 mol of copper this is a total stored heat energy of $6.5\times^{-3}\ J$. ^3He has a latent heat of vaporisation of 0.026 kJ/mol, which means that the 0.22 mol in the ^3He pot would need 5.8J of heat energy to vaporise completely. 5.8J is much more than the heat load of the sample box of $7 \times 10^{-3}J$, and so the design of the box does not greatly effect the

hold time at the lowest temperatures.

Two stages of filtering were employed within the walls of the sample box. This included a resistance/capacitor (RC) low pass filter and an inductive filter on each lead going to the sample. This was to filter out frequencies that could interfere with the results. The minimum time between measurements used by the measurement electronics was 1ms, corresponding to an operating frequency of 1kHz. Therefore the filtering was designed to filter out frequencies above 1kHz so as not to effect the measurements. The frequency response of an RC filter is given by $f = 1/2\pi RC$. There were limitations as to the size of resistance that could be used, as large resistances would put extra load on the current source, and the capacitors needed to be small enough to fit inside the box. Therefore 500Ω resistors and 1nC capacitors were used, giving the 3dB point at 300kHz. The measured frequency response of one of the filters is shown in figure (5.9).

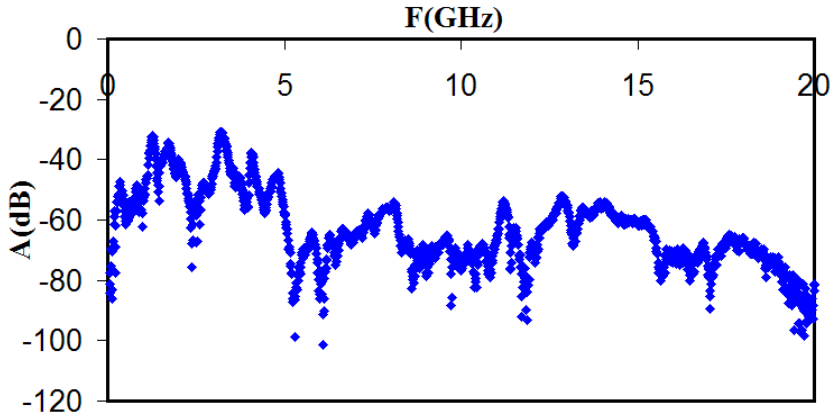

Figure 5.9: The attenuation of the filtering as a function of frequency as measured on a network analyser. The attenuation of -80dB had reached the noise floor of the analyser, and so the filtering of these high frequencies is good.

From the top of the cryostat the voltage and current leads were transported via twisted-pair co-axial cables to the VI box where the signals were amplified. The same VI box and computer software used in the continuous flow cryostat was used to take the V(I) measurements in this system. However, the thermometry supplied was not compatible with the V(I) electronics and so the R(T) characteristics were recorded manually. This was possible as measurements were taken at stable temperatures.

The temperature was measured with a ruthenium oxide resistor thermometer situated on the ^{3}He pot and the thermometer leads were well heat sunk to the ^{3}He pot. The Heliox system provided much better temperature control than the continuous flow system with stability within 1mK over the range 0.3K to 10K.

The sample can containing the sample box and thermometer was pumped to 1×10^{-5}mbar and then a small amount of exchange gas introduced. This meant that there was a much weaker thermal contact between the sample and thermometer through the exchange gas than in the continuous flow system. The thermometer and sample were both connected to the ^{3}He pot, but as a large amount of copper separated the sample from the thermometer one had to take thermal relaxation times into account. To ensure the sample and thermometer were in thermal equilibrium several seconds was left between the temperature becoming stable and the resistance measurement being made. The temperature stability could be observed directly from the resistance becoming stable, but can also be estimated with the following calculation:

Copper has a thermal conductivity at 1K of $k = 1 \times 10^2\ WK^{-1}m^{-1}$ [65]. The copper bar connecting the sample box to the ^3He pot has an

approximate length of 0.04m and cross-sectional area $1 \times 10^2\ m^2$, giving a specific thermal conductivity of $K = kA/L \approx 0.25\ 4WK^{-1}$. At 1K the sample box has a specific heat capacity of $3.910^{-4}\ JK^{-1}$, which gives a relaxation time $\tau \approx C/K = 1.6 \times 10^{-3}\ s$, a fraction of a second. This gives confidence that the sample and thermometer were in thermal equilibrium because several seconds were left before taking a measurement.

Chapter 6

Data Analysis

Of the many samples that were fabricated, only a few were made narrow enough to exhibit a broadening of the transition. Those that did, showed characteristics reminiscent of thermally activated and quantum phase slips. To find whether the broadening of the transition was due to phase slips the data were analysed using the theory of phase slips presented in Chapter 4.3. The following chapter shows the analysis of the data from nanowires fabricated from niobium and from YBCO.

An example of a typical niobium and YBCO wire is shown in figure (6.1). Neither wires are perfect 4 terminal, which means the voltage leads measured the resistance of the regions either side of the wire as well as the wires themselves. In Nb and YBCO this is not a problem as the T_c of both materials goes down with sample size. This means that the regions either side of the wire turned superconducting before the wires, and so did not effect the measurement of the wire resistance. The resistance drop of the regions either side of the wire were estimated to be $\sim 1\Omega$ for Nb and $\sim 15\Omega$ for YBCO,

and so are difficult to resolve as the normal state resistance of most of the wires are in the region of $1k\Omega$. For these reasons one can be confident that the contacts did not interfere with the measurement of the wire resistance.

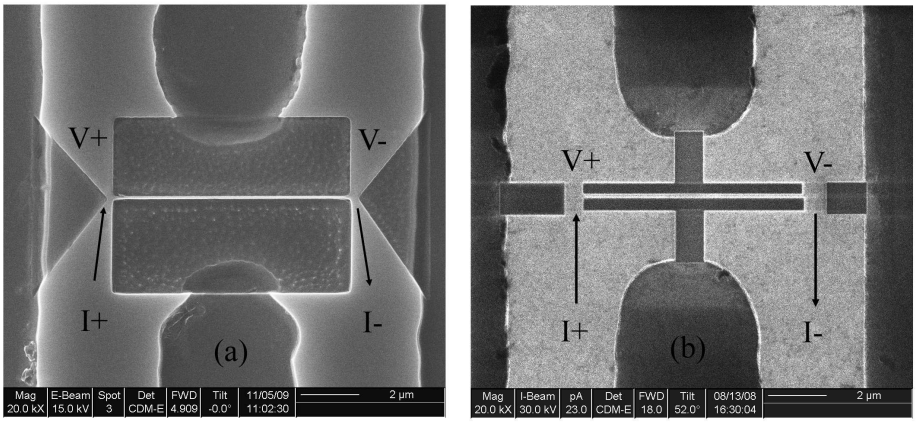

Figure 6.1: The design of the wires fabricated in Nb (a) and YBCO (b).

As explained in Chapter 5, the data were obtained by measuring V(I) characteristics of the wires at a range of temperatures, and then deriving the resistance from these V(I) plots. A typical R(T) plot showing a broadened transition is shown in figure(6.2).

A correction of some of the R(T) characteristics was made because some of the V(I) plots were not linear over the current range measured. This led to the R(T) computer program incorrectly fitting a straight line to the data (Fig. 6.3 (a)). This was an obvious problem with the automatic fitting of the program, as it could only fit the data with a straight line, and would attempt to do this regardless of the shape of the characteristic. At most temperatures this was not a problem as the V(I) characteristics were linear over the whole range.

The V(I) characteristics that were not linear were dealt with separately

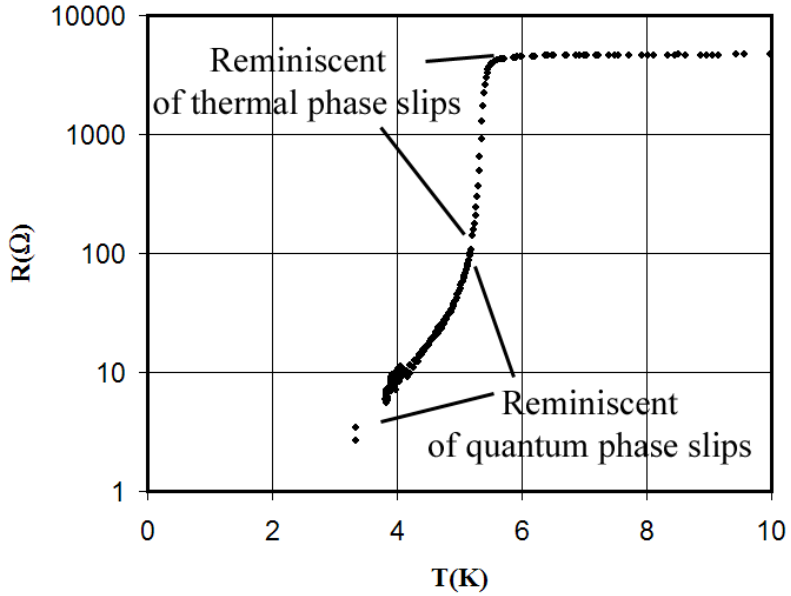

Figure 6.2: An example of a broadened transition. Instead of the resistance dropping sharply to 0Ω at 9.25K as in bulk niobium, the track resistance reduces more gradually. Two behaviours were observed in several wires, the broadened transition reminiscent of thermal phase slips and a lower resistive tail reminiscent of quantum phase slips.

by recalculating the resistance using the linear portion of the V(I) plot (Fig. 6.3 (b)). Note that the current offset is a function of how the electronics applies the current. Because the current source was not perfect, the applied current did not correspond exactly with the actual current flowing through the sample. The electronics measured the actual current applied and plotted this.

A corrected and uncorrected R(T) characteristic is shown in figure (6.4). Wherever possible the corrected characteristics have been shown. However, as the resolution of the measurement electronics were limited to ∼10nA, it was difficult to resolve the linear portion of the V(I) plot very close to T_c in

some specimens. Therefore, the corrected R(T) characteristic is likely to be more rounded at the onset of the transition. An analysis of the behaviour of these V(I) characteristics is presented later in the chapter.

Some of the V(I) characteristics in two of the YBCO wires also showed an anomalous behaviour, however it was not possible to correct for these as they did not have a linear portion. This is dealt with in the YBCO analysis section. Apart from this, it is worth noting that all other V(I) characteristics were linear over the current range ($\pm 1\mu$A) used. One can be confident in the reliably of the measured resistance form the V(I) characteristics as the measurement electronics was tested extensively, and showed reliable measurements of the resistance of wires down to 0.1Ω.

6.1 Method of Analysis

A computer program was written to aid the fitting of the data. The program plots the theoretical prediction of the resistance caused by both thermal and quantum phase slips based on the values of the variables involved. It also has the functionality to plot the R(T) characteristics from the experiments, so that the user can fit the data with the theory. Two versions of the program were written which each had alternative fitting parameters. This was done because the energy barrier ΔF_0, which occurs in both the thermal and quantum phase slip theory, can be written in two ways.

In chapter 4, ΔF_0 was shown to be:

$$\Delta F_0 = \frac{8\sqrt{2}}{3}\frac{\mu_0 H_c^2}{2} A\xi_{GL} \tag{6.1}$$

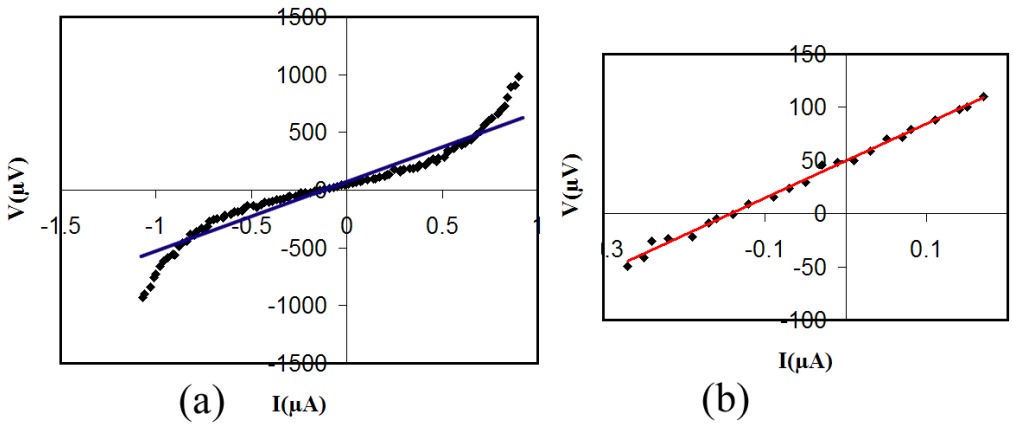

Figure 6.3: Plot (a) shows an example of a non-linear V(I) characteristic and illustration of the error caused on the measurement of R. (b) shows the linear portion of the same V(I) characteristic. Here the current offset is a function of how the electronics applies the current.

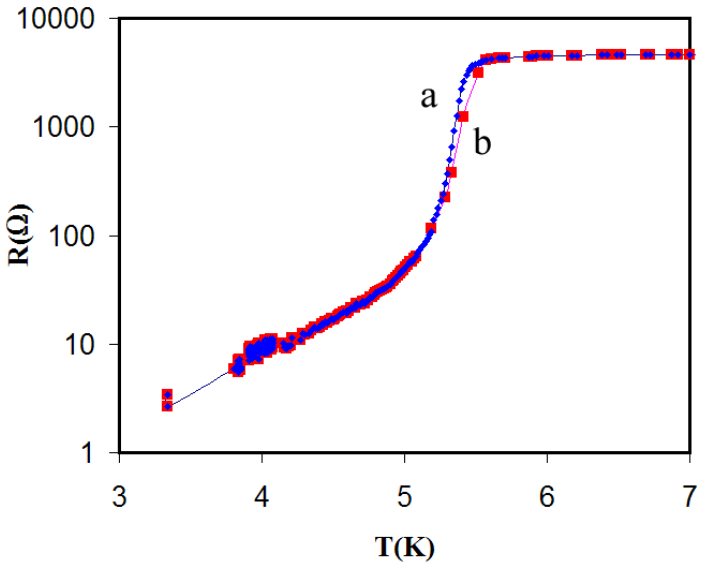

Figure 6.4: The uncorrected (a) and corrected (b) R(T) plot of a wire. The correction was made due to non-linear V(I) characteristics.

Following [9], ΔF_0 can also be expressed,

$$\Delta F_0 = 0.83 \frac{L}{\xi(0)} \frac{R_q}{R_N} \cdot k_b \cdot T_c \left(1 - \frac{T}{T_c}\right)^{\frac{3}{2}}. \tag{6.2}$$

Here $\xi(0)$ is the coherence length of the wire, R_N is the normal resistance of the wire before the transition, and R_q is the quantum of resistance of cooper pairs given by $h/4e^2 = 6.45k\Omega$.

The first form of ΔF_0 (6.1) comes from the LAMH theory that describes the thermal phase slip dynamics. The factor $\mu_0 H_c^2$ is the condensation energy of the superconducting state per unit volume, and the product of the coherence length ξ_{GL} and the cross sectional area A gives a volume. This is the volume over which the order parameter of the superconducting state ψ must be suppressed so that the phase can slip.

The advantage of expressing ΔF_0 in Eqn.(6.2) is that it reduces the parameters of the theory to just the length L, the normal resistance R_N, the transition temperature T_c, and the coherence length ξ_0. This eliminates H_c and the cross sectional area of the wire A as parameters. It is this form of ΔF_0 that has been used in much of the published work on phase slips as the parameters are more experimentally accessible.

The user interface of the two programs are shown in figure (6.5). The programs contained a number of functions to allow for easy use. The central plotting region can be resized to fit the data, and can plot data up to 100K. It can read in experimental data from a text file, and write the theoretical fitting data to a text file for plotting in other programs. The resistance axis can be displayed on a linear or log scale, and the data adjusted accordingly.

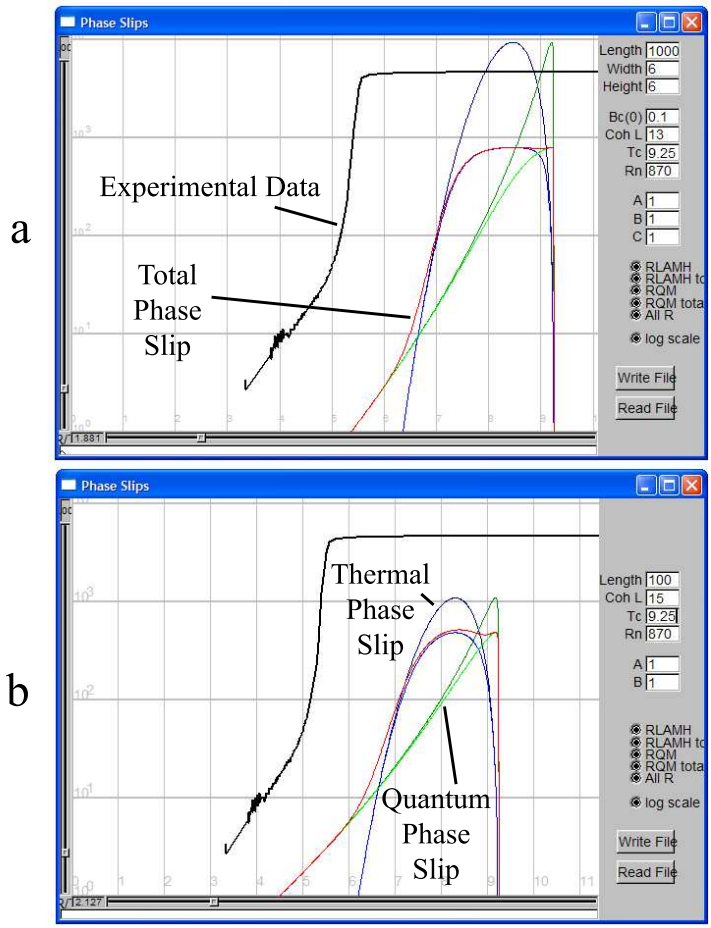

Figure 6.5: The programs used in the project. The experimental data can be fitted with the theoretical predictions by altering the parameters. The total phase slip rate (red line) is made up of a contribution of thermally activated phase slips (blue line) and quantum phase slips (green line). The program (b) was used to fit the experimental data as there were less free parameters.

The theoretical fit is automatically re-drawn whenever any of the parameters are changed or the window re-sized. The program is robust in use.

Extensive testing was done on the program to ensure that it produced the correct results. This included tests of each of the functions of the program, to ensure that the calculations were correct. The program was also tested

against the model used to analyse the data in Ref.[25], as well as published data to confirm that it produced the same results given the same input parameters (Fig.6.6).

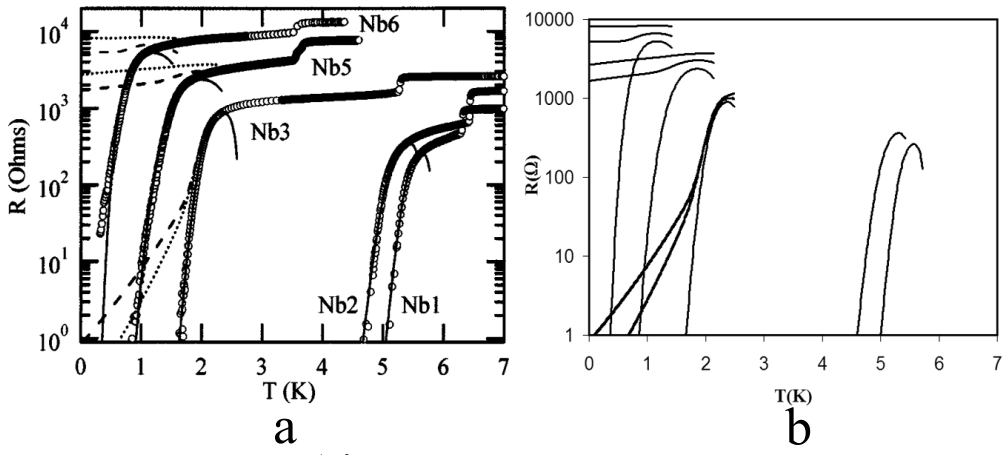

Figure 6.6: (a) shows the data and fitting from [10], (b) shows the data produced by my fitting program given the same input parameters. The two fits are identical proving that my program is producing the correct results.

6.2 Analysis of Niobium

The results from four Nb nanowires are presented here. These wires showed a broadening of the transition that increased as the wire dimensions were reduced. The wires Nb1 and Nb2 were fabricated on one chip, and Nb3 and Nb4 on another. The data from these wires are shown in figures (6.7) - (6.10). The R(T) characteristics Nb1(e)(f)(g), and Nb3(e)(f) were corrected from the raw data to account for the non linear I(V) plots, and Nb1(f)(e) and Nb2(e) were corrected for the temperature lag of the silicon diode thermometer. All

of these results were obtained using the continuous flow cryostat, and measurement electronics described in chapter 5. The wires are all $8\mu m$ long, and width and height information are described in the insets. Note that numbers preceded with a '$\sim$' are either an unreliable measurement, or estimates. This is because some of the wires were not not measured with an SEM in between subsequent mills, and so the dimensions had to be inferred from the general evolution of the wire size. The estimates were based on the rate of milling at the wire dimensions. The other measurements are reliable with an accuracy of $\pm$10nm.

In general, the wires all showed a similar response to being milled, the track dimensions were reduced and the normal state resistance increased. Samples Nb1, Nb2 and Nb3 showed an initial reduction of T_c, then an increase, followed by a final reduction of T_c at the lowest dimensions. This increase of T_c is a curious phenomenon as it is not obvious why argon ion beam milling would increase the T_c of niobium. To investigate further the T_c of each wire was plotted against the normal state resistance (Fig.6.11).

Because the wires were fabricated using a focused gallium beam, there would have been implanted gallium in the surface of the wires. This may have had an effect on the T_c, and be the cause of the increase in T_c observed in 3 of the wires. This notion is investigated in the next section.

6.2.1 Current Path

The measured dimensions of the wire may not correspond to the actual dimensions of the current path. Fabricating the wires using a FIB is likely to

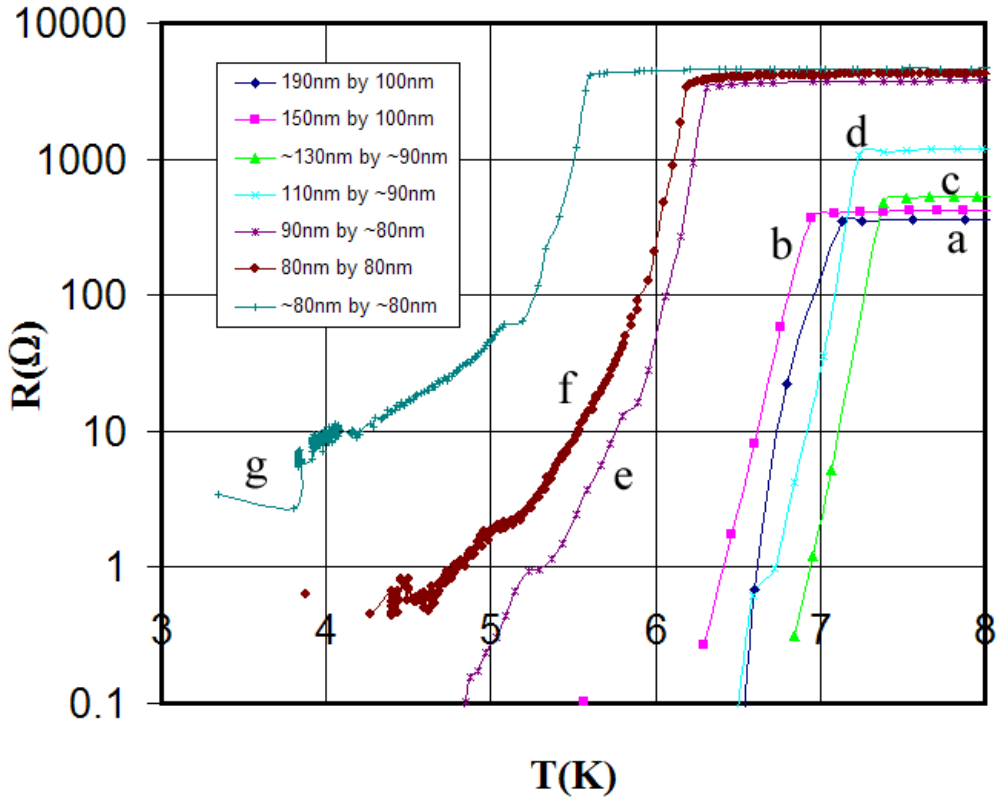

Figure 6.7: The R(T) characteristics of Nb1. From the initial wire (a) the sample was milled 4 times for 4 minutes (b - e) and then once for 20 seconds (f). The final plot (g) was measured using the on-chip thermometer. The sample had not been milled between plots (f) and (g), but stored for 6 weeks. This suggests that degradation of the niobium occurred as the properties had changed over time.

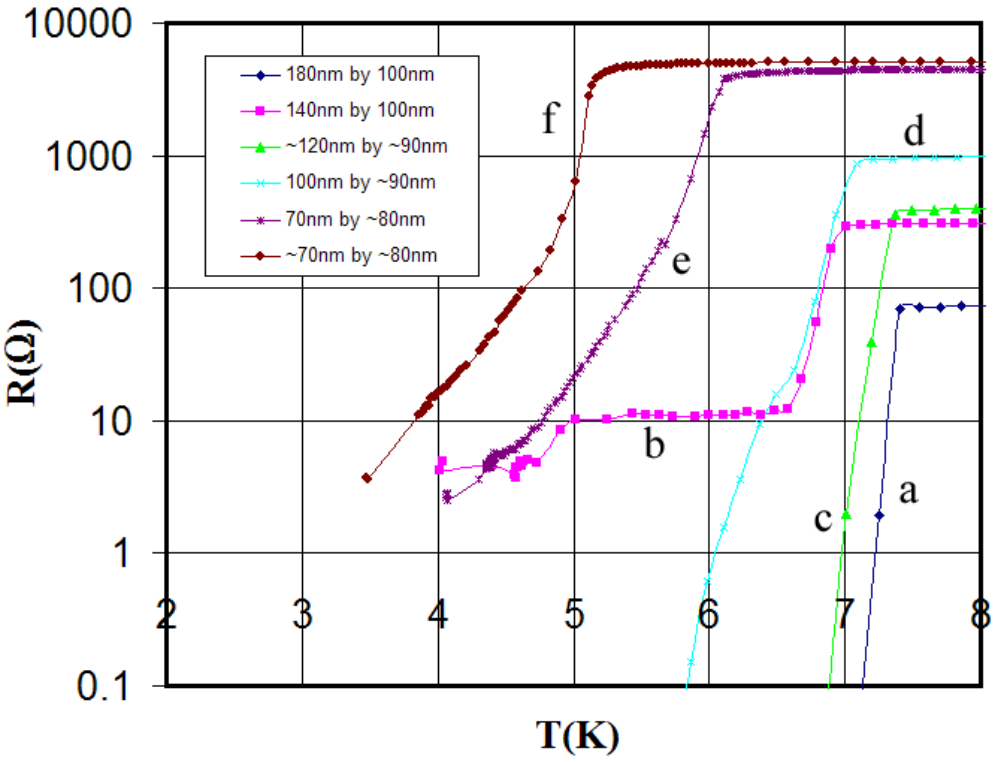

Figure 6.8: The R(T) characteristics of Nb2. From the initial wire (a) the sample was milled 3 times for 4 minutes (b - d) and then once for 4 minutes and 20 seconds (e). The final plot (f) was measured using the on-chip thermometer after storage for 6 weeks. Plot (b) departs from the normal pattern, and is believed to be a faulty reading caused by poor electrical contacts.

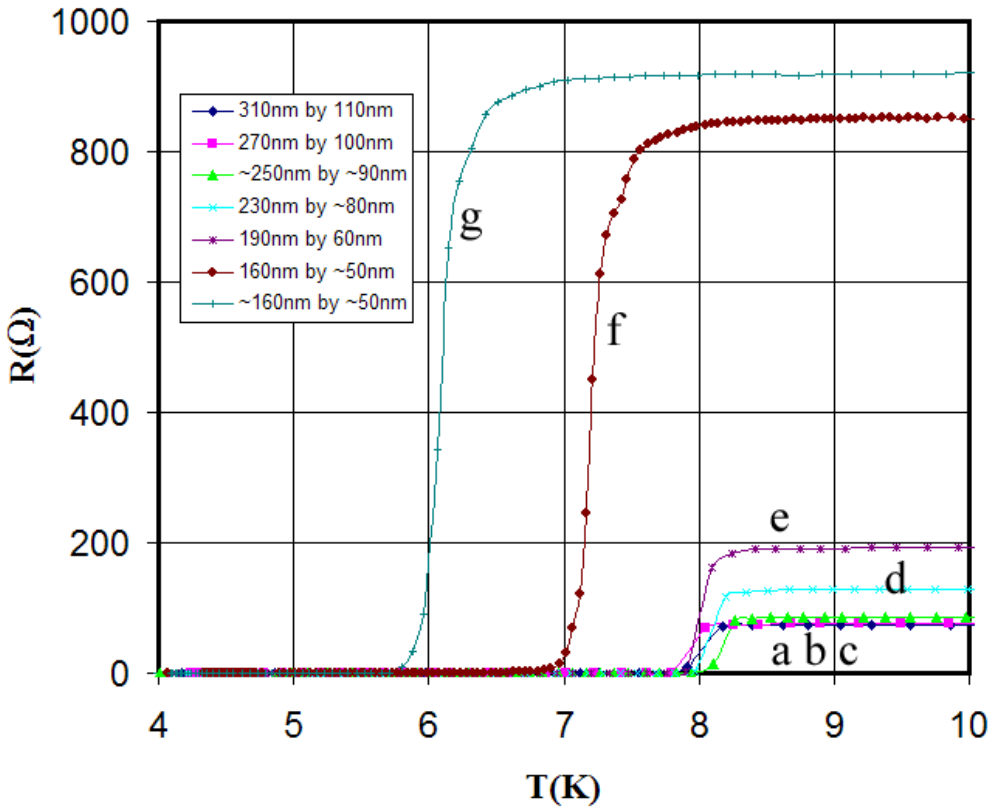

Figure 6.9: The R(T) characteristics of Nb3. From the initial wire (a) the sample was milled 4 times for 4 minutes (b - e) and then once for 5 minutes (f). The final plot (g) was measured using the on-chip thermometer after storage for 6 weeks.

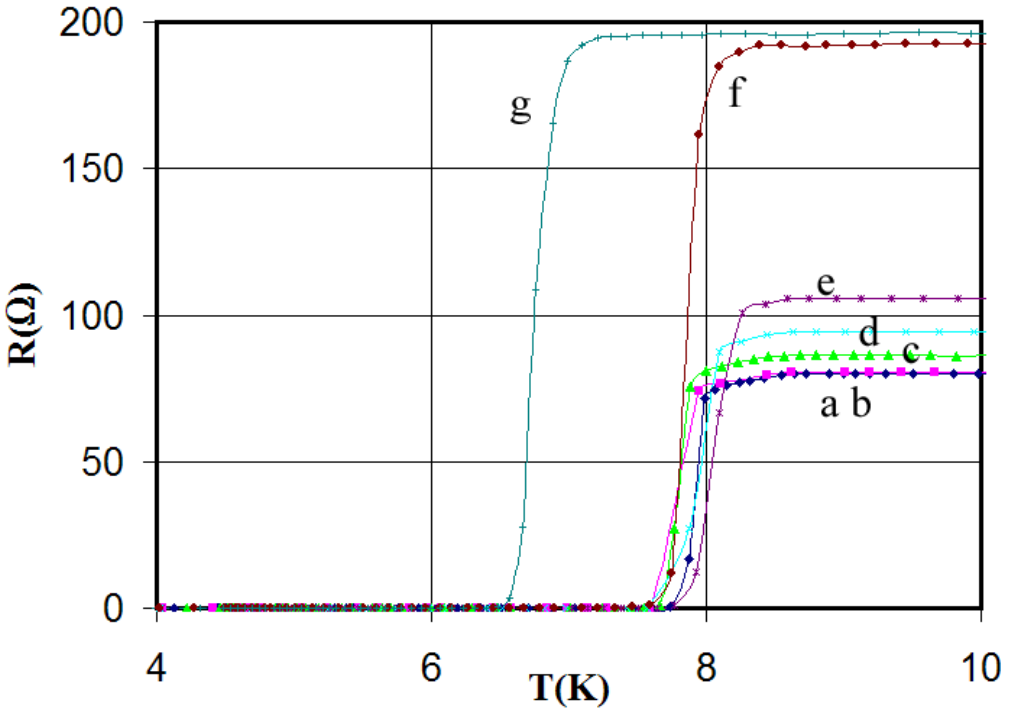

Figure 6.10: The R(T) characteristics of Nb4. From the initial wire (a) the sample was milled 4 times for 4 minutes (b - e) and then once for 5 minutes (f). The final plot (g) was measured using the on-chip thermometer after storage for 6 weeks. It was difficult to give measurements of the wire width and height as the wire had become obstructed by a piece of dust after the first mill, meaning that subsequent mills were non uniform along the length of the wire. The wire started with dimensions 300nm by 110nm.

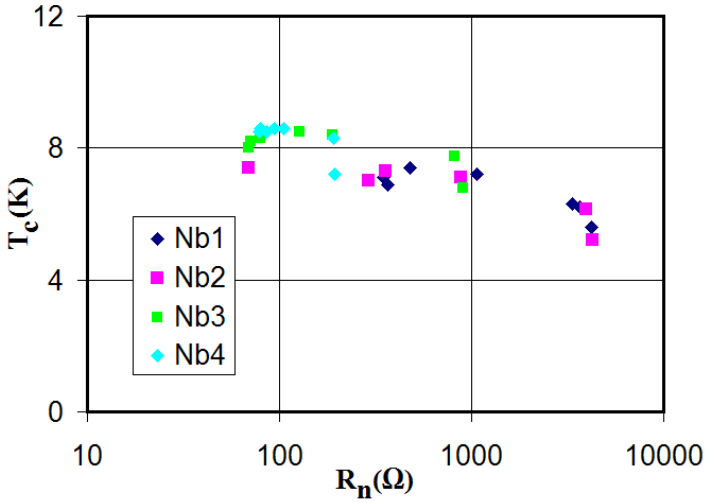

Figure 6.11: T_c plotted as a function of R_n of all of the Nb nanowires as they were milled. The samples showed a general reduction of T_c and increase of R_n as they were milled.

have damaged the outside surface of the wires because of the implanted gallium. High resolution transmission electron microscopy on niobium nanowires fabricated with an FIB have shown the damage caused by a gallium beam [66]. The images showed pure niobium cores around 100nm smaller than the external dimensions of the wire (Fig. 6.12).

One can gain an insight into the size of the Nb core in the nanowires fabricated in this project by calculating the apparent resistivity. The resistivity calculated from the measured resistance and dimensions of the various wires should be relatively independent of size. This was not observed. For the widest wires (300nm by 110nm) the resistivity at 10K was $\sim 3 \times 10^{-7}\Omega$m, and for the narrowest (80nm by 80nm) the resistivity was $\sim 3 \times 10^{-6}\Omega$m. Published values for the normal state resistivity of niobium are $1.4 \times 10^{-7}\Omega$m at room temperature, and $1 \times 10^{-8}\Omega$m for 100nm thick sputtered films at

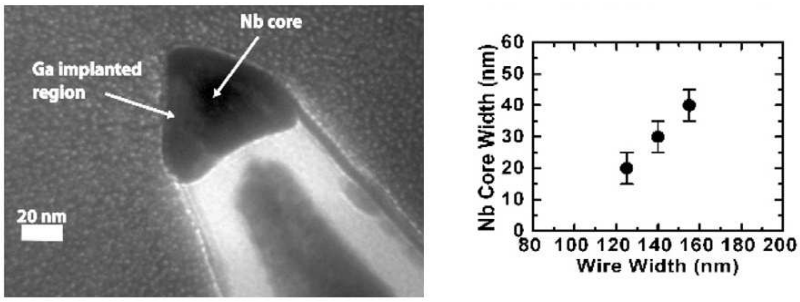

Figure 6.12: HR-TEM of a niobium nanowire fabricated using an FIB [66]. The energy of Ga-ions used was 30 keV, the same as in this project. This work shows that the niobium core width is ∼100nm less than the external dimensions of the wire.

10K [67]. This shows that the measured resistivity of the wires is larger than it should be, with the error increasing as the wires are reduced in size.

This error can be accounted for by the current being restricted to a path much smaller than the external dimensions of the wire. The calculated resistivity of the wire is directly proportional to the cross sectional area. Therefore, using a smaller cross sectional area in the calculation of the resistivity leads to more reasonable values.

This hypothesis was tested in the following way; if the resistivity is assumed to be $\rho = 1 \times 10^{-8}\Omega$m (at 10K), one can make an estimate of the current path of the wire. Here I assumed for simplicity that the wires were of circular cross section and were equally damaged all the way round. I have also assumed that the damaged region did not contribute to the resistance measured. This is not strictly true as the resulting NbGa compound will have a finite resistance. However, research on the effect of Ga implantation in thin Nb films has shown an increase in resistivity of the resulting compound which increased as a function of Ga dosage [68]. Therefore the damaged region will

have a higher resistance than the Nb core.

The $\surd$(estimated wire cross section) plotted against the $\surd$(measured cross section) of a number of wires is shown in figure (6.13). This leads to a comparison of the difference between the measured and estimated dimensions of the wire. When fitted with a straight line, the intercept with the vertical axis gives the average difference between the measured size of the wire and calculated size.

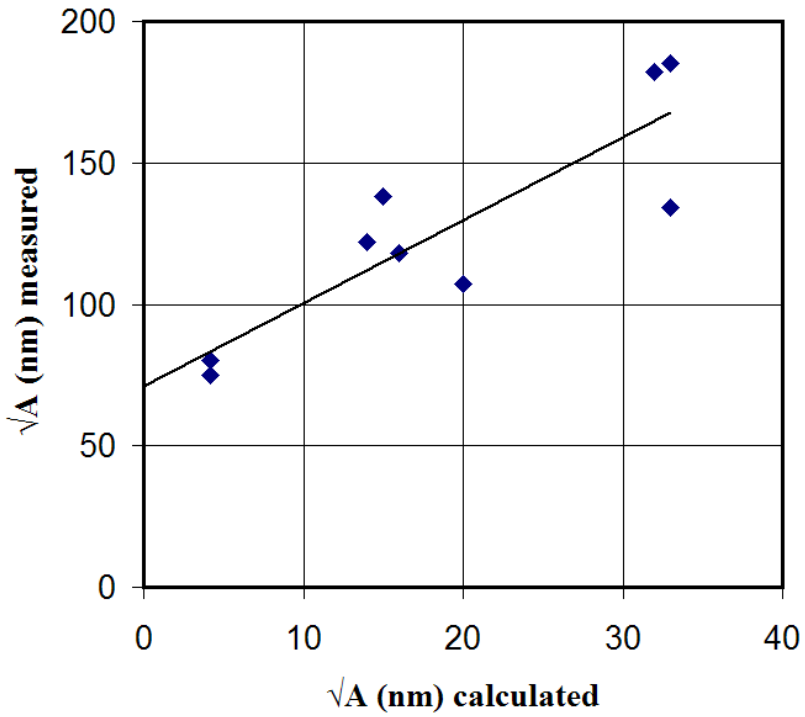

Figure 6.13: The horizontal axis plots the square root of the calculated cross sectional area of a series of wires derived using $L = 8\mu$m, $\rho = 1\mu\Omega$cm and the measured resistance at 10K. This is plotted against the square root of the measured cross sectional areas of the wires. A straight line has been fitted to the data, and shows an intercept at 71nm with an error of $\pm$14nm, this gives an estimate as to the size of the damaged region of 57-85nm.

The intercept is at 71nm, suggesting that the damaged region around the

outside of the core is ∼70nm thick. The error on the intercept was calculated using least squares regression, and found to be ±14nm, giving an estimate of the size of the damaged region to be 57-85nm wide. This is a slightly higher value than that predicted by the SRIM simulation (Fig.3.3) [66], where a total damage of ∼40nm was predicted. However it is less than the 100nm damage shown in figure (6.12). In either case 71nm is not unreasonable, and gives a crude indication as to the amount of damage caused. Taking this value for the damage one can estimate the size of the conductive channel in the centre of the wires which ranges from 115nm for the widest wires down to a few nm for the narrowest.

The gallium implantation may also have an effect on the T_c of the wire. The properties of the compound NbGa has been shown to have a higher T_c than pure Nb [69], which depends on the ratio of Nb to Ga. However, implanting Ga into Nb using an FIB is not the same process as making a bulk compound. Indeed, there is evidence showing that gallium implantation via FIB milling in thin Nb films reduces T_c proportionally to the dose of Ga ions [68]. From this evidence one can picture the wires as having a pure Nb core surrounded by a damaged region that has a decreasing T_c moving radially outwards from the wire.

It is worth noting here that the argon ions used to reduce the wire dimensions will also become implanted. However as the energies are much smaller than the gallium ions (argon = 1keV, gallium = 30keV), the argon ions are only expected to penetrate ∼2nm into the Nb. This estimate was based on SRIM analysis. Therefore the effect of argon implantation is negligible.

It was thought that the reduction of the Ga damaged region via Ar^+

beam milling might account for the increase of T_c observed in 3 of the wires. However it is difficult to see how the removal of the external damaged region might increase the T_c of the whole wire. This is because the T_c of the undamaged central region would be higher then that of the surrounding material, and so would become superconducting before the the rest of the wire, effectively shorting it. Therefore the increase of T_c observed in these wires remains unexplained.

6.2.2 Phase Slip Fitting

The data that showed a broadening of the transition was fitted with the theoretical model for phase slips. The fitting was done by reading the experimental data into the analysis program, and then adjusting the variables in the program to fit the data. Because there are 4 fitting parameters, the analysis was done in a systematic way. The R(T) characteristics that were analysed are Nb1(d)(e)(f)(g), Nb2(d)(e)(f), Nb3(e)(f)(g) and Nb4(f)(g).

The fitting parameters available to fit the data are the length of the wire L, the coherence length $\xi(0)$, the transition temperature T_c and the normal resistance R_n. In addition there are two extra parameters 'a' and 'B' which are used in the fitting of the QPS theory covered in chapter 4.3.3 (Eqn.4.27). The parameters a and B are arbitrary pre-factors that have been used in published work to fit data attributed to QPS. With so many parameters it is sensible to attempt to fit the data in a logical order, and this was done as follows.

All of the wires measured had a well defined length of $8\mu m$, and so this was

kept constant. The coherence length of bulk niobium is 30nm, however it may well differ in nanowires, particularly ones which have been gallium damaged. Even so, this was kept constant to begin the analysis. The normal state resistance is the resistance measured just above the transition temperature. As the T_c is not well defined this was estimated as the measured resistance at ~9K, as the wires have a weak temperature dependence at this temperature. The transition temperature of the wires varies with wire dimensions, and so initially this was used as the only fitting parameter. The results of using only T_c as a fitting parameter were poor, with the theoretical model not fitting the experimental data at all well (Fig. 6.14). The fit to only four of the wires is shown here for clarity.

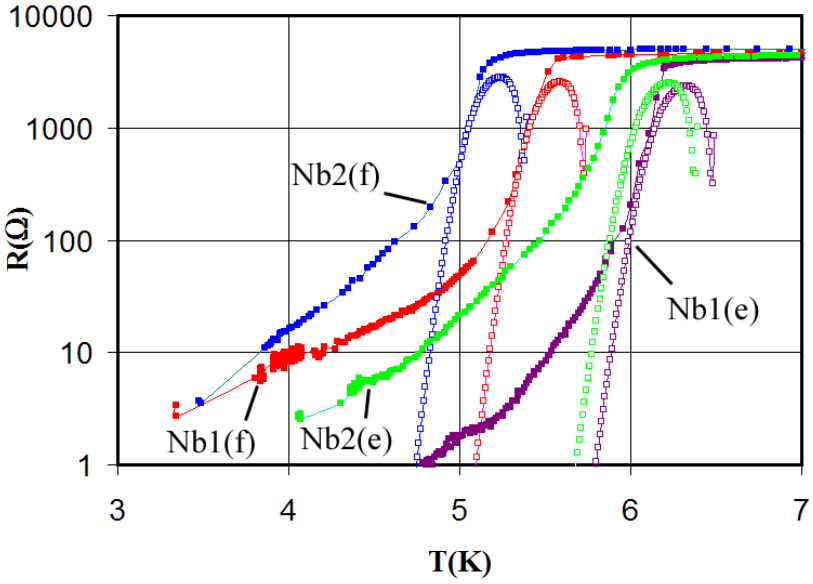

Figure 6.14: Fitting some of the data using only T_c as a free parameter. The solid squares are the experimental data and the empty squares the fit. The T_c used for Nb1(e), Nb1(f), Nb2(e), Nb2(f) are 6.44K, 6.5K, 6.4K and 5.4K respectively.

Because of the poor fitting, the coherence length was introduced as a second fitting parameter. In this case the fit was slightly better, although unreasonably high values of $\xi(0)$ (50nm-400nm) were needed to fit the data.

The main inaccuracy caused by the fit was the maximum resistance of the theoretical model being too low to model that of the wires. Therefore, another fit was attempted, this time keeping $\xi(0)$ constant at 30nm and using T_c and R_n as fitting parameters. Under these conditions the best fits were much better as shown in figure (6.15).

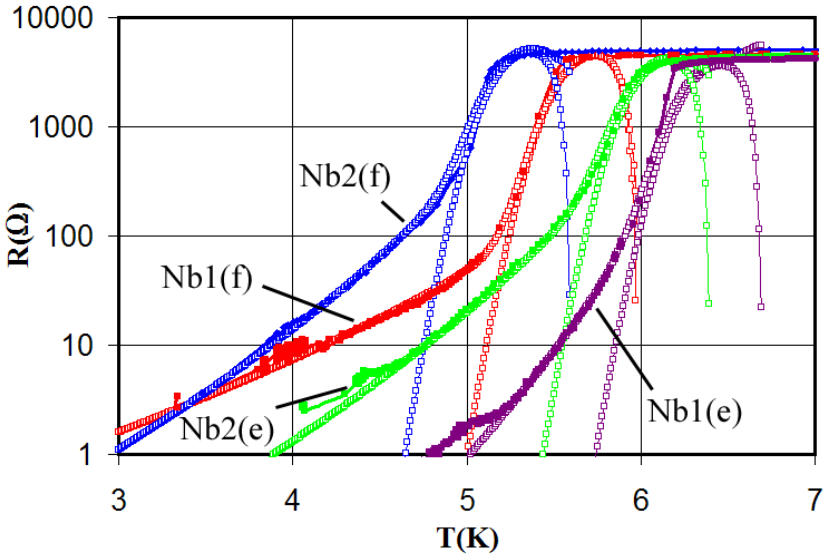

Figure 6.15: Fitting some of the data using only T_c and R_n as a free parameters, the coherence length was kept as 30nm and the length of the wire 8μm. The fit for just the thermal contribution, and the addition of quantum phase slips are shown. The T_c used for Nb1(e), Nb1(f), Nb2(e), Nb2(f) are 6.6K, 6.7K, 6.4K and 5.6K respectively. The R_n used are 6100Ω, 6500Ω, 7000Ω and 8500Ω respectively. The pre-factors used to fit the resistive tails are (a,B)=(0.4,1),(0.36,1),(0.27,0.1)and(0.3,0.1).

The pre-factors a and B were used to fit the low resistance tails in (6.15) to the theory of quantum phase slips. When a and B were kept at unity the

contribution of QPS to the overall resistance was always much lower than that of thermal phase slips. The QPS contribution could only be increased by using very low values for a and B. The choice of what value to use was arbitrary, and has no physical basis. Published results [9] used the values a = 1.3 and B = 7.2, which in this case produced a very bad fit to the data. It should be noted that careful choice of the pre-factors a and B can lead to the fitting of almost any curve. Therefore, the only situation in which one would be confident in their validity was if a single pair of pre-factors fitted an entire family of R(T) characteristics. This was not observed in this case, therefore it is very unlikely that the lower resistive tails are caused by quantum fluctuations.

When T_c and R_n were used as free parameters the fit to the wires from Nb1 and Nb2 was good, but the fit to Nb3 and Nb4 was poor. Satisfactory fits to Nb3 and Nb4 were only made by using T_c, $\xi(0)$ and R_n as free parameters. These are shown in figure (6.16).

During the analysis it was found that a good fit could only be obtained by using very large values (above 100nm) for the coherence length. This is not representative of the coherence lengths in these samples. The coherence length in bulk niobium is 30nm and, as this is related to the mean free path of the electrons, it is expected to be lower in very narrow granular wires. Is should be noted that, in the theoretical model, reducing the length of the superconductor has the same effect as increasing the coherence length. This is because of the dependence of the energy barrier on these variables (Eqn.6.2). Bearing this in mind, a more physical explanation of the fitting would be a reduction of the length of wire used. This may occur if the phase

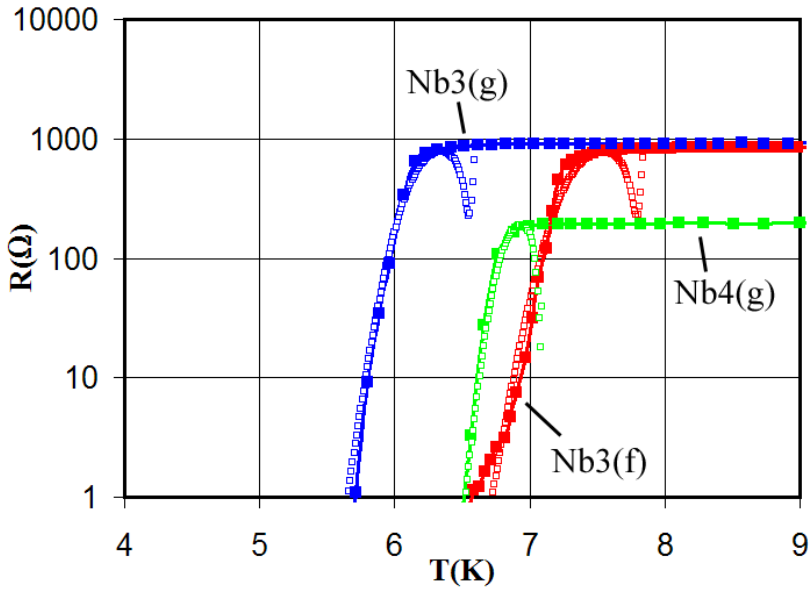

Figure 6.16: Fitting to Nb3 and Nb4 using T_c, R_n and $\xi(0)$ as a free parameters, the length of the wire was kept as 8μm. The T_c used for Nb3(g), Nb3(f), Nb4(g) are 6.6K, 7.85K and 7.1K respectively. The R_n used are 1400Ω, 1400Ω and 340Ω respectively. The coherence lengths used are 160nm, 160nm and 300nm.

slip behaviour is dominated by a small, constricted region, and not evenly along the length of the wire.

It has also been found that all of the theoretical fits required a larger normal resistance R_n than was measured. The increase of R_n needed to fit the data was remarkably consistent over all of the samples, a factor of 1.6-1.7 larger than the measured R_n. It was thought that this inconsistency may be due to taking the incorrect resistance as R_n, taken to be the measured resistance at 9K. However, this is not feasible as the required values of R_n are very much higher than the measured resistances.

One possible explanation of the increased R_n required can be attributed to the damaged region around the Nb core. Acting as a parallel resistor to

Nb wire it would effectively reduce the R_n of the entire wire. The Nb region within which the phase slips occur would in fact have a higher R_n than that measured. Even so, the values of R_n used are unreasonably large even for the Nb core, and so a more logical parameter to change would be the cross sectional area of the wire. In the analysis so far, the cross sectional area A was not available as a variable parameter. To be able to change it one needs to employ the original LAMH version of ΔF_0 Eqn.(6.1).

A final fit was made to the data, this time using the cross sectional area A, T_c and R_n as free parameters. In this case the length of wire was kept as the measured length 8μm. The coherence length and critical field are unknown and so were kept fixed at reasonable values known for Nb, $\xi(0) = 10$nm and $H_c(0) = 2.58 \times 10^{-7}$ A/m. The coherence length of 10nm is comparable to that used to fit published work on Nb nanowires (8.5nm-16.5nm), and that found in polycrystalline Nb films ($\sim$7nm) [10]. The results of the fitting are shown in figures (6.17),(6.18) and (6.19).

Fitting the data in this way resulted in a good fit to all of the data. The T_c varied from 6K - 8K in the samples, and the cross sectional area A ranged from 5^2nm^2 to 13^2nm^2. The R_n was in most cases the measured R_n, although it had to be increased slightly to get a good fit to the data with the highest resistance. Even so the increase of R_n was a lot more reasonable to that of the earlier fits, increasing by an average factor of 1.1 rather than 1.7. These results suggest that, if the broadening is caused by thermally activated phase slips, the wires have a diameter that reduces from 8nm-5nm as they are ion beam milled. These results can be compared to the diameters of wires derived from the estimate of gallium damage (Fig.

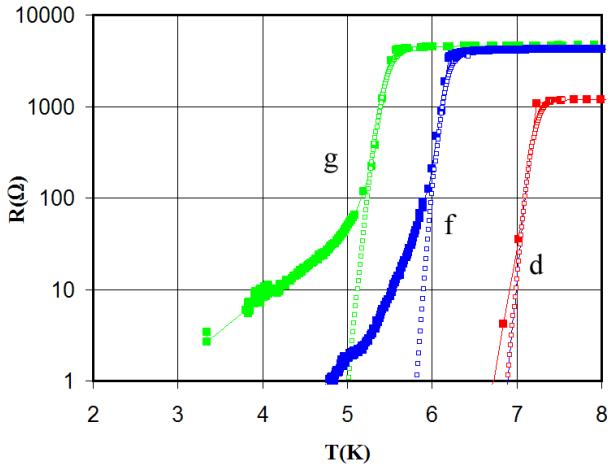

Figure 6.17: Nb1(d),(f) and (g). The cross sectional areas used to fit the data were, 8^2nm^2, 7^2nm^2 and 5^2nm^2 respectively. The T_c used were, 7.7K, 6.55K and 6K respectively.

6.13). The damage was calculated to be 71±14nm, resulting in a conductive core much smaller than the external dimensions of the wires. The external dimensions of the narrowest wires were 70nm and so, given the damage, a core of 5nm is feasible. However, the damage to the widest wires resulted in an estimate for the core size to be ∼115nm, which is much larger than the 8nm predicted by the phase slip fitting. Therefore there is an inconsistency between the models when applied to large and small wires.

In practice the wires may not have the same $\xi(0)$ and $H_c(0)$ as these parameters may reduce with sample size. A smaller $\xi(0)$ and $H_c(0)$ would require a larger A to obtain the same fit, and so the wire diameters predicted by this theory may not be as small as 8nm-5nm. Without being able to measure $\xi(0)$ and $H_c(0)$ directly it is difficult to estimate the actual cross sectional area. This could account for the inconsistency between the core size estimate from the damaged region and the phase slip fitting. In any

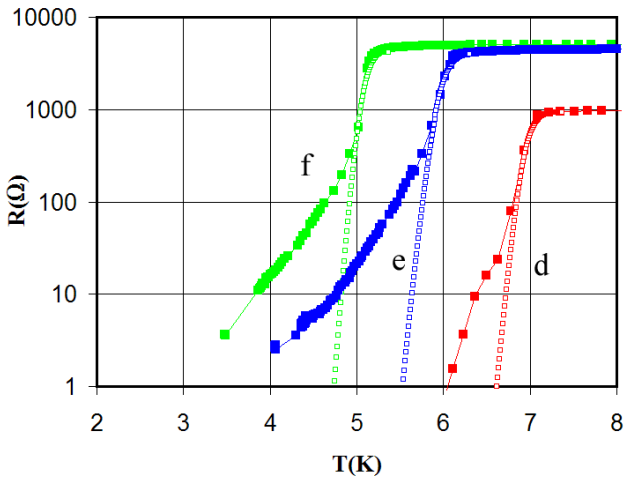

Figure 6.18: Nb2(d),(e) and (f). The cross sectional areas used to fit the data were, 7^2nm^2, 6^2nm^2 and 5.5^2nm^2 respectively. The T_c used were, 7.55K, 6.54K and 5.5K respectively.

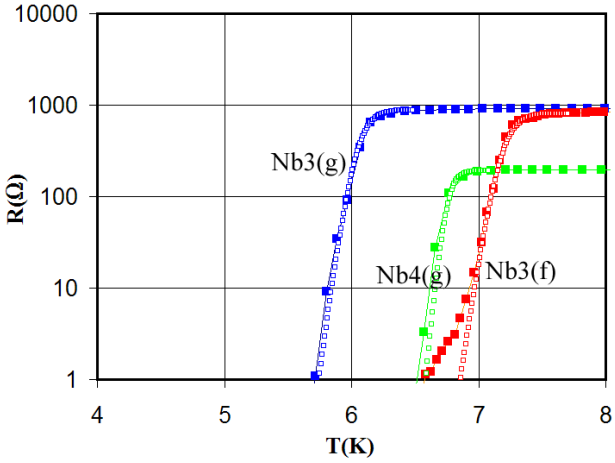

Figure 6.19: Nb3(f) and (g), and Nb4(g). The cross sectional areas used to fit the data were, 7^2nm^2, 6^2nm^2 and 9^2nm^2 respectively. The T_c used were, 7.85K, 6.67K and 7.2K respectively.

case, it gives an indication as to the wire diameters that is not unreasonable.

6.2.3 V(I) Plots

As already noted, the resistance measurements of the nanowires were obtained from measuring their V(I) characteristics in the linear region. However, further analysis of the V(I) characteristics can reveal information about the nature of the dissipation in the nanowires. To understand this, it is helpful to re-visit the theory of phase slips, to ascertain what V(I) characteristics it predicts.

According to the theory presented in Chapter 4 the dissipation is a result of voltage jumps caused by phase slippage, the voltage being proportional to the rate of change of phase,

$$\frac{d}{dt}\gamma = \frac{2eV}{\hbar}. \tag{6.3}$$

The dynamics of the phase slip process is described by analogy with the washboard potential (Fig. 6.20). In this situation, an applied current causes a tilt to the washboard potential making phase slips down the potential more likely than up it. According to Eqn. (6.3), these phase slips manifest themselves as voltage jumps. These voltage jumps are averaged over time to give a resistance.

At low bias currents the voltage increases linearly with current, but at higher currents the V(I) dependence becomes non-linear. To appreciate this, it is useful to express the voltage as a function of the current and barrier height as given by LAMH theory. The current is related to the barrier height,

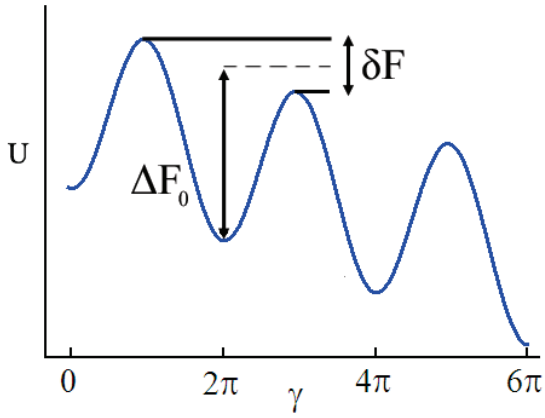

Figure 6.20: The washboard potential governing the phase slip process (it is shown as sinusoidal for illustration purposes only). The barrier height is given by ΔF_0. The difference in barrier heights, δF increases with increasing current I. This makes the phase more likely to propagate down than up it. Note that the washboard potential is a useful analogy in picturing the dynamics of phase slips, and that the real mechanism is more complex [1] [2].

$$\delta F = \frac{h}{2e} I. \tag{6.4}$$

The rate of change of phase was shown in Chapter 4 to be,

$$\frac{d\gamma}{dt} = \Omega \left[exp\left(-\frac{\Delta F_0 - \delta F/2}{k_B T} \right) - exp\left(-\frac{\Delta F_0 + \delta F/2}{k_B T} \right) \right] \tag{6.5}$$

And so by substituting in (6.3) and (6.4) one obtains the relationship between the voltage and current,

$$V = \frac{\Omega \hbar}{e} e^{-(\Delta F_0 / k_b T)} \left[e^{(hI/4ek_bT)} - e^{-(hI/4ek_bT)} \right]. \tag{6.6}$$

This relationship can be plotted to see the relationship between V and I

(Fig. 6.21).

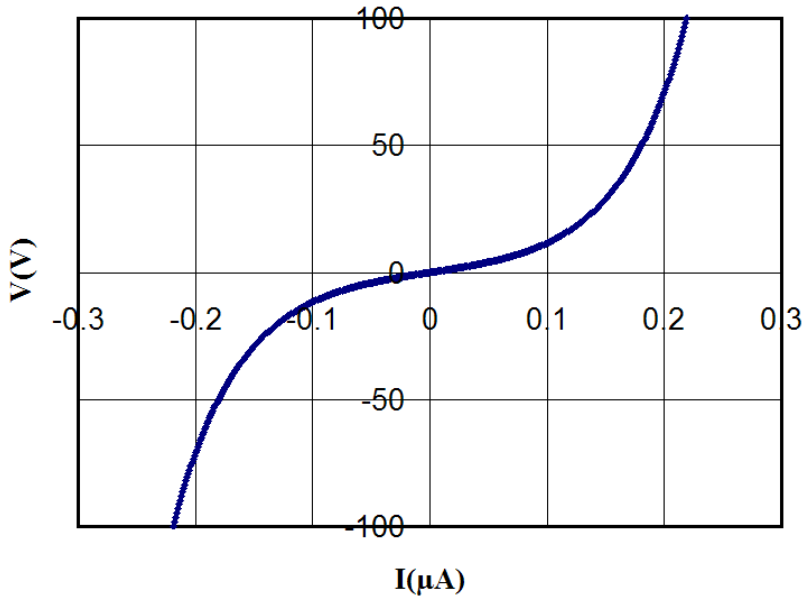

Figure 6.21: A theoretical plot of the V(I) characteristics expected from the phase slip process using Eqn.(6.6), and using reasonable experimental values; $R_n = 4000\ \Omega$, $\xi_0 = 30$nm, L = 8μm, $T_c = 7$K.

As can be seen in figure (6.21), at low currents Eqn.(6.6) varies linearly with I, because the exponential terms are approximately equal. But at larger currents one of the exponential terms dominates, causing the voltage to rise exponentially with current. The current below which the relationship is linear is given by [70],

$$I_0 = \frac{4ek_bT}{h} = 0.013\mu A/K. \tag{6.7}$$

At the temperature range 4K-10K, I_0 is in the region 0.05-0.1μA and decreases with decreasing temperature.

One can now compare these theoretical predictions with the observed

V(I) characteristics in the Nb nanowires. The first thing to note is that the measuring electronics were limited to a minimum current sweep of $1\mu A$. With a maximum of 1000 data points on the a sweep this limited the minimum resolution in current of $\sim$10nA, just on the range of I_0 at the lowest temperatures. In the $1\mu A$ range, one should observe the linear increase of V at low currents, and then an exponential increase as I exceeds I_0. This was not observed. The V(I) characteristics were linear over the whole range at all temperatures apart from near the transition. This is evidence to suggest that the resistance measured was not caused by phase slips.

Also, the non-linear behaviour observed in the V(I) characteristics close to the transition is in complete contradiction with the theory. As the temperature was increased towards the transition the V(I) characteristics exhibited a decreasing I_0. As we can see from Eqn.(6.7), this is the opposite behaviour to that expected. A plot of the I(V) characteristics with temperature is shown in figure (6.22).

One can determine the apparent I_0 as a function of temperature by fitting the data Fig.(6.22) with the function,

$$V = A\left[e^{\left(\frac{I}{I_0}\right)} - e^{-\left(\frac{I}{I_0}\right)}\right]. \tag{6.8}$$

Where A is a pre-factor and I_0 is the critical current. This fitting was done to the data in Fig.(6.22) to determine I_0 as a function of temperature. This is shown in Fig.(6.23).

This decrease in I_0 with temperature is the opposite to that predicted by LAMH theory, and so this behaviour cannot be attributed to phase slips.

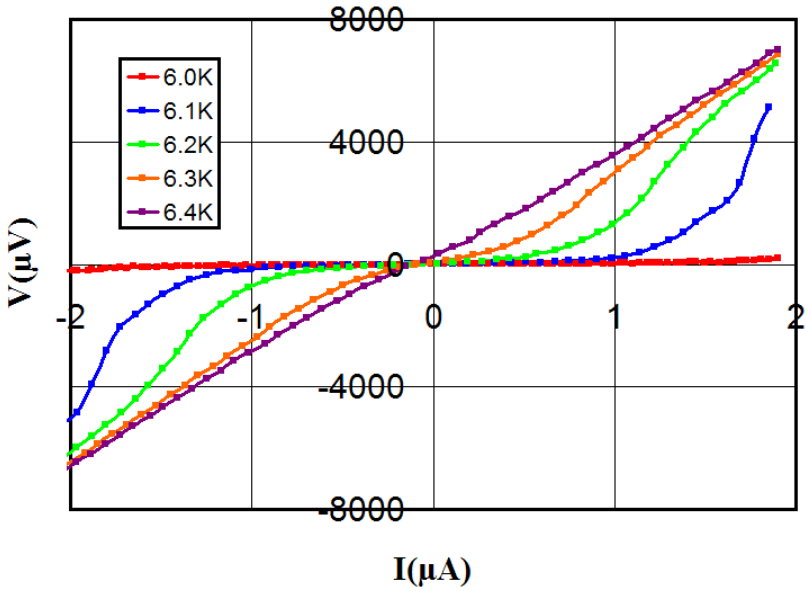

Figure 6.22: The V(I) characteristics of Nb1(g) close to T_c. As the temperature is increased the liner portion of the V(I) characteristics gets smaller and disappears at T_c.

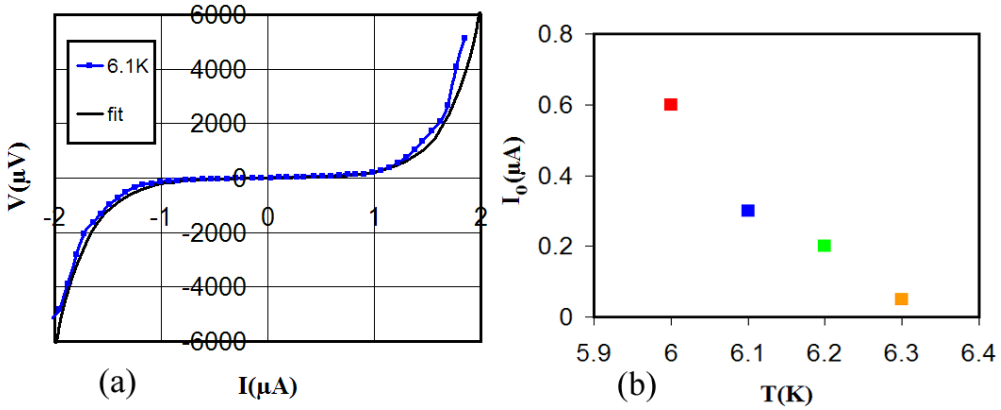

Figure 6.23: (a) shows an example of fitting the V(I) characteristics with the function V=A(exp(I/I_0)-exp(-I/I_0)). For these fits the pre-factor A was taken to be 8V. (b) shows how I_0 decreases with temperature close to T_c.

To gain further insight into the nature of the dissipation that is causing this behaviour the data in Fig.(6.23)(b) can be re-plotted. The critical current of

dissipative processes generally takes the form,

$$I_c \propto \left(1 - \frac{T}{T_c}\right)^n, \tag{6.9}$$

the value of n can give a clue as to the type of process that is involved in the dissipation. The value of n can be found by expressing eqn.(6.9) as,

$$log\,(I_c) = k + n \cdot log\left(1 - \frac{T}{T_c}\right), \tag{6.10}$$

where k is a constant. By plotting $log(I_c)$ against $log\left(1 - \frac{T}{T_c}\right)$, and fitting with a straight line, one can find the value of n. This is shown in 6.24, where the T_c was taken to be 6.4K,

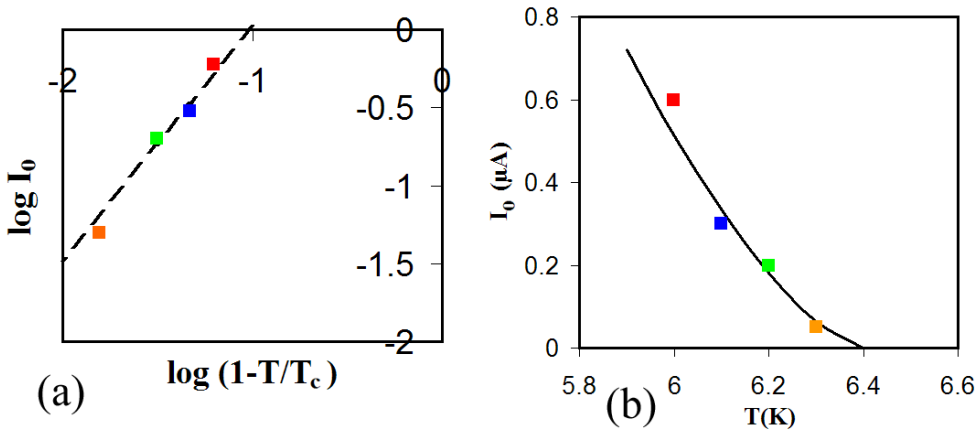

Figure 6.24: (a) shows the data fitted with the function $log(I_0) = 1.52 + 1.5log(1 - T/T_c)$. (b) shows this function fitted to the original data. From the relatively good fitting it suggests a value for n to be 3/2.

A series of fits were made to the data in 6.24(a), each using different values for n of 1, 3/2 and 2. The best fit was found using $n = 3/2$, and a value of 1.52 for the constant k. When these values were used to fit the

original data, a reasonable fit was found, as shown by 6.24(b). This suggests that the dissipation is caused by pair breaking, as the value for n in this process is derived from Ginzberg-Landau theory to be 3/2 (chapter 4.4.3) [60].

Dissipation due to flux flow may also be a contributing factor to the value of the critical current. As the temperature is increased, thermal fluctuations allow flux lines to become depinned and start to cause dissipation. Deviation of the value of the critical current away from the pair breaking regime has been observed in other samples, and attributed to flux flow [71]. However, in this case, one would require more data points to be able to observe this deviation.

Another behaviour that does not agree with the theoretical model was exhibited by the V(I) characteristics at low temperatures. At the lowest temperatures, linear V(I) relationship was observed at much larger currents ($10\mu A$) than predicted by the theory. The V(I) characteristics of sample Nb1(f) at 4K are shown in figure (6.25).

The V(I) characteristic (Fig. 6.25) does not appear to fit with the theoretical model as the characteristic is hysteretic, and the voltage does not appear to increase exponentially with current above the critical current. This is again evidence to suggest that the behaviour at these low temperatures is not caused by phase slips.

In this case behaviour is likely to be due to the current exceeding the critical current I_0 of the wire and turning it normal. Above the critical current the resistance of the linear region of (Fig. 6.25) was measured to be $4.3k\Omega$, which is close to the normal state resistance of the wire of $4.1k\Omega$

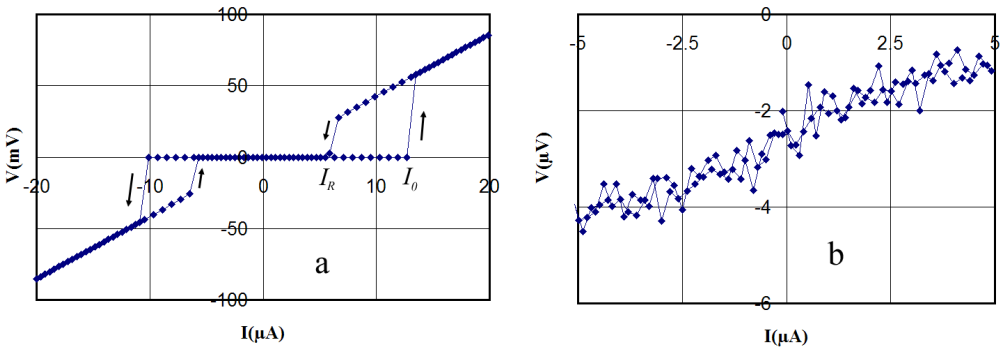

Figure 6.25: The V(I) characteristics of Nb1(f) at 4K. (a) shows a hysteretic characteristic at a current sweep of $\pm 20\mu A$, and (b) shows the linear portion of the V(I) curve at a current sweep of $\pm 5\mu A$. The voltage offset in (b) is a result of the measurement electronics and does not effect the calculated resistance.

measured above T_c. As the current is reduced from the maximum the re-trapping current I_R is lower than the critical current I_0. This hysteresis is likely to be caused by hot spot formation as described in chapter 4.4.2 and [63]. In this case the wire is still in the normal state below I_0 as it dissipates heat, and then turns superconducting when the temperature reduces below T_c.

In conclusion, analysis of the V(I) characteristics has brought into question whether the observed broadening of the superconducting transitions are caused by the phase slip process. They are more likely caused by flux flow and hot spot formation. It should be noted that the published literature rarely contains an in depth analysis of the V(I) characteristics of the samples. Much of the data R(T) data comes from V(I) characteristics where I is kept below I_0. There are some exceptions [10] [6] [25], who provide the V(I) characteristics, and these indeed appear to fit the theory. However, to my

knowledge, no one to date has fitted a range of V(I) characteristics with the LAMH theory at many temperatures, to show the temperature dependency of I_0.

6.2.4 Niobium Conclusions

In conclusion it appears that the resistance exhibited by the nanowires below T_c is not caused by phase slips. Even though the R(T) characteristics have a reasonable fit to LAMH theory, the behaviour of the V(I) characteristics can not be ignored. The behaviour observed in the V(I) characteristics does not fit with LAMH theory at all well. Therefore, it is unlikely that phase slips are the cause of the broadening of the transition.

The resistance below T_c must have a physical origin. The main candidate of this resistance is the gallium damage in the Nb wires. It has been shown that the T_c of niobium goes down with increased Ga poisoning, therefore the broadening of the transition may be caused by different parts of the wires going superconducting at different temperatures. A similar effect has been shown in nanowires aluminium where the T_c depends on the physical dimensions of the superconductor [6]. When the wires had an uneven cross sectional area along the length, parts of the wire became superconducting before others, causing a broadening of the transition. It is clear that the T_c of Nb goes down with sample size as well. So if the Ga damage is not even over the length of the wire, there may be a variation of T_c because of sample dimensions *as well* as the T_c change due to implantation.

These effects due to the Ga implantation complicate the system that

is being measured. This makes it difficult to observe phase slip behaviour because of the extra effects introduced by the Ga. For this reason it would be better to fabricate nanowires using a less invasive technique like e-beam lithography. Indeed this was planned from the beginning of the project, but due the lack of direct access to an e-beam system, and the difficulty in producing wires so small, this was not completed.

6.3 YBCO Results

Many samples of YBCO were fabricated and measured over the course of the project. The dimensions of wire required for YBCO to exhibit phase slips was less well defined than for Nb, as there is published data for only one wire that exhibited phase slip like characteristics [25]. This wire was fabricated from a 150nm thick film, had a width of 500nm and a length of 10μm. Therefore I concentrated on fabricating wires with similar dimensions to this.

The most compelling results came from a sample on which a range of wire widths were fabricated from the same film. These showed a range of R(T) characteristics again reminiscent of the broadening due to phase slips, although the transitions exhibited some extra effects. The results from these wire are shown in figure (6.26).

The general trend of these wires is that narrower and longer wires tend to have a larger resistance, and a lower T_c. The notable exception to this are wires (e) and (f) which, although having a larger width than (d) they have a much larger resistance. This behaviour is representative of many of

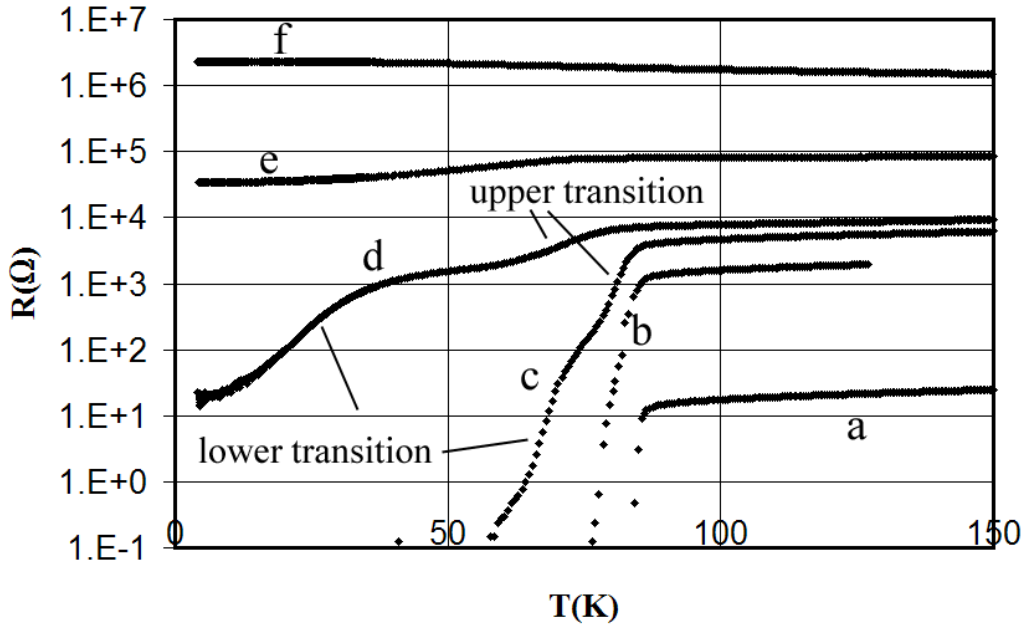

Figure 6.26: The R(T) characteristics of a series of wires fabricated from the same 150nm film. The dimensions of the wires,(length by width) are: (a) = (4μm by 4μm), (b) = (6.9μm by 250nm), (c) = (7.5μm by 205nm), (d) = (1.7μm by 80nm), (e) = (5.9μm by 135nm), (f) = (6.6μm by 120nm) respectively. Wires (c) and (d) exhibit a double hump behaviour, these features will be refered to as the upper and lower transitions.

the other samples fabricated in YBCO, where wires that were fabricated in the same way exhibited very different R(T) characteristics when measured. This behaviour was also found in Ref.[25], where the resistivity was greatly different in samples of similar dimensions. The two main mechanisms that would effect the resistance of wires is the extent of the gallium implantation and the oxygen content, which may vary from wire to wire. It was surprising that (d), with a width of only 80nm, exhibited such a low resistance. This may have been due to the length being only 1.7μm, reducing the probability of large imperfections along the length.

Wires (b), (c) and (d) exhibit broader transitions than (a), which could be interpreted as dissipation due to phase slips. The transitions of (c) and (d) show similar behaviours, where there is an initial decrease in the resistance with temperature, followed by a lower temperature resistive foot. The lower transition may be anomalous as the V(I) characteristics of these lower transitions showed a curious behaviour Fig.(6.27(b)).

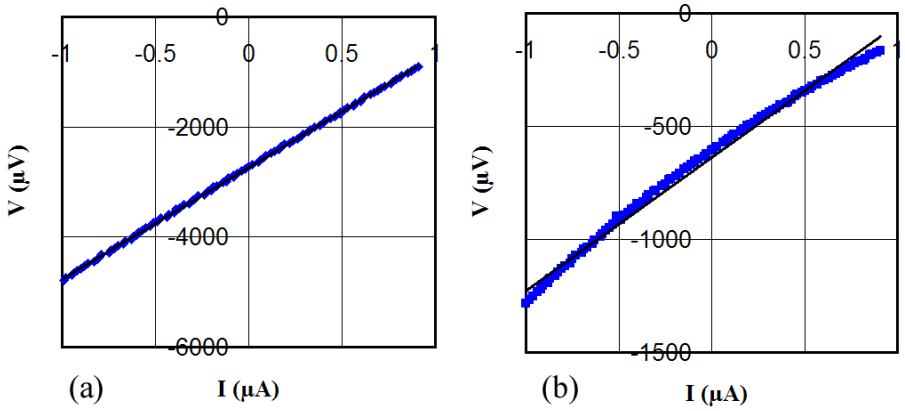

Figure 6.27: V(I) characteristics taken from wire (d). (a) shows a V(I) characteristic at 60K from the upper transition. (b) shows a V(I) characteristic at 40K from the lower transition. The straight line in (b) is the best fit used to determine the resistance. The voltage offset in both characteristics is caused by the measurement electronics and does not effect the calculation of the resistance.

The non-linear V(I) characteristics are peculiar in that they are not symmetrical either side of the voltage axis. This is clearly not physical as it suggests that resistance of the wires depend on the direction of the current, which cannot be true. This also means that the characteristics can not be corrected for as there is no way of knowing what the actual resistance of the wire is. Therefore, there are serious doubts as to the validity of the lower transitions of (c) and (d) as the resistances have been calculated from the

best fit to these data. The upper transitions of these wires did exhibit linear V(I) characteristics, and so it has been assumed that these are still valid data. It should be noted that all of V(I) characteristics of the other samples were linear at all temperatures.

The set of wires was milled in an Ar^+ beam at 60° for 30s to see what effect the reduction of wire dimensions would have on the samples. Only wire (b) retained a superconducting transition after milling and so it was measured and milled again. A broadening of the transition was observed as the wire dimensions were reduced (Fig. 6.28).

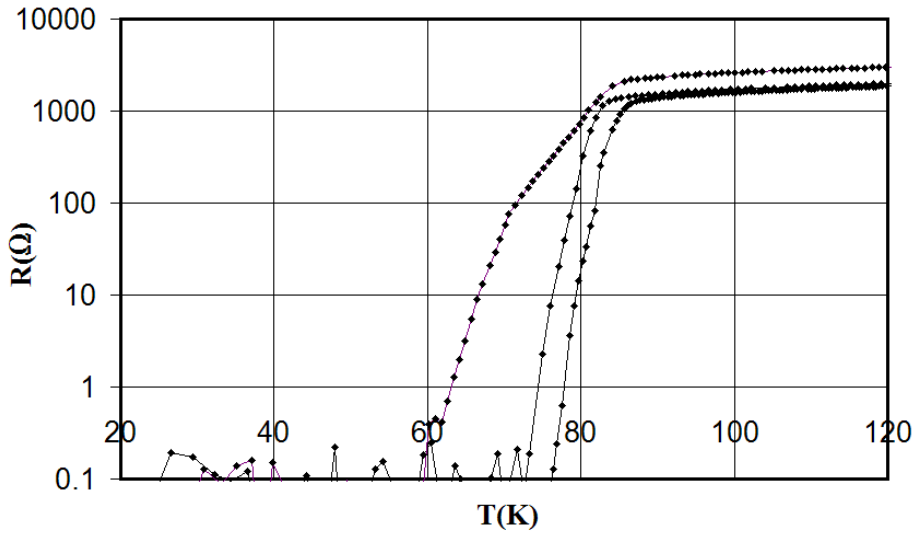

Figure 6.28: The R(T) characteristics of wire (b) after two 30s mills at 60°. The final width of the wire was 205nm.

This was the only YBCO wire that showed a systematic broadening of the transition with the reduction of wire size, as all other samples were destroyed in the milling process.

6.3.1 YBCO analysis

One can compare the data from these YBCO wires to the published results from the literature (Fig.6.29). The YBCO wires from these two experiments show a similar trend with the T_c reducing as the normal state resistance increases. One notable difference is that the wires from [25] fall into two groups. Those with an R_n below R_q exhibit superconductivity, whereas those with R_n above R_q show quasi-insulating behaviour. It was suggested that R_q might be the cross over resistance from one behaviour to the other. However the results from this project no not agree with this theory as wire (d) has an R_n above that of R_q, and yet still appears to have a transition.

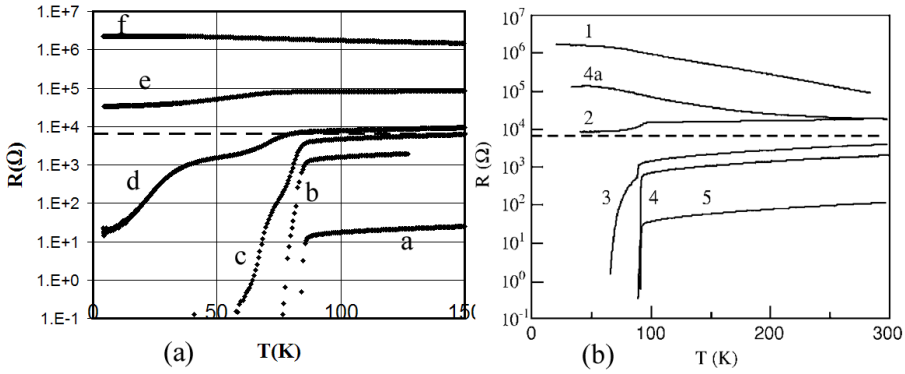

Figure 6.29: (a) shows the data from this project, (b) shows the data from [25]. The dashed line is the quantum of resistance 6.45kΩ.

The R(T) characteristics for the YBCO samples can be analysed in terms of the theory of phase slips to see if broadening of the transition can be attributed to them. This was done in the same way as for Nb. For wires (c) and (d) an attempt was made to fit the theory to the upper and lower transitions of the R(T) characteristics. The theory was also fitted to the

series of R(T) characteristics of wire (b). In the theoretical fits the length of wire L was kept to be the the measured length and $\xi(0)$, T_c and R_n were used as fitting parameters. The results are shown in figures (6.30, 6.31).

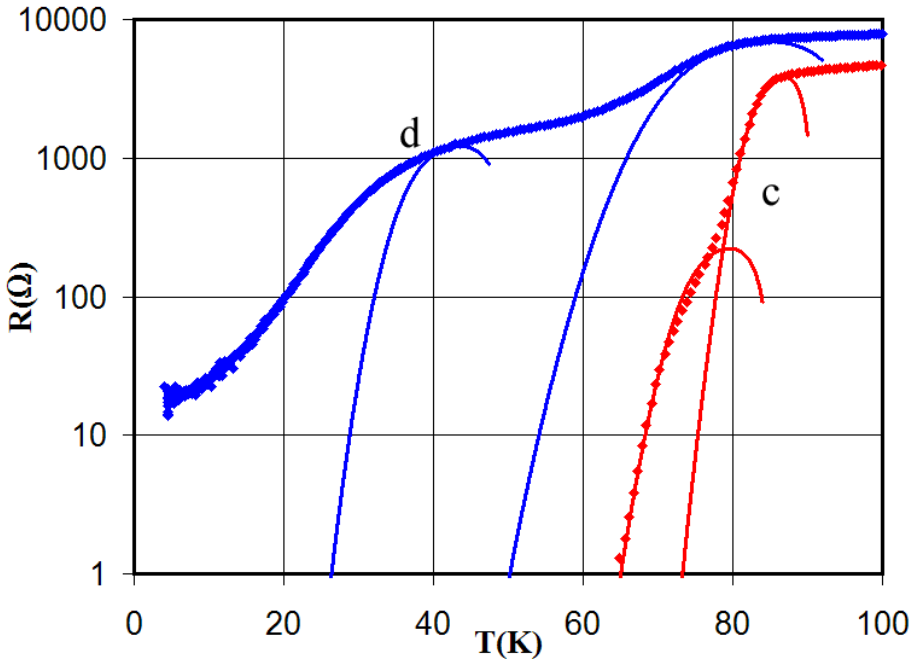

Figure 6.30: Best fits (solid lines) to the experimental data (squares). The fitting parameters for the transition of (c) are: L=7500nm, $\xi(0)$=45nm, T_c=91.3K and R_n=7000Ω, the lower lower transition of (c) are: L=7500nm, $\xi(0)$=1500nm, T_c=86K and R_n=400Ω, the transition of (d) are: L=1750nm, $\xi(0)$=36nm, T_c=100K and R_n=12500Ω and the lower transition of (d) are: L=1750nm, $\xi(0)$=230nm, T_c=52K and R_n=2200Ω.

For the upper transitions in wire (d) and (c) were slightly difficult to fit because the characteristics are obscured at lower temperatures by the lower transition. Even so, the fitting parameters are not wholly unreasonable. The coherence lengths of 36nm and 45nm used in the fit are much larger than that expected in YBCO which is $\sim$ 1.5nm in the *ab* plane. However, the same fit can be found by reducing L and $\xi(0)$ by the same factor. In this

case, using $\xi(0) = 1.5$nm would require $L_d = 73$nm and $L_c = 250$nm.

The interpretation of this is that the phase slip process is constrained to a section of wire smaller than the overall length. This could be true if the FIB milling process caused an inhomogeneous cross section along the length, and so the phase slips in the narrowest region of the wire would dominate. This also matches conclusions from [25] where the phase slip behaviour was attributed to a wire with length and diameter much smaller than that measured.

Just like the analysis for Nb a large R_n was required to fit the data. This R_n was larger than the measured resistance above the transition by a factor of 1.6 for (d) and 1.5 for (c).

As has been mentioned, the resistance of the lower transitions of (d) and (c) were derived from a best fit to non-linear V(I) characteristics, and so it is not clear if these are valid data. Even so, a fit was made to see if the phase slip theory could account for the curves. The lower fits to (d) and (c) required coherence lengths of 230nm and 1500nm respectively, much larger than 1.5nm expected of YBCO. It should be noted that it was very difficult to fit the lower transition of (d) with any satisfaction. For these reasons it is very unlikely that these transitions were caused by phase slips.

The fitting to the R(T) characteristics 1 and 2 of (b) are also quite reasonable with a required coherence length of 70nm and 80nm respectively. Because the characteristics of the final mill are a lot broader, a coherence length of 400nm was required to fit the data. If a coherence length of 1.5nm was assumed for these characteristics the effective length would be reduced to 150nm, 130nm and 26nm respectively. If the resistance were dominated

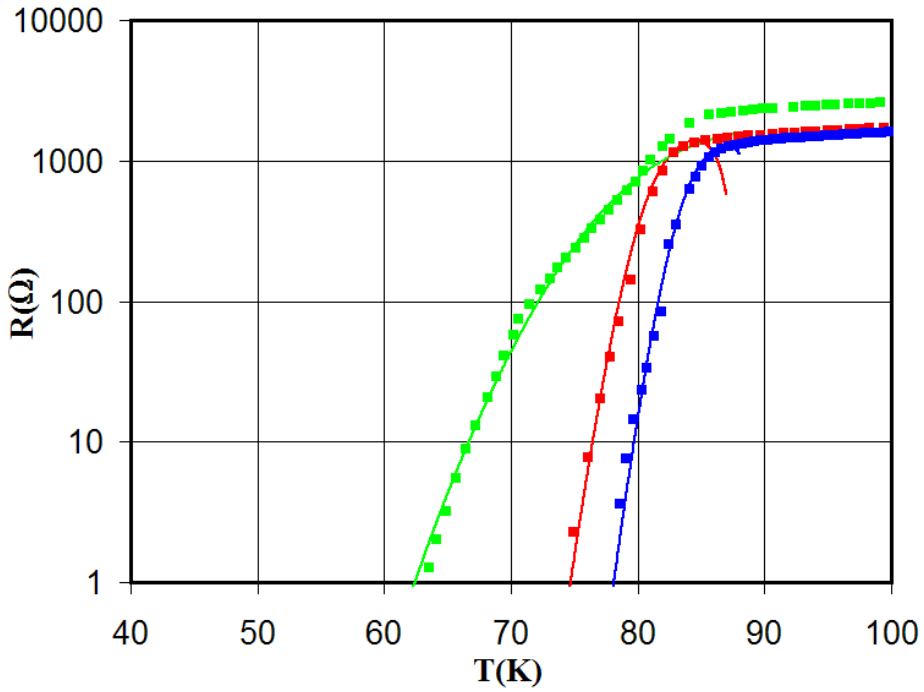

Figure 6.31: The best fits to the R(T) characteristics of (b) after sequential mills. The fitting parameters for the original wires are: L=6900nm, $\xi(0)$=70nm, T_c=90K and R_n=2300Ω, after the first mill are: L=6900nm, $\xi(0)$=80nm, T_c=88K and R_n=2500Ω, and after the second mill are: L=6900nm, $\xi(0)$=400nm, T_c=104K and R_n=3000Ω.

by a small phase slip region along the length of the wire this suggests that milling the wire reduces the length of this region. Again the value of R_n required to fit the data was larger than the measured resistance above T_c, also suggesting that the dominant region has a cross sectional area less than the wire.

A similar conclusion was reached in Ref.[25], where the phase slip behaviour observed in a YBCO wire was attributed to a dominant nano-bridge three orders of magnitude smaller than the measured physical dimensions of the wire. This nano-bridge was calculated to have a cross sectional area

of 4.7nm^2, and a length of 8.4nm. This was from a wire with a measured length of 500nm, and a width and height of 500nm and 150nm respectively. The wires measured in this project show the same behaviour, although the reduction of the effective wire dimensions is less dramatic.

To investigate the hypothesis of a dominant nano-bridge, another fit was made to the data, this time using the LAMH version of ΔF_0. This enabled the use of the cross sectional area as a variable parameter. As well as the cross sectional area, the length and T_c were used to fit the data. Apart from this all other parameters were maintained at the published values, $\xi(0) =$ 1.5nm, $H_c(0) = 1.76 \times 10^{-6}$ A/m, or the measured values for R_n.

Using these parameters the theory only fitted well with characteristics 1 and 2 of wire wire (b) (Fig.6.32). All of the other fits did not match the measured R(T) characteristics at all well. To fit wire (b) the cross sectional area was 9^2nm^2 before milling and 8^2nm^2 after milling, and the length in both cases was 300nm. These results are similar to the previous fit in which a length of 150nm was required. It should be noted that the real values of $\xi(0)$, $H_c(0)$ are not know for the wires, and so the published data on bulk YBCO is the best estimate.

If the broadening of the transitions above are to be attributed to phase slips it is worth re-visiting the value of I_0, the current at which the V(I) characteristics are predicted to become non-linear. At 50K - 100K I_0 has the value 0.65μA - 1.3μA. The V(I) characteristics were measured over a current range of 1μA, around the same range as I_0. Therefore at the lower temperatures it is expected that the measured V would start depend exponentially on the current. This was not observed, as mentioned before, all of the V(I)

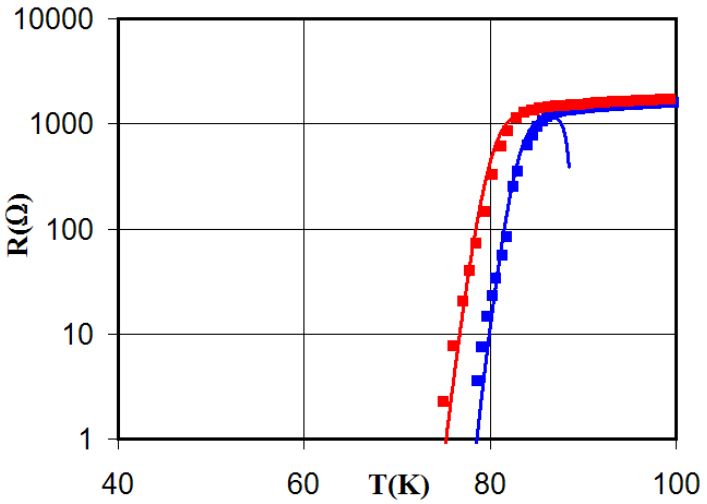

Figure 6.32: Fitting to the R(T) characteristics of (b). The fitting parameters are T_c, L, and A, which for plot 1 were 89K, 300nm, and 9^2nm^2. For plot 2 they were 87K, 300nm, and 8^2nm^2. The R_n used was the measured resistance above the transition, which were R_{n1}=1600Ω and R_{n2}=1700Ω. Other parameters were kept to the published values $\xi(0) = 1.5$nm, $H_c(0) = 1.76 \times 10^{-6}$ A/m.

characteristics were linear. This again brings into question whether phase slips caused the broadening of the transitions.

In summary, it is possible to attribute some of the behaviour observed in the YBCO nanowires to thermally activated phase slips. The width of the transition appears to be related to the dimensions of the wires, although when fitting the theory one requires a much shorter length and area of wire then measured. Again the analysis is complicated by the fact that other mechanisms may be contributing to the resistance at low temperatures. It is known that the transition temperature of YBCO goes down with sample dimensions, and that gallium implantation and oxygen loss suppress T_c. And so any one of these effects could cause a broadening of the transition.

6.4 Analysis Conclusions

Wires of both YBCO and Nb showed similar behaviours with a broadening of the transition increasing with normal state resistance. Because the normal state resistance is a measure of the dimensions of conducting region in the wires, it shows that the broadening is a function of effective wire size. In the Nb wires this was also consistent with the external dimensions of the wire, although in YBCO there was no strong correlation between the wire size and the normal state resistance.

Whether the broadening of the transition is caused by phase slips is not so clear. Although the R(T) characteristics from both Nb and YBCO can be fitted well with LAMH theory of thermal phase slips, the impact of the Ga implantation cannot be ignored. It is clear that having a range of T_c along the length of the wires being measured can lead to a broadened transition reminiscent of phase slips [6]. The T_c of Nb has been shown to decrease with Ga implantation [68], and so irregularity of the Ga concentration could very well cause a range of T_c.

There is some evidence to suggest that some of the R(T) characteristics of YBCO could be caused by phase slips as the R(T) characteristics fit well with the theory and linear V(I) characteristics were observed in a current range below I_0. But again the implantation of Ga complicated matters as the T_c of YBCO is suppressed by the implantation. Also, because the T_c depends on the sample size, an uneven wire cross section along the length could produce a range of T_c that would also cause a broadening of the transition. The FIB milling may well produce an uneven cross section along the length. This may

indeed be the cause of of some wires with large dimensions not exhibiting superconductivity at all, as it only takes one section of the wire to be resistive to obscure the behaviour of the rest of the wire below T_c. Argon ion beam milling was observed to destroy the superconductivity in all but the widest YBCO wires. This also means that oxygen content of the wires is also a significant factor to take into account.

6.5 Project Conclusions

A range of fabrication techniques were employed to investigate the fabrication of nanowires. Many different techniques were investigated to assess their suitability for nanowire production. These included both novel techniques and methods inspired by the established literature. Of all the techniques investigated the greatest success came from samples fabricated using a combination of photolithography, focused ion beam milling and conventional argon ion beam milling. The main advantage of this technique is the ability to measure the properties of the *same sample* at a range of reducing dimensions, a feature not possible with any other fabrication technique.

To be able to produce sub 100nm wires the fabrication equipment was carefully characterised and calibrated. Through this calibration the fabrication process was sequentially refined leading to increasingly narrow sample sizes. The result of this process was the successful production of niobium nanowires with a width of 70nm over a length of 8μm, and YBCO nanowires at a range of widths. A critical part of the fabrication process was the discovery of the ideal angle with which to mill niobium nanowires to produce

an even reduction of both the width and height of the wires. The ideal angle was found to be 75°, and this fact allowed for the production of the narrowest wires. The process that was developed to find the optimum milling angle was not material specific. Therefore this process was not only restricted to superconducting materials and could be used to produce nanowires of *any* other material.

The samples that were produced were very fragile to stress, both mechanical and electromagnetic. Great care was needed when handling samples so as not to destroy them with static discharge or large currents, and a series of measure were put in place to limit sample damage.

An investigation was made into the nature of conductivity in nanowires of Nb and YBCO, at a range of temperatures down to 4K. The samples were cooled in a continuous flow cryostat and measured with electronics that were extensively tested to ensure the data was reliable.

A breakdown of superconductivity was observed below the transition temperature in both materials, which led to a broadening of the superconducting transitions. The data were analysed in terms of the established theory of superconductivity, in order to determine whether the dissipation was being caused by phase slips. As well as the LAMH theory of phase slips, several other mechanisms for dissipation were considered, including flux flow, hot spots and pair breaking.

The R(T) characteristics of the nanowires were found to have quite good agreement with LAMH theory of phase slips. The narrowest wires of Nb showed a low temperature deviation away from the LAMH theory reminiscent of QPS. However, analysis of these characteristics with QPS theory showed

that it was unlikely that QPS caused this low level resistance. Investigation of the resistivity of the wires showed that the resistance appeared to be caused by a wire much smaller than the external dimensions that were measured. This led to the conclusion that the wires are made of a pure niobium core surrounded by an implanted Ga region. This model agreed with published work on Ga implantation in Nb [68] [66]. This also agreed with the phase slips fitting which required the sample diameter to be ∼10nm, much smaller then the external dimensions of the wire.

Analysis of the V(I) characteristics of Nb wires showed a big difference between the measured results and the LAMH theory. The measured voltage of Nb wires was observed to increase linearly with applied current over a current range larger than that predicted by the theory. The behaviour of the V(I) characteristics close to T_c was attributed to pair breaking and the V(I) characteristics at the lowest temperature was interpreted in terms of hot spot formation. This led to the conclusion that the resistance measured was not caused by phase slips.

Of the YBCO wires that exhibited a broadened superconducting transition, one wire showed signs of superconductivity at a R_n greater than R_q, that was in contrast to earlier work in YBCO [25]. YBCO nanowires also showed a deviation away from LAMH theory at low temperatures. However, non linear V(I) characteristics brought the validity of the low temperature resistance into question. The theoretical prediction of an exponential V(I) characteristic at currents above I_0 was not observed in YBCO nanowire either. Again, this was seen as evidence to suggest that the broadening observed in the R(T) characteristics was not caused by phase slips.

It was clear that the effect of Ga implantation was a significant factor in the superconducting properties of the nanowires, as it reduced the T_c of the implanted material and reduced the effective diameter of the nanowires. It was concluded that non-uniformity of Ga implantation along the length of the wires may well have been the cause of the broadening of the transition by two mechanisms. Firstly, differences in the density of implanted Ga ions could have led to varying T_c, and secondly, inhomogeneity of the gallium implantation depth caused varying effective wire diameter along the length of the wires. As the T_c of both Nb and YBCO goes down with reducing sample size, variations of wire diameter would lead to variations of T_c.

Because the process that was developed to successfully produce nanowires is material independent it could be applied to any other material, superconducting or not. By characterising the argon milling process the optimum milling angle can be found which would allow for the reduction of sample size to 100nm and beyond. This has useful applications for the investigation of conductivity at small scales in both superconductors and normal metals.

6.5.1 Future Work

It has been seen that Ga implantation may have been a significant issue in the production of both YBCO and Nb nanowires. Therefore, fabricating nanowires using e-beam lithography would the first step to make for future work as it is a less invasive technique. Much characterisation of the EBL process was made in collaboration with the group at the University of Bath, however more characterisation of the reactive ion etching stage would be

needed to reliably produce Nb nanowires. The EBL fabrication could also be applied to YBCO wires.

The broadening of the superconducting transition as a result of varying T_c is a significant problem as it can obscure the resistance caused by phase slips [6]. The inhomogeneity of wire cross section along the length is a general problem for all superconductors whose T_c varies with sample size, and this issue may affect much of the published literature. Therefore it is not enough to just analyse the R(T) characteristics of nanowires, one needs to analyse the V(I) characteristics as well. There is a clear need in the literature to fully investigate the V(I) behaviour in terms of the theory. To do this one would need to measure at currents above I_0 at a full range of temperatures, and see whether I_0 increased with T.

Furthermore, a system measuring samples down to 0.3K was developed during this project. It includes a high level of shielding and filtering from both ambient magnetic fields and electromagnetic interference, as well as having a very stable temperature control over the temperature range 0.3K to 10K. Therefore this would be the system of choice for the measurement of samples in future work.

Bibliography

[1] J. S. Langer and V. Ambegaokar, Phys. Rev. **164**, 498 (1967).

[2] D. E. McCumber and B. I. Halperin, Phys. Rev. B **1**, 1054 (1970).

[3] J. Mooij and Y. Nazarov, Nature Lett. **2**, 169 (2006).

[4] J. Mooij and C. Harmans, New Journal of Physics **7**, 219 (2005).

[5] T. Giamarchi and H. J. Schulz, Phys. Rev. B **37**, 325 (1988).

[6] M. Zgirski and Y. Arutyunov, Phys. Rev. B **75**, 172509 (2007).

[7] H. Hilgenkamp and J. Mannhart, Rev. Mod. Phys. **74**, 485 (2002).

[8] M. T. A. Bezryadin, C. N. Lau, Nature **404**, 971 (2000).

[9] C. N. Lau, N. Markovic, M. Bockrath, A. Bezryadin, and M. Tinkham, Phys. Rev. Lett. **87**, 217003 (2001).

[10] A. Rogachev and A. Bezryadin, Applied Physics Letters **83**, 512 (2003).

[11] M. Zgirski, K. P. Riikonen, V. Touboltsev, and Y. Arutyunov, Phys. Rev. B **77**, 054508 (2008).

[12] J. E. Lukens, R. J. Warburton, and W. W. Webb, Phys. Rev. Lett. **25**, 1180 (1970).

[13] R. S. Newbower, M. R. Beasley, and M. Tinkham, Phys. Rev. B **5**, 864 (1972).

[14] W. C. Ellis, D. F. Gibbons, and R. G. Treuting, *Growth and Perfection of Crysals* (Wiley, 1958), p. 102.

[15] M. Tian *et al.*, Phys. Rev. B **71**, 104521 (2005).

[16] N. Giordano, Phys. Rev. B **43**, 160 (1991).

[17] N. Giordano, Phys. Rev. Lett. **61**, 2137 (1988).

[18] N. Giordano and E. R. Schuler, Phys. Rev. Lett. **63**, 2417 (1989).

[19] N. Giordano, Phys. Rev. B **41**, 6350 (1990).

[20] D. E. Prober, M. D. Feuer, and N. Giordano, Appl. Phys. Lett. **37**, 94 (1980).

[21] K. Y. Arutyunov, D. S. Golubev, and A. D. Zaikin, Physics Reports **464** (2008).

[22] A. V. Herzog, P. Xiong, F. Sharifi, and R. C. Dynes, Phys. Rev. Lett. **76**, 668 (1996).

[23] F. Sharifi, A. V. Herzog, and R. C. Dynes, Phys. Rev. Lett. **71**, 428 (1993).

[24] P. Xiong, A. V. Herzog, and R. C. Dynes, Phys. Rev. Lett. **78**, 927 (1997).

[25] P. Mikheenko *et al.*, Phys. Rev. B **72**, 174506 (2005).

[26] H. Maeda, Y. Tanaka, M. Fukutomi, and T. Asano, Jpn. J. Appl. Phys. **27**, L209 (1988).

[27] M. Nagao, M. Sato, H. Maeda, S. Kim, and T. Yamashita, Appl. Phys. Lett. **79**, 2612 (2001).

[28] M. Cyrot and D. Pavuna, *Introduction to Superconductivity and High-T_c Materials* (World Scientific, 1995), chap. 5.9, p. 169.

[29] M. Cyrot and D. Pavuna, *Introduction to Superconductivity and High-T_c Materials* (World Scientific, 1995), chap. 5.9, p. 181.

[30] M. M. Abdelhadi and J. A. Jung, Phys. Rev. B **67** (2003).

[31] J. Jung, M. Abdelhadi, H. Darhmauoi, and H. Yan, Int. J. Mod. Phys. B **19**, 167 (2005).

[32] N. Curtz *et al.*, Supercond. Sci. Technol. **23**, 045015 (2010).

[33] C. Carmerlingo, I. Delfino, and M. Lepore, Supercond. Sci. Technol. **15**, 16061609 (2002).

[34] W. E. Booij, *Sub-micron bridges in high-Tc superconductors* (Universiteit Twente, 1994), p. 15.

[35] D. J. Barber.

[36] S. Somekh, J. Vac. Sci. Technol. **13**, 1003 (1976).

[37] R. Mogilevsky *et al.*, Phys. Rev. B **49**, 6420 (1994).

[38] D. J. Quinn and W. B. Ittner, J. Appl. Phys. **33**, 748 (1962).

[39] J. Bardeen, L. N. Cooper, and J. R. Schrieffer, Phys. Rev. **106**, 162 (1957).

[40] Tinkham, *Introduction to Superconductivity*, 2 ed. (Dover, 2004), chap. 1.4, p. 2.

[41] Tinkham, *Introduction to Superconductivity*, 2 ed. (Dover, 2004), chap. 1.4, p. 12.

[42] F. London and H. London, Proc. R. Soc. London A **149**, 71 (1935).

[43] V. Ginzburg and L. Landau, Zh. Eksp. Teor. Fiz. **20**, 1064 (1950).

[44] W. Buckel and R. Kleiner, *Superconductivity*, 2 ed. (Wiley-Vch, 2004).

[45] Tinkham, *Introduction to Superconductivity*, 2 ed. (Dover, 2004).

[46] D. R. Tilley and J. Tilley, *Superfluidity and Superconductivity*, 2 ed. (Adam Hilger Ltd, 1986).

[47] H. Frölich, Phys. Rev. **79**, 845 (1950).

[48] N. L. Cooper, Phys. Rev. **112**, 1900 (1956).

[49] B. D. Josephson, Phys. Lett. **1**, 251 (1962).

[50] R. Feynman, R. Leighton, and M. Sands, *The Feynman Lectures on Physics Vol. III* (Addison-Wesley, 1965), chap. 21, p. 14.

[51] M. Cyrot, Rep. Prog. Phys. **36**, 103 (1973).

[52] R. Voss and R. Webb, Phys. Rev. Lett. **47**, 265 (1981).

[53] J. Martinis, M. Devoret, and J. Clarke, Phys. Rev. B **35**, 4682 (1987).

[54] J. Clarke, Phys. Rev. B **45**, 4682 (1987).

[55] J. Clarke, A. Cleland, M. Devoret, D. Esteve, and J. Martinis, Science **239**, 992 (1988).

[56] Tinkham, *Introduction to Superconductivity*, 2 ed. (Dover, 2004), chap. 8.1, p. 289.

[57] J. M. Graybeal, P. M. Mankiewich, R. C. Dynes, and M. R. Beasley, Phys. Rev. Lett. **59**, 2697 (1987).

[58] S. Saito and Y. Murayama, Phys. Lett. A **135**, 55 (1989).

[59] S. Saito and Y. Murayama, Phys. Lett. A **139**, 85 (1989).

[60] Tinkham, *Introduction to Superconductivity*, 2 ed. (Dover, 2004), chap. 8.1, p. 124.

[61] D. R. Tilley and J. Tilley, *Superfluidity and Superconductivity*, 2 ed. (Adam Hilger Ltd, 1986), p. 229.

[62] X. Lu *et al.*, Physica C: Superconductivity **423**, 175 (2005).

[63] W. J. Skocpol, M. R. Beasley, and M. Tinkham, Journal of Applied Physics **45**, 4054 (1974).

[64] G. K. White, *Experimental Techniques in Low-Temperature Physics* (Oxford University Press, 1959).

[65] O. V. Lounasmaa, *Experimantal Principles and Methods Below 1K*, 1 ed. (Academic Press: London and New York, 1974).

[66] G. C. Tettamanzi *et al.*, Nanotechnology **20**, 465302 (2009).

[67] A. F. Mayadas, R. B. Laibowitz, and J. J. Cuomo, J. Appl. Phys. **43**, 1287 (1972).

[68] Datesman, Cecil, Lyons, Schultz, and Lichtenberger, Applied Superconductivity Conference Jacksonville, FL, October (2004).

[69] S. Foner and E. J. M. Jr., Phys. Lett. **38A**, 323 (1972).

[70] Tinkham, *Introduction to Superconductivity*, 2 ed. (Dover, 2004), chap. 8.1, p. 291.

[71] H. Mori *et al.*

Appendix A

Code for Analysis Program

Here I present the source code of the analysis program.

```
#include <vector>
#include <cmath>
#include <FL/Fl.H>
#include <FL/Fl_Double_Window.H>
#include <FL/fl_draw.H>
#include <FL/Fl_Value_Slider.H>
#include <FL/Fl_Box.H>
#include <FL/Fl_Value_Input.H>
#include <FL/Fl_Multiline_Output.H>
#include <FL/Fl_Round_Button.H>
#include <FL/Fl_Button.H>
#include <iostream>
#include <fstream.h>
#include <cstdlib>
#include <stdio.h>
#include <stdlib.h>
#include <math.h>
#include <vector>

using namespace std;

double boltzmann = 1.380658e-23;
double pi = 3.14159265;

double hBar = 1.05457266e-34;
double muNought = 1.25663706e-6;
double e = 1.60217733e-19;
double Rq = 6453.201824; //The quantum of resistance

```

```
30 double BcZero = 0.206;
31 double CoherenceL = 30; //in nano meters
32 double Tc = 9.25;          //in Kelvin
33 double RNormal = 870;
34
35 double trackL = 1000; //in nano meters
36 double trackW = 20;   //in nano meters
37 double trackT = 5;    //in nano meters
38
39 double prefactorA = 1;
40 double prefactorB = 1;
41 double prefactorC = 1;
42
43 int logbut = 1;
44 double logmultiplier = 100;
45
46 Fl_Window *window;
47 class Drawing;
48 Drawing *canvas;
49
50 int windowW = 1100;
51 int windowH = 700;
52 int canvasH = 700;
53
54 Fl_Value_Slider *graphSliderY;
55 Fl_Value_Slider *graphSliderX;
56
57 Fl_Value_Input *trackLSlider;
58
59 Fl_Value_Input *CoherenceLInput;
60 Fl_Value_Input *TcInput;
61 Fl_Value_Input *RNormalInput;
62 Fl_Value_Input *prefactorAInput;
63 Fl_Value_Input *prefactorBInput;
64
65 Fl_Multiline_Output *output;
66
67 Fl_Round_Button *logbutton;
68
69 Fl_Round_Button *RLAMHbutton;
70 Fl_Round_Button *RLAMHtotbutton;
71 Fl_Round_Button *RQMbutton;
72 Fl_Round_Button *RQMtotbutton;
73 Fl_Round_Button *ALLRbutton;
74
75 Fl_Button *writeButton;
76 Fl_Button *readButton;
77
78 int vectorSize = 10000;
79 //the y values of the plotting data will be recorded in these vectors
80 //there are vectorSize elements in each vector and each element corresponds to a temperature
```

```
81 //each element corresponds to 0.01K giving a range of 0K-100K
82 vector<double> RLAMH(vectorSize,0);
83 vector<double> RLAMHtot(vectorSize,0);
84 vector<double> RQM(vectorSize,0);
85 vector<double> RQMtot(vectorSize,0);
86 vector<double> ALLR(vectorSize,0);
87
88 //Vectors to hold values from a text file of R(T) data
89 vector <double> writeTemperature;
90 vector <double> writeResistance;
91
92
93 //a class extending Fl_Double_Window to deal with all the drawing
94 class Drawing : public Fl_Double_Window
95 {
96   private:
97     void draw()
98     {
99       canvasH = this->h(); //reset canvas height so that graph gets re-drawn correctly when re-sizing
              window
100
101      fl_color(FL_WHITE);
102      fl_rectf(0,0,w(),h());
103
104      double Y = graphSliderY->value();
105      double X = graphSliderX->value();
106
107      //draw the X axis
108      fl_color(FL_GRAY);
109      fl_line_style(0,2);
110      fl_begin_line();
111      fl_vertex(0,0);
112      fl_vertex(0,850);
113      fl_end_line();
114
115      for (int i = 0; i<vectorSize; i=i+100)
116      {
117        fl_line_style(0,0);
118        fl_begin_line();
119        fl_vertex(i*(1/X),canvasH);
120        fl_vertex(i*(1/X),0);
121
122        //draw the numbers for temperature
123        int temp = i/100;
124        char s[10];
125        sprintf(s, "%i", temp);
126        int swidth = (int)i*(1/X);
127        fl_draw(s,swidth,canvasH-10);
128        fl_end_line();
129      }
130
```

```
131       //draw the Y axis
132       fl_color(FL_GRAY);
133       fl_line_style(0,2);
134       fl_begin_line();
135       fl_vertex(1,0);
136       fl_vertex(1,850);
137       fl_end_line();
138
139       for (int i = 0; i<20000; i=i+10)
140       {
141
142         if(i%100 == 0 && logbut == 1)
143         {
144           fl_line_style(0,2);
145           fl_begin_line();
146           fl_vertex(0,(canvasH)-(i*(1/Y)));
147           fl_vertex(windowW,(canvasH)-(i*(1/Y)));
148           fl_end_line();
149
150           //draw the numbers for temperature
151           int temp = i/100;
152           char power[10];
153           sprintf(power, "%i", temp);
154
155           int ten = 10;
156           char s[10];
157           sprintf(s, "%i", ten);
158
159           fl_draw(s,2,(canvasH)-(i*(1/Y)));
160           fl_draw(power,15,(canvasH-5)-(i*(1/Y)));
161           fl_end_line();
162         }
163         else
164           if(i%100 == 0)
165           {
166             fl_line_style(0,2);
167             fl_begin_line();
168             fl_vertex(0,(canvasH)-(i*(1/Y)));
169             fl_vertex(windowW,(canvasH)-(i*(1/Y)));
170             fl_end_line();
171
172             //draw the numbers for temperature
173             int temp = i/10;
174             char s[10];
175             sprintf(s, "%i", temp);
176             int sheight = (int)i*(1/Y);
177             fl_draw(s,2,(canvasH)-(i*(1/Y)));
178             fl_end_line();
179           }
180         else
181           if(logbut == 0 && Y < 3)
```

```
182           {
183             fl_line_style(0,0);
184             fl_begin_line();
185             fl_vertex(0,(canvasH)-(i*(1/Y)));
186             fl_vertex(windowW,(canvasH)-(i*(1/Y)));
187             fl_end_line();
188           }
189       }
190
191       //draw RLAMH
192       if(RLAMHbutton->value() == 1)
193       {
194         fl_color(FL_DARK_BLUE);
195         fl_line_style(0,0);
196         fl_begin_line();
197         for (int i = 0; i<RLAMH.size(); i++)
198         {
199           //cout << RLAMHtot[i] << endl;
200           double n = double(i);
201           if(logbut == 1 && RLAMH[i] > 0)
202             fl_vertex(n*(1/X),
203             (canvasH)-(log10(RLAMH[i]))*(1/Y)*logmultiplier);
204           else
205             fl_vertex(n*(1/X),
206             (canvasH)-(RLAMH[i]*10)*(1/Y));
207         }
208         fl_end_line();
209       }
210
211       //draw RLAMHtot
212       if(RLAMHtotbutton->value() == 1)
213       {
214         fl_color(FL_BLUE);
215         fl_line_style(0,0);
216         fl_begin_line();
217         for (int i = 0; i<RLAMHtot.size(); i++)
218         {
219           //cout << RLAMHtot[i] << endl;
220           double n = double(i);
221           if(logbut == 1 && RLAMHtot[i] > 0)
222             fl_vertex(n*(1/X),
223             (canvasH)-(log10(RLAMHtot[i]))*(1/Y)*logmultiplier);
224           else
225             fl_vertex(n*(1/X),
226             (canvasH)-(RLAMHtot[i]*10)*(1/Y));
227         }
228         fl_end_line();
229       }
230
231       //draw RQM
232       if(RQMbutton->value() == 1)
```

```
233       {
234         fl_color(FL_DARK_GREEN);
235         fl_line_style(0,0);
236         fl_begin_line();
237         for (int i = 0; i<RQM.size(); i++)
238         {
239           //cout << RQM[i] << endl;
240           double n = double(i);
241           if(logbut == 1 && RQM[i] > 0)
242             fl_vertex(n*(1/X),
243             (canvasH)-(log10(RQM[i]))*(1/Y)*logmultiplier);
244           else
245             fl_vertex(n*(1/X),
246             (canvasH)-(RQM[i]*10)*(1/Y));
247         }
248         fl_end_line();
249       }
250 
251       //draw RQMtot
252       if(RQMtotbutton->value() == 1)
253       {
254         fl_color(FL_GREEN);
255         fl_line_style(0,0);
256         fl_begin_line();
257         for (int i = 0; i<RQMtot.size(); i++)
258         {
259           //cout << RQMtot[i] << endl;
260           double n = double(i);
261           if(logbut == 1 && RQMtot[i] > 0)
262             fl_vertex(n*(1/X),
263             (canvasH)-(log10(RQMtot[i]))*(1/Y)*logmultiplier);
264           else
265             fl_vertex(n*(1/X),
266             (canvasH)-(RQMtot[i]*10)*(1/Y));
267         }
268         fl_end_line();
269       }
270 
271       //draw RLAMH+RQM
272       if(ALLRbutton->value() == 1)
273         {
274         fl_color(FL_RED);
275         fl_line_style(0,0);
276         fl_begin_line();
277         for (int i = 0; i<ALLR.size(); i++)
278         {
279           //cout << ALLR[i] << endl;
280           double n = double(i);
281           if(logbut == 1 && ALLR[i] >0)
282             fl_vertex(n*(1/X),
283             (canvasH)-(log10(ALLR[i]))*(1/Y)*logmultiplier);
```

```
284           else
285             fl_vertex(n*(1/X),
286             (canvasH)-(ALLR[i]*10)*(1/Y));
287         }
288         fl_end_line();
289       }
290
291       //draw the R(T) from a datafile (if loaded)
292       fl_color(FL_BLACK);
293       fl_line_style(0,2);
294       fl_begin_line();
295       for (int i = 0; i < writeResistance.size(); i++)
296       {
297         if(logbut == 1 && writeResistance[i] > 0)
298           fl_vertex(writeTemperature[i]*100*(1/X),
299           (canvasH)-(log10(writeResistance[i]))*(1/Y)*logmultiplier);
300         else
301           fl_vertex(writeTemperature[i]*100*(1/X),
302           (canvasH)-(writeResistance[i]*10)*(1/Y));
303       }
304       fl_end_line();
305     }
306
307   public:
308       Drawing(int X,int Y,int W,int H) : Fl_Double_Window(X,Y,W,H) {}
309 };
310
311
312 // Function to re-calculate the values
313 //in the data vectors depending on the values of
314 //the slider buttons and input buttons.
315 void calc()
316 {
317 //WORK OUT THE RESISTANCE DUE TO THERMAL PHASE SLIPS
          ***************************************************
318
319   //a vector to hold the values of deltaF
320   vector<double> deltaF(vectorSize,0);
321
322   //fill all the values of deltaF
323 /*    for (int i = 0; i<deltaF.size(); i++)
324   {
325     double n = double(i)+0.1;
326     double two = 2;
327     double temp =((8*sqrt(two))/3)*
328           (pow((BcZeroInput->value()*
329           (1-((n/100)/TcInput->value()))),2)/(2*muNought))*
330           (trackWSlider->value()*1e-9)*
331           (trackTSlider->value()*1e-9)*
332           (CoherenceLInput->value()*1e-9)*
333           pow(1-((n/100)/TcInput->value()),-0.5);
```

```
334     if(temp > 1e-99)
335     {
336       deltaF[i] = temp;
337     }
338     else
339     {
340       deltaF[i] = 0;
341     }
342     //if(i<10)
343       //cout << n/100 << endl;
344       //cout << deltaF[i] << endl;
345   }*/
346
347   //calculate deltaF using Tinkham's form
348   //in terms of the resisatnce quantum, eliminating Bc
349   for (int i = 0; i<deltaF.size(); i++)
350   {
351     double n = double(i)+0.1;
352     double two = 2;
353     double temp =0.83*(trackLSlider->value()/CoherenceLInput->value())*
354             (Rq/RNormalInput->value())*
355             boltzmann*TcInput->value()*
356             pow(1-((n/100)/TcInput->value()),1.5);
357     if(temp > 1e-99)
358     {
359       deltaF[i] = temp;
360     }
361     else
362     {
363       deltaF[i] = 0;
364     }
365     //if(i<10)
366       //cout << n/100 << endl;
367       //cout << deltaF[i] << endl;
368   }
369
370   //a vector to hold the values of the Ginzberg Landau Relaxation time
371   vector<double> tGL(vectorSize,0);
372
373   //fill in all the values of tGL
374   for (int i = 0; i<tGL.size(); i++)
375   {
376     double n = double(i)+0.1;
377     tGL[i]=(pi*hBar)/(8*boltzmann*(TcInput->value()-(n/100)));
378     //if(i<100)
379     //    cout << tGL[i] << endl;
380   }
381
382   //a vector to hold the values for the omega in the attack frequency
383   vector<double> omega(vectorSize,0);
384
```

```
385   //fill in all the values of omega
386   for (int i = 0; i<omega.size(); i++)
387   {
388     double n = double(i)+0.1;
389
390     double temp=((trackLSlider->value()*1e-9)/
391       ((CoherenceLInput->value()*1e-9)*
392       pow(1-((n/100)/TcInput->value()),-0.5)))*
393       pow((deltaF[i]/(boltzmann*(n/100))),0.5)*
394       (1/tGL[i]);
395
396     if(temp > 1e-99)
397     {
398       omega[i] = temp;
399       //cout << temp << endl;
400     }
401     else
402     {
403       omega[i] = 0;
404     }
405     //if(i<1000)
406       //cout << "class" << omega[i] << endl;
407   }
408
409   //fill in all the values of RLAMH
410   for (int i = 0; i<RLAMH.size(); i++)
411   {
412     double n = double(i)+0.1;
413     RLAMH[i]=((pi*pow(hBar,2)*omega[i])/
414         (2*pow(e,2)*boltzmann*(n/100)))
415         *exp(-deltaF[i]/(boltzmann*(n/100)));
416
417     //RLAMH[i]=exp(-deltaF[i]/(boltzmann*(n/100)));
418     //if(i<100)
419     //    cout << RLAMH[i] << endl;
420   }
421
422   //fill in RLAMHtot to be plotted
423   for (int i = 0; i<RLAMHtot.size(); i++)
424   {
425     RLAMHtot[i] = (RLAMH[i]*RNormalInput->value())/
426     (RLAMH[i]+RNormalInput->value());
427     //RLAMHtot[i] = RLAMH[i];
428     //if(i<100)
429     //    cout << RLAMHtot[i] << endl;
430   }
431
432 //*****************************************************************
433
434 //WORK OUT THE RESISTANCE DUE TO QUANTUM PHASE SLIPS
          ******************************************************************
```

```
435
436   //a vector to hold the values for the omega
437   //in the attack frequency for the QM case
438
439   vector<double> omegaQM(vectorSize,0);
440
441   //fill in all the values of omega for the QM case
442   for (int i = 0; i<omegaQM.size(); i++)
443   {
444     double n = double(i)+0.1;
445
446     double temp=((trackLSlider->value()*1e-9)/
447         ((CoherenceLInput->value()*1e-9)*
448         pow(1-((n/100)/TcInput->value()),-0.5)))*
449         pow((deltaF[i]/(hBar/tGL[i])),0.5)*
450         (1/tGL[i]);
451
452     if(temp > 1e-99)
453     {
454       omegaQM[i] = temp;
455     }
456     else
457     {
458       omegaQM[i] = 0;
459     }
460     //if(i<100)
461       //cout << "Quantum" << omegaQM[i] << endl;
462   }
463
464   //fill in all the values of RQM
465   for (int i = 0; i<RQM.size(); i++)
466   {
467     double n = double(i);
468     RQM[i]=prefactorBInput->value()*
469           (((pi*pow(hBar,2)*omegaQM[i])/(2*pow(e,2)*
470           (hBar/tGL[i])))*(exp(prefactorAInput->value()*
471           (-deltaF[i]/(hBar/tGL[i])))));
472
473     //RQM[i]=exp(-deltaF[i]/(hBar/tGL[i]));
474     //if(i<100)
475     //    cout << RQM[i] << endl;
476   }
477
478   //fill in RQMtot to be plotted
479   for (int i = 0; i<RQMtot.size(); i++)
480   {
481     RQMtot[i] = (RQM[i]*RNormalInput->value())/
482                 (RQM[i]+RNormalInput->value());
483
484     //RQMtot[i] = RQM[i];
485     //if(i<100)
```

```
486     //    cout << RQMtot[i] << endl;
487   }
488
489   //fill in the ALLR for the plot of RQM + RLAMH
490   for (int i = 0; i<ALLR.size(); i++)
491   {
492     ALLR[i] = 1/((1/(RQM[i]+RLAMH[i]))+
493               (1/RNormalInput->value()));
494
495     //if(i<100)
496     //    cout << ALLR[i] << endl;
497   }
498 }
499
500 //***************************************
501
502 //Callback function for the slider buttons
503 void calculate_cb(Fl_Widget*, void*)
504 {
505   calc();
506   canvas->redraw();
507 }
508
509 //Callback function for the log buttons
510 void logbutton_cb(Fl_Widget*, void*)
511 {
512   logbut = logbutton->value();
513   calc();
514   canvas->redraw();
515 }
516
517 //Callback function for the write button
518 void writeButton_cb(Fl_Widget*, void*)
519 {
520   ofstream writefile;
521   writefile.open ("values.txt");
522   writefile << "Parameters:\n";
523
524   writefile <<" CoherenceL="<<CoherenceLInput -> value()<<
525               " Tc="<<TcInput -> value()<<
526               " RNormal="<<RNormalInput -> value()<<
527               " trackL="<<trackLSlider -> value()<<
528               " prefactorA="<<prefactorAInput -> value()<<
529               " prefactorB="<<prefactorBInput -> value() <<"\n";
530
531   writefile << "N RLAMH RLAMHtot RQM RQMtot ALLR\n";
532
533   for (int i = 0; i<ALLR.size(); i++)
534   {
535     writefile << (double)i/100 << " ";
536     writefile << RLAMH[i] << " ";
```

```
537     writefile << RLAMHtot[i] << " ";
538     writefile << RQM[i] << " ";
539     writefile << RQMtot[i] << " ";
540     writefile << ALLR[i] << " \n";
541   }
542   writefile.close();
543 }
544
545 //Callback function for the read button
546 void readButton_cb(Fl_Widget*, void*)
547 {
548   ifstream datafile;
549   string data;
550   datafile.open("rt.txt");
551
552   if(!datafile) {
553     cout << "File doesn't exist" << endl;
554     exit(0);
555   }
556
557   datafile >> data; //puts first element from the datafile into data
558   int i = 0;
559   while ( !datafile.eof() ) {
560     if (i == 0) {
561       double tempTemperature;
562
563       // convert string to double put in tempTemperature
564       tempTemperature = atof(data.c_str());
565
566       //then put value into vector
567       cout << tempTemperature << " ";
568       writeTemperature.push_back(tempTemperature);
569     }
570     else if (i == 1) {
571       double tempResistance;
572       tempResistance = atof(data.c_str());
573       cout << tempResistance << " ";  //then put value into vector
574       writeResistance.push_back(tempResistance);
575     }
576     else if (i == 4) {
577       cout << data << endl;
578       i = -1;
579     }
580     else {
581       cout << data << " ";
582     }
583     datafile >> data;
584     i++;
585   }
586
587   datafile.close();
```

```
588   cout << "End of file." << endl;
589
590   int j = 0;
591   while(j < writeResistance.size()){
592     cout << writeTemperature[j] << " " << writeResistance[j] << endl;
593     j++;
594   }
595
596   calc();
597   canvas->redraw();
598 }
599
600 int main()
601 {
602   // The main window
603   window = new Fl_Window(0,0,windowW,windowH,"Phase Slips");
604   window->resizable(window);
605
606 // A widget to draw on
607   canvas = new Drawing(20,0,windowW-200,windowH-40);
608   canvas->end();
609
610 //some slider buttons
611
612   trackLSlider = new Fl_Value_Input(windowW-100,120,60,30,"Length");
613   trackLSlider -> value(trackL);
614   trackLSlider -> callback(calculate_cb);
615
616   graphSliderY = new Fl_Value_Slider(0,0,20,(windowH-40), "R/T");
617   graphSliderY -> type(FL_VERT_NICE_SLIDER);
618   graphSliderY -> range(10,0.0001);
619   graphSliderY -> value(1);
620   graphSliderY -> precision(3);
621   graphSliderY -> callback(calculate_cb);
622
623   graphSliderX = new Fl_Value_Slider(20,(windowH-40),(windowW-200),20, "X");
624   graphSliderX -> type(FL_HOR_NICE_SLIDER);
625   graphSliderX -> range(0.0001,10);
626   graphSliderX -> value(1.5);
627   graphSliderX -> precision(3);
628   graphSliderX -> callback(calculate_cb);
629
630   CoherenceLInput = new Fl_Value_Input(windowW-100,150,60,30,"Coh L");
631   CoherenceLInput -> value(CoherenceL);
632   CoherenceLInput -> callback(calculate_cb);
633
634   TcInput = new Fl_Value_Input(windowW-100,180,60,30,"Tc");
635   TcInput -> value(Tc);
636   TcInput -> callback(calculate_cb);
637
638   RNormalInput = new Fl_Value_Input(windowW-100,210,60,30,"Rn");
```

```
639   RNormalInput -> value(RNormal);
640   RNormalInput -> callback(calculate_cb);
641
642   prefactorAInput = new Fl_Value_Input(windowW-100,260,60,30,"A");
643   prefactorAInput -> value(prefactorA);
644   prefactorAInput -> callback(calculate_cb);
645
646   prefactorBInput = new Fl_Value_Input(windowW-100,290,60,30,"B");
647   prefactorBInput -> value(prefactorB);
648   prefactorBInput -> callback(calculate_cb);
649
650   output = new Fl_Multiline_Output(0,windowH - 20,windowW-180, 20);
651
652   logbutton = new Fl_Round_Button(windowW-130,490,30,30,"log scale");
653   logbutton -> callback(logbutton_cb);
654
655   RLAMHbutton = new Fl_Round_Button(windowW-130,370,30,30,"RLAMH");
656   RLAMHbutton -> value(1);
657   RLAMHbutton -> callback(calculate_cb);
658
659   RLAMHtotbutton = new Fl_Round_Button(windowW-130,390,30,30,"RLAMH total");
660   RLAMHtotbutton -> value(1);
661   RLAMHtotbutton -> callback(calculate_cb);
662
663   RQMbutton = new Fl_Round_Button (windowW-130,410,30,30,"RQM");
664   RQMbutton -> value(1);
665   RQMbutton -> callback(calculate_cb);
666
667   RQMtotbutton = new Fl_Round_Button(windowW-130,430,30,30,"RQM total");
668   RQMtotbutton -> value(1);
669   RQMtotbutton -> callback(calculate_cb);
670
671   ALLRbutton = new Fl_Round_Button(windowW-130,450,30,30,"All R");
672   ALLRbutton -> value(1);
673   ALLRbutton -> callback(calculate_cb);
674
675   writeButton = new Fl_Button(windowW-150,550,100,40," Write File");
676   writeButton -> callback(writeButton_cb);
677
678   readButton = new Fl_Button(windowW-150,600,100,40," Read File");
679   readButton -> callback(readButton_cb);
680
681   calc();
682
683   window->end();
684   window->show();
685   return Fl::run();
686 }
```